



Libraries and Learning Services

University of Auckland Research Repository, ResearchSpace

Copyright Statement

The digital copy of this thesis is protected by the Copyright Act 1994 (New Zealand).

This thesis may be consulted by you, provided you comply with the provisions of the Act and the following conditions of use:

- Any use you make of these documents or images must be for research or private study purposes only, and you may not make them available to any other person.
- Authors control the copyright of their thesis. You will recognize the author's right to be identified as the author of this thesis, and due acknowledgement will be made to the author where appropriate.
- You will obtain the author's permission before publishing any material from their thesis.

General copyright and disclaimer

In addition to the above conditions, authors give their consent for the digital copy of their work to be used subject to the conditions specified on the [Library Thesis Consent Form](#) and [Deposit Licence](#).

Active and adaptive control of noise transmission in structures

Khairul Affendy Md Nor

A thesis submitted in complete fulfilment of the requirements for the degree of
Doctor of Philosophy in Mechatronics Engineering
The University of Auckland, 2018

ACKNOWLEDGEMENTS

All praises to God, for granting me courage, strength and health to complete this research.

I would like to express my deepest gratitude towards my principal supervisor Professor Brian Mace and my co-supervisor Dr. Yusuke Hioka for their positive encouragement, constructive ideas and invaluable advice. Under their supervision and guidance, I was able to learn and grow tremendously over the progressive years. And I am most grateful for their motivation, professional and immense knowledge, and endless comments on and editing of my English writing. Thank you!

I am also thankful to the lab technicians, Mr. Gian Schmit and Mr. Sarath Pathirana, for their helps during experimental works.

I want to express my deep gratitude to my beloved wife, Alena, for her love, patience and unlimited encouragement given throughout this PhD journey. My gratitude also goes to my lovely son Amsyar and daughter Abirah for being my strength and motivation. Thanks to my parents and siblings for being the source of inspiration to become who I am now.

Last but not least, I would like to acknowledge the Ministry of Higher Education Malaysia (MOHE) and International Islamic University Malaysia (IIUM) for the financial support through SLAB scholarship.

Thank you!

ABSTRACT

The thesis presents a method of calculating the radiated sound power of vibrating structures based on the time domain estimation of acoustic radiation modes (ARMs). Each ARM is frequency-dependent, radiates power independent of the other ARMs and can be estimated in the time domain from measurements made at discrete sensor locations on the surface of the radiating structure. The individual ARM components are estimated digitally in the time domain using finite impulse response filters, which are designed to provide a best weighted fit to the ARMs in the frequency domain. The ARM amplitudes are estimated by filtering the vectors of measured velocities at points on the radiating surface with these ARM filters, before summing the product of the square of these amplitudes multiplied by the relevant ARM eigenvalues to estimate the radiated sound power. The method is described with reference to one and two dimensional radiators, namely a simply supported beam and a clamped plate. The results show that the sound power calculated from the proposed approach and from a frequency domain approach are comparable. Next, real time simulations of active structural acoustic control are performed using real-time ARM amplitudes as the cost function of the controller. The primary path is the path between the disturbance signal and the error signal, in this case, the ARM amplitude. The secondary path is from the controller output to the error signal. Two control strategies are considered here. The first one is non-adaptive feedforward active structural acoustic control, which is applied to a baffled beam. The controller transfer function is defined by the ratio of the primary path and secondary path frequency responses. This technique requires the control path to be accurately estimated using an FIR filter to get good attenuation. The second strategy is adaptive feedforward active structural acoustic control with reference to the baffled plate as the radiator. The controller is based on the filtered-x version of the adaptive LMS algorithm. Here two FIR filters are required to estimate the secondary and the control paths. To get good attenuation, the optimal locations of the control actuators are obtained using a swarm intelligent algorithm called Ant Colony Optimization. Finally, physical experiments are conducted to validate the findings.

PUBLICATIONS

Md Nor, K., Mace, B., & Hioka, Y. (2016). Time-domain estimation of acoustic radiation modes and active structural acoustic control. In I. D. M. Hillock, D. J. Mee (Eds.) Proceedings of ACOUSTICS 2016 Brisbane, Queensland, Australia.

Md Nor, K., Mace, B., & Hioka, Y. (2017). Adaptive control of radiated sound power based on time-domain estimates of acoustic radiation modes. Proceedings of International Congress on Sound and Vibration (ICSV 24), London, UK.

TABLE OF CONTENTS

ACKNOWLEDGEMENTS	i
ABSTRACT.....	ii
PUBLICATIONS.....	iii
TABLE OF CONTENTS.....	iv
LIST OF FIGURES	vii
NOMENCLATURE	xii
CHAPTER 1 : INTRODUCTION	1
1.1 Overview	1
1.2 Literature review	2
1.2.1 Measurement of the radiated sound power	2
1.2.2 Acoustic radiation modes	3
1.2.3 Active control approaches.....	4
1.2.4 Active structural acoustic control.....	5
1.3 Motivation	6
1.4 Objectives.....	7
1.5 Contributions.....	7
1.6 Thesis outline	8
CHAPTER 2 : RADIATED SOUND POWER FROM VIBRATING STRUCTURES AND ACOUSTIC RADIATION MODES	9
2.1 Introduction.....	9
2.2 Radiated sound power from a plane radiating surface	9
2.3 Acoustic radiation modes	12
2.3.1 Numerical example: One dimensional radiator.....	13
2.3.2 Numerical example: Two dimensional radiator.....	15
2.4 Equation of motion of the radiators	18
2.4.1 Simply supported beam.....	18
2.4.1.1 Numerical simulation: Structural mode shapes and natural frequencies	24
2.4.1.2 Numerical simulation: Radiated sound power of beam radiator.....	25
2.4.2 Clamped rectangular plate.....	27
2.4.2.1 Numerical simulations: Mode shapes and natural frequencies	31

2.4.2.2 Numerical simulations: Radiated sound power of plate radiator	33
2.5 Summary	35
CHAPTER 3 : TIME-DOMAIN ESTIMATION OF ACOUSTIC RADIATION MODE AMPLITUDES	37
3.1 Introduction	37
3.2 Acoustic radiation modes estimated using FIR filters	37
3.3 Practical implementation of ARM FIR filters.....	38
3.4 Filter quality	42
3.5 Structural response estimation using IIR filters	42
3.6 Estimation of radiated sound power.....	45
3.7 Numerical simulations	46
3.7.1 Performance of acoustic radiation mode filters	47
3.7.2 Structural transfer function filters	51
3.7.3 Estimation of radiated sound power.....	53
3.8 Summary	59
CHAPTER 4 : ACTIVE CONTROL OF RADIATED SOUND POWER OF VIBRATING STRUCTURES.....	60
4.1 Introduction	60
4.2 Cancellation of the first few acoustic radiation modes	61
4.3 Feedforward active structural acoustic control applied to the vibrating beam	63
4.3.1 Real time implementation of feedforward controller.....	64
4.3.2 Real-time simulation: Feedforward active structural acoustic control of beam radiator	65
4.3.2.1 Frequency responses of the feedforward controllers	67
4.3.2.2 Control results	69
4.4 Adaptive control of radiated sound power from a vibrating plate	73
4.4.1 Filtered-x LMS controller	74
4.4.2 Estimation of secondary path.....	77
4.4.3 Real-time simulation: Adaptive control of radiated sound power from vibrating plate	79
4.4.3.1 Adaptive controller settings	80
4.4.3.2 Results of adaptive control.....	81
4.5 Optimisation of location of control actuators	86
4.5.1 Ant colony optimisation algorithm	86

4.5.2	Objective function.....	88
4.5.3	Optimisation settings.....	90
4.5.4	Optimisation results	91
4.6	Summary	96
CHAPTER 5 : EXPERIMENT		98
5.1	Introduction.....	98
5.2	Test structure.....	98
5.3	Structural sensors and actuators	100
5.4	Instrumentation	104
5.5	Compact RIO Controller programming	105
5.6	Calculation of the sound power radiated from the vibrating plate.....	107
5.6.1	ISO 3741 method	107
5.6.2	Statistical method.....	108
5.7	Experimental results.....	109
5.7.1	Estimation of radiated sound power.....	109
5.7.2	Control of radiated sound power using FxLMS control	111
5.7.2.1	Tonal excitation.....	111
5.7.2.2	Broadband, random noise excitation.....	112
5.8	Summary	114
CHAPTER 6 : CONCLUSIONS AND RECOMMENDATIONS		116
6.1	Conclusions.....	116
6.2	Recommendations for future work.....	118
6.3	Summary	120
BIBLIOGRAPHY.....		122
APPENDIX A.....		129

LIST OF FIGURES

Figure 2.1: Coordinate system of plane baffled structure [55].	10
Figure 2.2: The first six ARMs of a one-dimensional baffled structure as functions of position and dimensionless frequency kl .	14
Figure 2.3: Radiation efficiencies of individual ARMs for 1-D radiator.	15
Figure 2.4: (a) First, (b) second, (c) third and (d) fourth ARM shapes of a rectangular 2-D structure when dimensionless frequency $kl = 0.1, 1, 5$ and 10 , respectively.	17
Figure 2.5: Radiation efficiencies of individual ARMs of the plate.	18
Figure 2.6: Thin beam.	18
Figure 2.7: Mode shapes of a simply supported beam.	25
Figure 2.8: Radiated sound power of beam radiator.	26
Figure 2.9: Ratio of sound powers of individual ARMs to the total sound power of beam radiator.	26
Figure 2.10: Thin plate.	27
Figure 2.11: Mode shapes of the clamped plate.	32
Figure 2.12: Radiated sound power of plate radiator, where W_j is the individual sound power from j^{th} ARM.	34
Figure 2.13: Ratio of sound powers of individual ARMs to the total sound power of plate radiator.	35
Figure 3.1: Real-time r^{th} ARM filter.	39
Figure 3.2: Coefficients of non-causal and causal FIR filters for $q_{1,n}$, $q_{2,n}$ and $q_{3,n}$ for ARMs 1, 2 and 3 as functions of time sample index m , for $d=7$.	40
Figure 3.3: Coefficients of FIR filters for $q_{1,n}$, $q_{2,n}$ and $q_{3,n}$ for ARMs 1, 2 and 3 as functions of time step m , for $d=7$, measured at point $(0.1L_x, 0.3L_y)$.	41
Figure 3.4: Resonant filter of mode β , $H_\beta(z)$.	45
Figure 3.5: Configuration of resonant filters to simulate the real-time structural surface velocities.	45
Figure 3.6: Block diagram representation of the time domain radiated sound power estimation.	46

Figure 3.7: (a) Magnitude of the frequency response of the ARM filters for the first three ARMs using causal FIR filters and (b) mean square error as a function of number of filter coefficient s	49
Figure 3.8: (a) Magnitude of the frequency response of the ARM filters for the first three ARMs using causal-delayed FIR filters and (b) mean square error as a function of number of filter coefficient s (where $s=2d+1$).	50
Figure 3.9: Phases comparison of the theoretical and estimated first 3 ARM frequency responses using causal and causal-delayed FIR filters, measured at $(0.1L_x, 0.3L_y)$	51
Figure 3.10: Magnitudes and phases of the theoretical and estimated modal frequency responses for the first three modes.	52
Figure 3.11: z-plane pole-zero plots of the estimated resonant filters hm,n for each resonant mode, where ‘o’ is zero and ‘x’ is pole.	52
Figure 3.12: (a) Magnitude and (b) phase of the velocity frequency response at $(0.3L_x, 0.1L_y)$	53
Figure 3.13: Sensor and point force arrangements on the simply supported beam.....	54
Figure 3.14: The sound power radiated from beam with primary force located at $x_0/l = 0.15$, estimated by ARM filters.	55
Figure 3.15: The individual sound powers radiated from beam with primary force located at $x_0/l = 0.15$, estimated by the first two ARM filters.	55
Figure 3.16: Location of sensors and point force on the clamped plate.....	56
Figure 3.17: The sound power radiated from plate with primary force located at $(x_0/L_x, y_0/L_y) = (0.15, 0.15)$, estimated by ARM filters.....	57
Figure 3.18: The individual sound powers radiated from plate with primary force located at $(x_0/L_x, y_0/L_y) = (0.15, 0.15)$, estimated by the first eight ARM filters.	58
Figure 4.1: Feedforward control system.....	63
Figure 4.2: The configuration of the sensors and the actuators for the feedforward control of the sound power radiated from a vibrating beam.	66
Figure 4.3: Theoretical and estimated frequency responses of the feedforward controllers using causal-delayed FIR filters for the case of cancellation of (a) the first, (b) the first two and (c) the first three ARM amplitudes, using the first, second and third control forces located at points $x_{s,1}/l = 0.5$, $x_{s,2}/l = 0.3$ and $x_{s,3}/l = 0.75$, respectively.	69
Figure 4.4: Time histories of the first three ARM amplitudes of beam for the cases of cancellation of (a) the first, (b) the first two, and (c) the first three ARM amplitudes, when the controllers are enabled at $t=5$ seconds.	70

Figure 4.5: The uncontrolled and controlled sound powers from beam, contributed by (a) the first ARM (W_1), (b) the second ARM (W_2) and (c) the third ARM (W_3).	72
Figure 4.6: The total radiated sound powers from the vibrating beam, controlled using feedforward control.	73
Figure 4.7: Block diagram of the filtered-x LMS algorithm.	75
Figure 4.8: Identification of secondary path using LMS algorithm.	78
Figure 4.9: Block diagram representation of the adaptive feedforward ASAC using FxLMS algorithm.	80
Figure 4.10: Time histories of the first three ARM amplitudes of the plate for cancellation of the first, (b) the first two, and (c) the first three ARM amplitudes, when the adaptive controllers are enabled at $t=50$ seconds.	82
Figure 4.11: The uncontrolled and controlled sound powers from plate, contributed by (a) the first ARM (W_1), (b) the second ARM (W_2) and (c) the third ARM (W_3).	83
Figure 4.12: The radiated sound powers from vibrating plate, controlled using adaptive controller.	85
Figure 4.13: Flowchart of Simple Ant Colony Optimisation (S-ACO).	88
Figure 4.14: ACO graph for optimisation of j^{th} control actuator location.	91
Figure 4.15: Convergence plots when optimizing (a) the first control actuator location, (b) the second control actuator location, and (c) the third control actuator location.	92
Figure 4.16: Permissible zone (in red colour) to place (a) the first (b) the second, and (c) the third control actuators.	93
Figure 4.17: Optimal actuator locations.	94
Figure 4.18: Time histories of the first three ARM amplitudes of plate using optimal control actuator locations, for cancellation of (a) the first, (b) the first two, and (c) the first three ARM amplitudes, when the adaptive controllers are enabled at $t=50$ seconds.	94
Figure 4.19: The radiated sound powers from vibrating plate using optimal control actuator locations, controlled using adaptive controller.	96
Figure 5.1: Clamped plate.	98
Figure 5.2: Floor plan of the acoustics laboratories at the University of Auckland.	99
Figure 5.3: View of reverberation chamber A and C when the wall between them is removed.	100
Figure 5.4: Location of the clamped plate on the wall between two reverberation chambers.	100
Figure 5.5: Location of the actuators on the plate (view from Chamber C).	102

Figure 5.6: Arrangements of accelerometers and shakers attached to the plate, viewed from (a) Reverberation chamber A and (b) Reverberation chamber C.....	103
Figure 5.7: Experimental setup.....	105
Figure 5.8: FIR filter coefficients for the (a) first, (b) second and (c) third secondary paths.	106
Figure 5.9: Velocity responses from the 3x3 array of sensors.	110
Figure 5.10: Radiated sound power measured according to ISO 3741, ARM estimates and statistical methods.	110
Figure 5.11: Attenuation of radiated sound power, tonal reference at various frequencies.	112
Figure 5.12: Third octave band attenuation of radiated sound power calculated according to ISO 3741, when the plate is excited by noise signal.	113

LIST OF TABLES

Table 2.1: Parameters of simply supported beam and fluid	24
Table 2.2: Natural frequency of the simply supported beam	24
Table 2.3: Parameters of clamped plate.....	33
Table.2.4: Natural frequencies of the clamped plate	33
Table 4.1: Locations of the secondary actuators	67
Table 4.2: Reduction of the radiated sound powers from beam.....	73
Table 4.3: Locations of the control actuators on the plate.....	79
Table 4.4: Convergence step-size.....	81
Table 4.5: Reduction of the radiated sound power from plate	85
Table 4.6: ACO parameters	91
Table 4.7: Optimal locations of the control actuators	93
Table 4.8: Reduction of the radiated sound power from plate using optimal control actuators	95
Table 5.1: Specification of the sensors	101
Table 5.2: Specification of the shaker model ET-132	102
Table 5.3: Locations of the control actuators on the plate.....	103
Table 5.4: Third octave band considered in the experiment.....	110
Table 5.5: Attenuation of the radiated sound power for tonal excitation, calculated using ARM estimates method	112
Table 5.6: Attenuation of the radiated sound power for noise excitation, calculated using ARM estimates method	114

NOMENCLATURE

Latin letters

A	Surface area
a_k	Feedback coefficients of the filter
b_b	Width of the beam
b_j	Feedforward coefficients of the filter
c_o	Speed of sound in air
d	Number of time steps delay
d_c	time-steps delay of the controller
d_p	Desired signal from primary path
d_s	Desired signal from the secondary path
D	Bending stiffness of the plate
E	Young's modulus
e	Error signal in discrete time
e_s	Error signal of the secondary path
f_l	Low cut-off frequencies
f_h	High cut-off frequencies
f_s	Sampling frequency
f_n	Nyquist frequency
f_{cr}	Critical frequency
f_p	Primary force
$f_{s,j}$	j^{th} secondary force
F_p	Primary force in frequency domain
F_s	Secondary force in frequency domain
G_p	Transfer function of primary path
G_s	Transfer function of secondary path
\hat{G}_s	Estimated transfer function of secondary path

g_p	Coefficients of the primary path filter
g_s	Coefficients of the secondary path filter
h_b	Thickness of the beam
h	Thickness of the plate
H_β	Frequency response of vibration mode β
\mathbf{H}_p	Vector of sensor transfer functions of the primary paths
\mathbf{H}_s	Vector of sensor transfer functions of the secondary paths
$H_{c,j}$	Control transfer function to the j^{th} secondary force
$h_{c,j}$	impulse response of $H_{c,j}$
I	Area moment of inertia
i	Imaginary unit i.e. $\sqrt{-1}$
J	Objective function
k	Wavenumber
K_1	Number of filter coefficients considered for the primary path filter
K_2	Number of filter coefficients considered for the secondary path filter
K_3	Number of filter coefficients considered for the controller filter
l	Length of the beam
L_k	Cost of the tour by ant k
L_x	Length of the plate
L_y	Width of the plate
m_b	Beam's mass per unit length
m_s	Plate's mass per unit area
m	Sample index (discrete time)
N	Total number (Elements / Sensors / ARMs / Structural modes)
N_r	Number of ARMs
N_s	Number of structural sensors
N_β	Number of resonance frequencies
p	Acoustic pressure
$P(t)$	Probability of paths selected by an ant at a given time (in ACO algorithm)
$q_{r,n}$	impulse response of $Q_{r,n}$
$Q_{r,n}$	r^{th} ARM at the n^{th} sensor location in frequency domain

Q	Eigenvectors a.k.a. acoustic radiation modes
Q_c	Controlled ARMs vector
r	Arbitrary position vector
<i>r</i>	Reference signal in discrete time
<i>t</i>	Time
<i>s</i>	Filter coefficients index
<i>T</i>	Set of all possible paths selected by an ant at time <i>t</i> (in ACO algorithm)
<i>u</i>	Input signal in discrete time
<i>v_n</i>	Velocity at <i>n</i> th sensor location
v	Velocity vector
v_p	Velocity vector caused by the primary force, <i>F_p</i>
v_s	Velocity vector caused by the secondary force, <i>F_s</i>
$\langle v ^2 \rangle$	Mean-square velocity
<i>V_n</i>	Velocity at the <i>n</i> th sensor location in frequency domain
<i>w_k</i>	Coefficients of the controller filter
<i>w(x, t)</i>	Transverse displacement at point <i>x</i> and time <i>t</i>
<i>w(x, y, t)</i>	Transverse displacement at the point (<i>x, y</i>) and time <i>t</i>
<i>W_r</i>	Radiated sound power contributed by <i>r</i> th ARM
<i>W</i>	Radiated sound power
\bar{W}	Statistical sound power
<i>y_r</i>	<i>r</i> th ARM amplitude
<i>Y_r</i>	<i>r</i> th ARM amplitude in frequency domain
y	ARM amplitude vector
y_c	Controlled ARM amplitudes vector
<i>z</i>	<i>z</i> domain (digital)

Greek letters

α	Relative importance of the pheromone values on the decision of an ant
Λ	Eigenvalues matrix
λ_r	<i>r</i> th eigenvalue
σ	Radiation efficiency

σ_r	r^{th} radiation efficiency
$\Phi_{pq}(x, y)$	mode shapes of the plate
$\varphi_p(x)$	mass normalised mode shapes of the beam
$\varphi_{\beta,n}$	Mode shape of mode β at n^{th} sensor location
δ_{pq}	Kronecker delta function
η_b	loss factor of the beam
η_s	Loss factor of the plate
τ	Sampling period
τ_{mn}	Pheromone trails
μ	Convergence step-size
$\mu_p(t)$	modal coordinates of p^{th} mode of the beam
$\mu_{pq}(t)$	modal coordinates of the $(p, q)^{\text{th}}$ mode of the plate
ν	Poisson's ratio
ω	Angular frequency
ω_p	p^{th} natural frequency of the beam
ω_{pq}	$(p, q)^{\text{th}}$ natural frequency of the plate

Subscripts

r	ARM index
c	control
p	Primary
s	Secondary
b	beam
k	filter index (in ACO algorithm)
n	Sensor index
β	Vibration mode index
p	Element index in x-direction
q	Element index in y-direction
j	Secondary force index

This form is to accompany the submission of any PhD that contains published or unpublished co-authored work. **Please include one copy of this form for each co-authored work.** Completed forms should be included in all copies of your thesis submitted for examination and library deposit (including digital deposit), following your thesis Acknowledgements. Co-authored works may be included in a thesis if the candidate has written all or the majority of the text and had their contribution confirmed by all co-authors as not less than 65%.

Please indicate the chapter/section/pages of this thesis that are extracted from a co-authored work and give the title and publication details or details of submission of the co-authored work.

Chapters 2 and 3 and Section 4.3

Md Nor, K., Mace, B., & Hioka, Y. (2016). Time-domain estimation of acoustic radiation modes and active structural acoustic control. In I. D. M. Hillock, D. J. Mee (Eds.) Proceedings of ACOUSTICS 2016 Brisbane, Queensland, Australia.

Nature of contribution by PhD candidate	Main author/ Majority of work
Extent of contribution by PhD candidate (%)	90

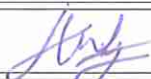
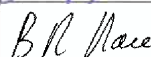
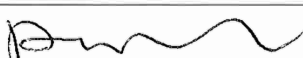
CO-AUTHORS

Name	Nature of Contribution
Khairul Affendy Bin Md Nor	Propose the original idea, do the theoretical analysis and simulation, and draft the paper.
Prof. Brian R. Mace	Main supervisor, advice research direction, paper structure and proofreading
Dr. Yusuke Hioka	Co-supervisor, advice research direction, paper structure and proofreading

Certification by Co-Authors

The undersigned hereby certify that:

- ❖ the above statement correctly reflects the nature and extent of the PhD candidate's contribution to this work, and the nature of the contribution of each of the co-authors; and
- ❖ that the candidate wrote all or the majority of the text.

Name	Signature	Date
Khairul Affendy Bin Md Nor		11/05/2018
Prof. Brian R. Mace		12/5/18
Dr. Yusuke Hioka		11/5/2018

Co-Authorship Form

This form is to accompany the submission of any PhD that contains published or unpublished co-authored work. **Please include one copy of this form for each co-authored work.** Completed forms should be included in all copies of your thesis submitted for examination and library deposit (including digital deposit), following your thesis Acknowledgements. Co-authored works may be included in a thesis if the candidate has written all or the majority of the text and had their contribution confirmed by all co-authors as not less than 65%.

Please indicate the chapter/section/pages of this thesis that are extracted from a co-authored work and give the title and publication details or details of submission of the co-authored work.

Chapters 2 and 3 and Section 4.4

Md Nor, K., Mace, B., & Hioka, Y. (2017). Adaptive control of radiated sound power based on time-domain estimates of acoustic radiation modes. Proceedings of International Congress on Sound and Vibration (ICSV 24), London, UK.

Nature of contribution by PhD candidate	Main author/ Majority of work
---	-------------------------------

Extent of contribution by PhD candidate (%)	90
---	----

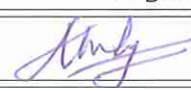


CO-AUTHORS

Name	Nature of Contribution
Khairul Affendy Bin Md Nor	Propose the original idea, do the theoretical analysis and simulation, and draft the paper.
Prof. Brian R. Mace	Main supervisor, advice research direction, paper structure and proofreading
Dr. Yusuke Hioka	Co-supervisor, advice research direction, paper structure and proofreading

Certification by Co-Authors

The undersigned hereby certify that:

- ❖ the above statement correctly reflects the nature and extent of the PhD candidate's contribution to this work, and the nature of the contribution of each of the co-authors; and
- ❖ that the candidate wrote all or the majority of the text.

Name	Signature	Date
Khairul Affendy Bin Md Nor		11/05/2018
Prof. Brian R. Mace		12/5/18
Dr. Yusuke Hioka		11/5/2018

CHAPTER 1 : INTRODUCTION

1.1 Overview

Recent technology advances in the automotive and aircrafts industries, requirement of improved fuel economy and environmental and socioeconomic factors have created consumer demands for lighter vehicles. Such vehicles, usually made of simple beams, plates, panels etc., are prone to noise and vibration problems caused by aerodynamic sources (e.g. turbulent boundary layer pressure fields on aircraft skins or on car bodyworks), by external sources (e.g. jet or reciprocating engine noise), and by structure-borne noise (e.g. engine induced or road induced vibrations) [1-2]. Impaired performance, degraded communication, increased fatigue, and hearing loss are some of the risks encountered by the passengers due to uncontrolled interior noise in the vehicle cabin. Thus, understanding of the vibro-acoustic characteristics of thin-walled enclosures typical of cabin structures is important, and necessary countermeasures need to be taken to reduce noise levels.

Acoustic noise transmission is often passively suppressed by adding mass, stiffening or damping material to the structure to reduce the undesired effects in the dynamic response of lightweight structures. This is done by introducing enclosures, barriers and silencers to the system to absorb or block the acoustic waves [3-4]. One of the successful examples is the use of Helmholtz resonators (HRs) to increase acoustical damping by tuning the parameters of HR (volume and neck dimensions) in order to tune the natural frequency of the HR to the frequency of the acoustic noise. [5-6]. They have been proven to be very efficient in controlling noise over a narrow frequency band and have been applied successfully in many acoustic enclosures [4, 7-8]. Besides, Leung et al. [9] utilised passive noise reduction through enhancement of aero-acoustic interference due to two cavities when considering a laminar flow.

Passive noise control can effectively reduce noise at mid and high frequencies. However, there is typically much less noise reduction at low frequencies, and reduction requires a substantial implementation cost with the addition of size and weight, simply because the acoustic wavelengths are much longer than the structure [4]. Advancements of

sensors, actuators and microprocessors nowadays have provided more possibilities for noise control, namely active noise control (ANC) and active structural acoustic control (ASAC), that could satisfy both the requirements for low weight and low vehicle interior noise levels. In ANC additional noise is introduced to cancel out unwanted noise, while in ASAC the vibration characteristics of the radiating surface are controlled to reduce the radiated sound power, without necessarily reducing the mean square vibrational velocity.

The thesis presents a method of estimating the radiated sound power of vibrating structures based on the time domain estimation of acoustic radiation modes (ARMs). These ARMs represents independent velocity patterns of the radiator that radiate sound to the far-field [10-11]. The benefit of the real-time estimates of ARM approach is that it gives broadband estimation of radiated sound power from strongly radiating vibration. A method of controlling the radiated sound power using the ASAC approach is also presented, where real-time ARM amplitudes are used as the cost function of the controller. Finally, physical experiments are conducted to validate the findings.

1.2 Literature review

1.2.1 Measurement of the radiated sound power

The accurate measurement of the radiated sound power is important in an active control system, since the objective is to suppress the sound radiation. Over many years, the radiated sound from a vibrating surface has been studied extensively, with a rectangular plate often considered [12-13]. The radiated sound pressure in the far-field can be calculated using Rayleigh integral [14] (equation 2.1), which is an integral over the surface of the vibrating plate. Alternatively the power can be estimated by integrating the far-field acoustic intensity over a hemisphere enclosing the plate [15]. These are chosen to be the standard methods of calculating the sound power and typically require a special acoustic environment, i.e. an anechoic or reverberation chamber [16].

In the 1990s, a new technique of estimating the sound power radiated from a vibrating structure using the radiation resistance matrix was proposed [10, 17]. This method discretises the radiator surface into elementary pistons and the radiated sound power is estimated as the product of the radiation resistance matrix, which relates the pressures and velocities of the

discrete elemental piston radiators, and the squared velocity vectors [4, 18]. The radiation resistance matrix contains mutual radiation impedances between the elementary pistons. Later, it was shown that the sound power radiated by a vibrating structure can be expressed as the sum of linear contributions of the acoustic radiation modes (ARMs), where these ARMs are the eigenvectors of the radiation resistance matrix [2, 10-11].

1.2.2 Acoustic radiation modes

In recent years, significant attention has been drawn to use the concept of ARMs in developing efficient design strategies for ASAC systems. ARMs can be defined as the velocity distributions that radiate power independently to the acoustic far-field. Physically, ARMs are basis vectors orthogonal to each other in vector space and each basis vector represents a possible velocity pattern that radiates sound independent of the other ARMs. Each ARM has a specific radiation efficiency, thus, the radiated power can be estimated as a superposition of the ARM contributions [10-11]. Sound power estimation using the ARMs approach eliminates the complex coupling terms in the structural vibration modes in the model. Besides, at low frequencies, often control of only a few ARMs is required, as compared to vibration modes. These simplify the calculation and active control of the structure-borne radiation.

The unique feature of ARMs is that they depend only on the radiator geometry and frequency. Thus, the far-field sound power can be estimated even without information of the mechanical properties and boundary conditions of the radiators [10]. The summation of the product of the ARM shape and the corresponding surface velocity produces the ARM amplitude. The radiated sound power W can then be calculated as

$$W = \sum_{j=1}^{\infty} \lambda_j |y_j|^2, \quad (1.1)$$

where y_j is the j^{th} ARM amplitude and λ_j is the eigenvalue of j^{th} ARM. Equally, by reducing the corresponding distributed surface velocities that contribute to the radiation modes with the most significant radiation efficiencies, which are normally the first few ARMs, by using actuators, the overall radiated sound power can be reduced considerably.

The ARM approach has been used by many researchers in sound radiation problems. Tao and Qiu [19] estimated the radiated sound power of lightly damped, baffled, simply supported rectangular plates by using ARMs and velocity sensors. A mapped ARM method proposed by Wu et al. [20] was used to simplify the ARM computation for convex structures, e.g. a sphere. Estimation of the radiated sound power from the structure-dependent radiation modes based on the modal velocity distributions was proposed by Ji et al. [21-22] as a replacement for the classical ARMs. Yamaguchi et al. [23] proposed the force radiation mode concept to understand the relationship between sound power and driving force distribution. Hesse et al. [24] estimated the acoustic potential energy of an enclosure using a frequency-independent radiation modes method.

1.2.3 Active control approaches

Rapid development of digital signal processors and A/D and D/A converters since 1990s, has made active control methods feasible in attenuating noise especially at low frequencies. Active control is realized by introducing additional signals to the system through a set of secondary actuators. The responses from these actuators are added to those of the primary actuators through superposition. With correct tuning, the additional inputs are able to modify the characteristic of the control system appropriately to yield the desired response. There are two types of active controls, namely active noise control (ANC) and active structural acoustic control (ASAC).

Active noise control was first introduced in 1936 in a patent by Lueg [25]. ANC uses secondary sources to generate a sound signal, which has equal magnitude and is 180 degrees out of phase with the unwanted noise signal, in order to cancel that noise [26-28]. Unwanted noise is often created due to vibrating structures. Active noise control methods that are based on modifying the sound field are not always effective for this type of problem.

The ASAC method however can reduce the complexity of controlling a 3-dimensional sound field to the 2-dimensional problem of controlling the vibration of a vibrating surface to suppress transmitted or radiated noise. This requires a smaller number of structural actuators to produce global far-field attenuation as compared to ANC [29-32]. It is an extension of a technique used to control vibration of a structure, called active vibration control (AVC) [31] but with a different cost function. The other difference between ASAC and AVC is their

control objective. The AVC technique is aimed at vibration reduction. However, some of the vibration modes, for example an even-even mode of a simply supported plate, is not an efficient radiator thus suppressing this mode will not reduce the radiated sound power significantly. In ASAC, the objective is to control only the vibrations which are important to sound radiation [31].

1.2.4 Active structural acoustic control

For the realisation of ASAC, numerous methods have been developed. For instance, Pinte et al. [33] proposed iterative learning control for active control of repetitive impact noise. The approaches of vibro-acoustic modes were proposed to control both sound and vibration simultaneously [34-36]. Bianchi et al. [37] and Gardonio et al. [38-39] developed a sound radiation control system using direct velocity feedback (DVF) with a collocated configuration of accelerometers and piezoelectric patches. Sound radiation from structural vibration modes was decoupled by investigating the ARMs and radiation modal expansion before application to practical real-time control [40-41]. With the identified model, the control system was designed according to a Hankel-Norm specification to suppress noise radiated from a vibrating structure [42]. Hesse et al. [24] used H_∞ control based on frequency-independent radiation modes to reduce the acoustic potential energy of a plate-cavity system under stochastic excitation.

Volume velocity is a measurable quantity on the surface of the plate and has a similar appearance to the lowest order ARM [10]. Volume velocity control has proven to be an effective strategy to reduce overall sound radiation especially at low frequencies, [43-44]. Gardonio et al. [45] applied direct velocity feedback control using a matched volume velocity sensor and a uniform force actuator bonded to a plate to control sound radiation. Good control results were achieved for excitation frequencies below 100 Hz. However, the controller was unstable at higher frequencies. This was due to the sensor-actuator response being controlled by the in-plane longitudinal and shear vibration of the panel. Implementation of volume velocity control requires a relatively large number of structural sensors. In the paper by Sors and Elliott [44], 62 sensors were used to estimate the volume velocity accurately for a steel rectangular plate whose smallest dimension was 483 mm [46]. Another control metric of ASAC for the low frequency range, termed the composite velocity, is based

on the weighted sum of the spatial velocity gradient (also known as WSSG). This was proposed by Fisher [47]. Using this method, control results comparable to volume velocity control were achieved but with fewer sensors [48-50]. However, both control methods are only applicable for the low frequency range (i.e. frequency range before the second ARM becomes important).

1.3 Motivation

One problem associated with ASAC is that the ARMs are frequency dependent: in frequency domain approaches the system is designed based on the ARM shape at a specific frequency, similar to the approximation of volume velocity approaches at low frequencies. Unlike frequency-domain approaches, time-domain methods enable a broader frequency range of approximation of radiated sound power [51] and allow for real-time implementation. However, few studies focus on calculating the radiated sound power using a time-domain approach. Borgiotti and Jones [52] estimated the sound power using frequency-independent radiation spatial filters, where they used ARMs weighted at a discrete frequency. At other frequencies, the ARM was normalised with respect to this frequency, thus the radiated sound power can only be measured accurately if all self and mutual radiation efficiencies are taken into account.

Later, the discrete structural acoustic sensing (DSAS) technique was proposed by Maillard [53]. His work provides time domain estimates of the radiated far-field sound pressure. Arrays of finite impulse response (FIR) filters, whose impulse responses were constructed from the appropriate Green function, were employed to process the measured acceleration signal in the time domain. Validation of the sensing technique was performed on a baffled rectangular plate and finite cylinder.

Berkhoff [51] identified the ARMs by extracting the underlying Green function using time-domain inverse filtering technique. Using this method, the ARMs obtained are the optimum vibration patterns in an average sense evaluated over a predefined frequency band and thus selection of a normalization frequency as in [52], was not required. The work of Wu [54] managed to calculate the sound power using time-domain acceleration distribution instead of velocity distribution.

However, none of the previous studies estimate the sound power from the time-domain estimates of the ARM itself. The ARM shape is frequency-dependent and can be reconstructed in the time domain using digital filters weighted across the frequency range of interest. Moreover, the real-time ARM amplitudes can be calculated from the convolution of the ARM filters and the corresponding velocity responses. These ARM amplitudes can also be used as the cost function in ASAC system. Addressing these issues is the scope of this thesis.

1.4 Objectives

This research focuses on developing a method of calculating and controlling the radiated sound power of vibrating structures based on the time domain estimation of ARMs. The main objectives of this research are:

1. to develop digital filters that estimate the ARMs and radiated sound power in the time domain,
2. to develop non-adaptive and adaptive feedforward controllers to attenuate the sound radiated from a structure using real-time ARM amplitude as an error function,
3. to determine the optimal location of the actuators used to control the sound radiation, and
4. to verify the simulation results experimentally.

1.5 Contributions

The main contributions of this thesis can be summarised as follows.

- In order to allow for real-time implementation, a method to estimate the ARM amplitude in the time domain using digital filter is proposed using a causal-delayed FIR filter, which is also called the ARM filter. This ARM filter is designed by introducing a time delay in the frequency response of the ARM estimator (Chapter 3).
- The ARM filter is then used to estimate the radiated sound power of one and two dimensional radiating structures. The ARM filters allow for the frequency dependence of the ARM shapes, and hence give a better approximation across the frequency range of interest (Chapter 3).

- Methods to use ARM estimates in active structural acoustic control on both non-adaptive and adaptive feedforward control system are proposed. Generally, the ASAC controller is designed in a way that it minimises the real-time ARM amplitudes. In the non-adaptive feedforward control case (applied on the beam radiator), the ARM estimates are used to derive the controller model, which is obtained from the transfer function ratio of the primary path to the secondary path and reconstructed in discrete time using an FIR filter. In the adaptive feedforward control case (applied on the plate radiator), the controller is designed using filtered-x least mean square (LMS) algorithm whereby the ARM estimates are used as the error functions of the adaptive controller (Chapter 4).
- A method to determine the optimal control actuator locations for adaptive control case (applied on the plate radiator) using offline optimisation is proposed. Here, the optimisation is done using ant colony optimisation (ACO) algorithm, although other optimisation algorithms can equally be used (Chapter 4).

1.6 Thesis outline

In the following chapter of this thesis, the theory of radiated sound power from vibrating structures is discussed. Numerical examples of the first few ARMs for one and two-dimensional structures are also presented. In Chapter 3, the method for estimating the ARM amplitudes and radiated sound power in real time, which is implemented in discrete time, is described. The method is described with reference to one and two-dimensional radiators, namely a simply supported beam and a clamped plate. Various forms of the digital filters used are discussed and numerical simulations are performed to verify the performance of the estimation method. Chapter 4 discusses control of radiated sound power using feedforward ASAC strategies. Here two control cases are considered. The first case is non-adaptive control applied to a baffled beam and the second is adaptive control using the filtered-X least mean square (FxLMS) algorithm applied to a baffled rectangular plate. Selection of optimal locations of the control actuators is also discussed. Chapter 5 presents the experimental results, which aim to validate the estimation and control of the radiated sound power from a vibrating plate using the ARM estimation approach. Finally, Chapter 6 concludes this thesis and some recommendations for future work are also presented.

CHAPTER 2 : RADIATED SOUND POWER FROM VIBRATING STRUCTURES AND ACOUSTIC RADIATION MODES

2.1 Introduction

This chapter discusses the acoustic pressure derived from the Rayleigh Integral equation. The corresponding radiated power is found by solving the integral of the product of acoustic pressure and particle velocity over the radiating surface. Alternatively, this radiated acoustic power can also be calculated using the superposition of radiation modes, i.e. the velocity distributions that radiated power independently to the acoustic far-field; the shapes of the acoustic radiation mode (ARM) vary with the excitation frequency. Numerical examples of the first few radiation modes for one and two-dimensional structures are also presented. Here, a simply supported beam and a rectangular clamped plate are selected as the one and two-dimensional structures. To simulate the radiated sound power, the structural response needs to be calculated first. Thus, the equations of motion of a beam and a plate are derived, together with some numerical examples of the structural mode shapes and radiated sound power. Finally numerical examples of the radiated sound powers are presented.

2.2 Radiated sound power from a plane radiating surface

A structure lies in a rigid baffle in the x - y plane with the origin of the coordinates lying at the centre of the structure (see Figure 2.1). The shape of the radiator is arbitrary, although the figure shows a rectangular radiator. An acoustic fluid occupies the half-space $z > 0$. The far field acoustic pressure can be estimated at an arbitrary position $\mathbf{r}(R, \theta, \phi)$ expressed in the spherical coordinate system, in terms of the velocity of the structure using the Rayleigh integral [14]

$$p(\mathbf{r}, t) = \frac{i\omega\rho_0}{2\pi} \int_A v(\mathbf{r}_0) e^{i\omega t} \frac{e^{-ik|\mathbf{r}-\mathbf{r}_0|}}{|\mathbf{r}-\mathbf{r}_0|} dA, \quad (2.1)$$

where ω is the angular frequency, k is the wavenumber, ρ_0 is the density of the fluid, A is the area of the structure, $\mathbf{r}-\mathbf{r}_0$ is the distance from the location on the vibrating surface to the observation point, and $v(\mathbf{r}_0)$ is the transverse velocity of the structure. For the far-field case, the distance $\mathbf{r}-\mathbf{r}_0$ is large compared to the characteristic dimension of the structure and can be approximated by $R \equiv |\mathbf{r}-\mathbf{r}_0|$ in the denominator. Thus, the time-independent far-field pressure in Equation (2.1) becomes

$$p(\mathbf{r}) = \frac{i\omega\rho_0}{2\pi R} \int_A v(\mathbf{r}_0) e^{-ik|\mathbf{r}-\mathbf{r}_0|} dA. \quad (2.2)$$

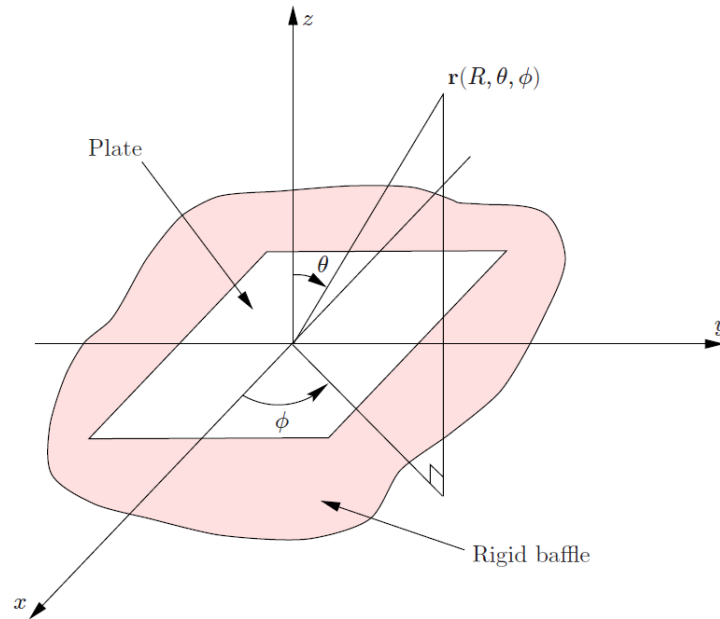


Figure 2.1: Coordinate system of plane baffled structure [55].

The time-averaged acoustic intensity at any observation point \mathbf{r} and direction is given by the product of the complex conjugate of particle velocity $v^*(\mathbf{r})$ and the complex acoustic pressure $p(\mathbf{r})$. Integrating the sound intensity over the surface of the radiator, the sound power radiated to the farfield by the structure equals [15]

$$W = \int_A \frac{1}{2} \text{Re} [v^*(\mathbf{r}) p(\mathbf{r})] dA. \quad (2.3)$$

Here, the evanescent component of the sound pressure is neglected. Substituting Equation (2.1) into Equation (2.3) yields

$$W = \frac{\omega \rho_0}{4\pi} \text{Re} \left[\iint_{AA} v(\mathbf{r}_p) \frac{ie^{-ik|\mathbf{r}-\mathbf{r}_0|}}{R} v^*(\mathbf{r}_q) dAdA \right] = \frac{\omega \rho_0}{4\pi} v(\mathbf{r}_p) \cdot \iint_{AA} \frac{\sin(k|\mathbf{r}-\mathbf{r}_0|)}{R} dAdA \cdot v^*(\mathbf{r}_q), \quad (2.4)$$

where \mathbf{r}_p and \mathbf{r}_q are any two arbitrary position vectors on the surface of the radiator. For practical implementation, the radiating surface can be discretised into N small elements of equal area ΔA , which converts the integration into a summation of elementary radiators.

The total radiated sound power of Equation (2.3) is expressed as

$$W = \frac{\omega \rho_0}{4\pi} \sum_{p=1}^N \sum_{q=1}^N v_p \frac{\sin(kr_{pq})}{r_{pq}} v_q^* (\Delta A)^2, \quad (2.5)$$

where v_p and v_q are the complex velocities of the p^{th} and q^{th} elements normal to the surface, respectively, $r_{pq} = |\mathbf{r}_p - \mathbf{r}_q|$ is the distance between the p^{th} element and the q^{th} element. Equation (2.5) can also be re-written in a vector-matrix form as [10]

$$W = \mathbf{v}^H \mathbf{M} \mathbf{v}, \quad (2.6)$$

where superscript H is the Hermitian transpose, \mathbf{v} is the velocity vector whose entries are the elemental velocities and \mathbf{M} is the radiation resistance matrix whose entries are given by

$$M_{pq} = \frac{\omega^2 \rho_0 (\Delta A)^2}{4\pi c_0} \begin{cases} 1 & p = q, \\ \frac{\sin(kr_{pq})}{kr_{pq}} & p \neq q. \end{cases} \quad (2.7)$$

2.3 Acoustic radiation modes

The radiation resistance matrix \mathbf{M} in Equation (2.7) is real and symmetric because of reciprocity. Also, due to the fact the radiated sound power is always greater than zero, except for the case where the surface velocity of the radiator is zero, \mathbf{M} is positive semi-definite. Thus, matrix \mathbf{M} can be diagonalised through an orthogonal transformation and written as

$$\mathbf{M} = \mathbf{Q}\mathbf{\Lambda}\mathbf{Q}^T, \quad (2.8)$$

where the superscript T is the transpose, $\mathbf{\Lambda} = \{\lambda_1 \dots \lambda_r\}^T$ is the vector of the eigenvalues of \mathbf{M} , ordered such that $\lambda_{r+1} < \lambda_r$, and \mathbf{Q} is a matrix whose columns are the orthogonal eigenvectors of \mathbf{M} . Each eigenvector in \mathbf{Q} is known as an acoustic radiation mode (ARM). ARMs are functions of position and frequency only but not boundary conditions, hence are not dependent on the natural modes of the structure but only on the shape of the radiating surface. Each ARM represents a possible velocity pattern of the radiator's surface and has a radiation efficiency related to the eigenvalue λ .

The radiation efficiency is defined as the ratio of the spatial acoustic power \bar{W} radiated by a vibrating structure to the average acoustic power radiated by a piston of the same surface area vibrating with the same mean-square velocity $\langle |v|^2 \rangle$ of the structure [56], i.e.

$$\sigma = \frac{\bar{W}}{\rho_0 c_0 \langle |v|^2 \rangle}, \quad (2.9)$$

where

$$\langle |v|^2 \rangle = \frac{1}{2A} \sum_{n=1}^N |v_n|^2 \Delta A. \quad (2.10)$$

Thus, the radiation efficiency of the individual ARM r is given by [57]

$$\sigma_r = \frac{2N}{\rho_0 c_0 A} \lambda_r. \quad (2.11)$$

The radiated sound power contributed by the r^{th} ARM is given by

$$W_r = |y_r|^2 \lambda_r, \quad (2.12)$$

where y_r is the r^{th} ARM amplitude, while the total radiated acoustic power of a vibrating structure W is determined by the summation of the sound power radiated from each ARM, as [10-11]

$$W = \mathbf{y}^H \Lambda \mathbf{y} = \sum_{r=1}^{N_r} W_r, \quad (2.13)$$

where $\mathbf{y} = \{y_1 \dots y_r\}^T = \mathbf{Q}^T \mathbf{v}$ is the vector of ARM amplitudes and N_r is the total number of ARMs. Equation (2.13) shows that the radiated acoustic power of one ARM is completely independent of all others. In other words, suppressing an individual radiation mode amplitude will reduce the total radiated power by an amount which depends on the contribution that particular radiation mode gives to the total radiated power. This is basically the essence of active structural acoustic control (ASAC), as mentioned in Chapter 1.

2.3.1 Numerical example: One dimensional radiator

Figure 2.2 shows the first six ARM shapes of a one-dimensional radiating plane structure, e.g. a baffled beam, when excited in the frequency range of $kl=0$ to $kl=10$, where kl is the dimensionless frequency, $k=\omega/c_0$ is the wavenumber, l is the length of the structure and x represents position on the beam. At low frequencies, i.e. $kl \leq 1$, the velocity distributions for the first two ARMs are similar to monopole-like and dipole-like motions, respectively. The higher ARMs are characterised by higher order functions. As frequency increases, their

shapes become more curved. Note that the ARM shapes are frequency dependent, in contrast to, for example, vibration mode shapes.

Using Equation (2.11), the radiation efficiencies of the first six ARMs of the radiator are shown in Figure 2.3. In general, the efficiency increases as frequency increases. It can be seen that the lower order ARMs are substantially more efficient radiators at low frequencies. This means that significant attenuation of the total radiated sound power at low frequencies can be achieved by controlling the sound power of only the first few ARMs. At higher frequencies, the efficiencies approach a constant value of 1.

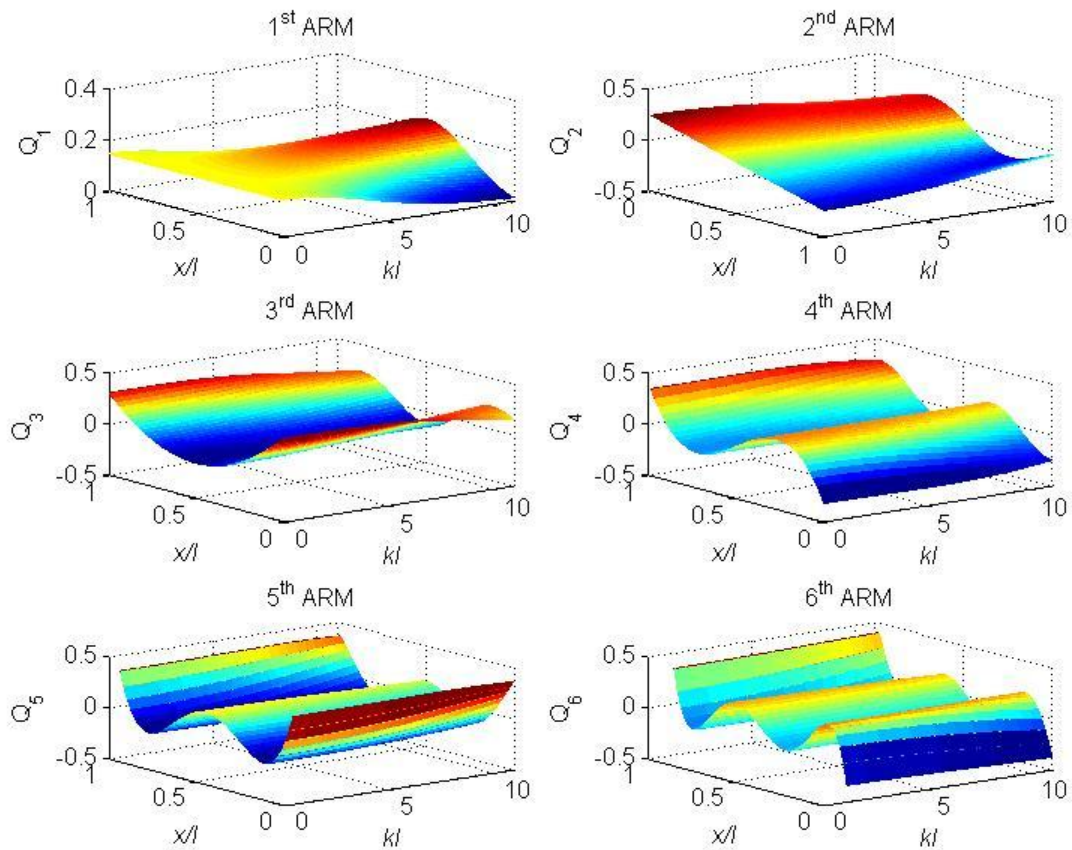


Figure 2.2: The first six ARMs of a one-dimensional baffled structure as functions of position and dimensionless frequency kl .

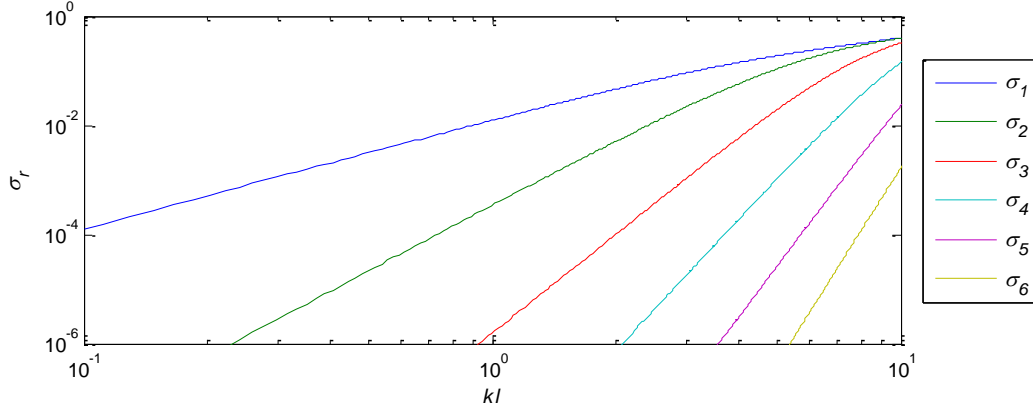
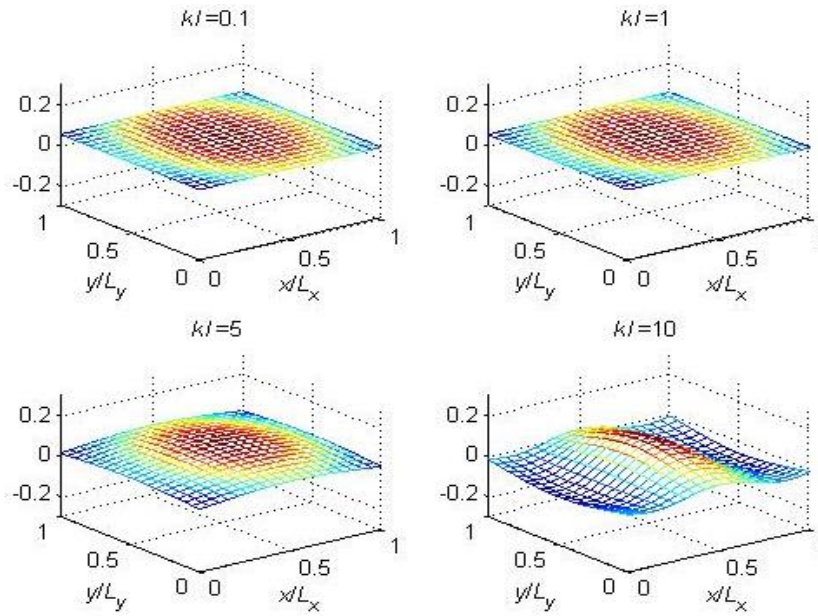


Figure 2.3: Radiation efficiencies of individual ARMs for 1-D radiator.

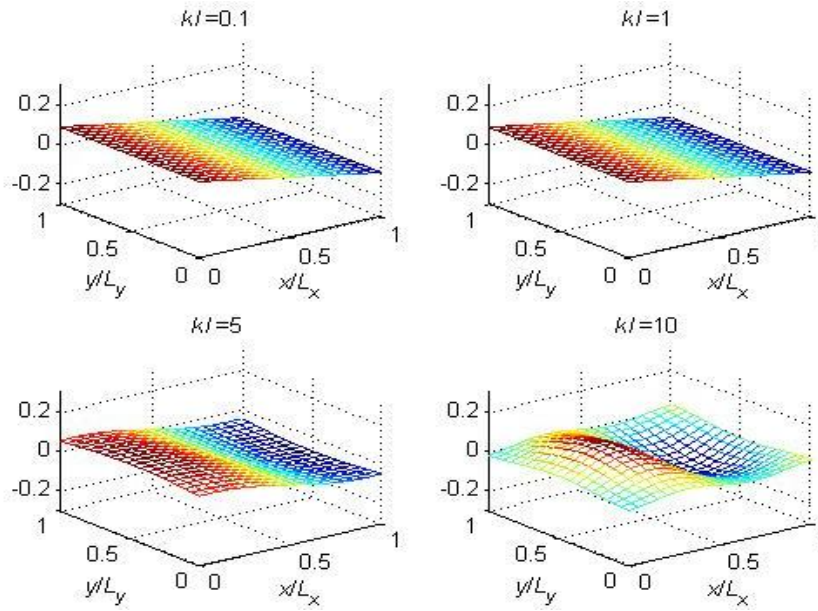
2.3.2 Numerical example: Two dimensional radiator

The two-dimensional radiator selected as a reference model is a rectangular plate with length $L_x = l$ and width $L_y = 0.75l$. Figure 2.4 shows the first four ARM shapes of the two-dimensional radiator. In this figure, the first ARM shape is nearly uniform over the surface of the radiator at low frequencies, i.e. $kl \leq 1$, whereas it is distorted towards a dome-shape at higher frequencies. The second and third modes are rocking-type, dipole-like modes oriented along the two axes of the panel at low frequencies and become distorted as the frequency increases. The fourth ARM is defined by the shape of higher order functions which have maximum and minimum values located at the two opposite vertices and becomes distorted at higher frequencies. Note again that these shapes are frequency dependent, which are quite the opposite to vibration mode shapes.

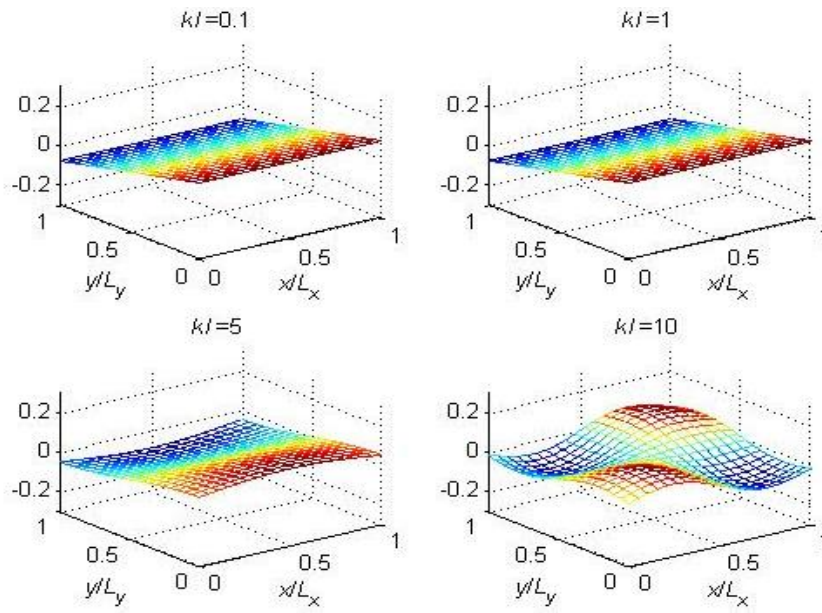
The radiation efficiencies of the first five ARMs of the plate are shown in Figure 2.5. From this figure, similar to the beam case, the lower ARMs are seen to be more efficient radiators especially at low frequencies; in other words, they generally contribute more to the radiated sound power than the higher ARMs. Note also the efficiencies for the second and third ARMs as well as also for the fourth and fifth ARMs are nearly equal due to the aspect ratio L_y/L_x being near to unity. The efficiencies increase as the frequency increases and finally tend to 1.



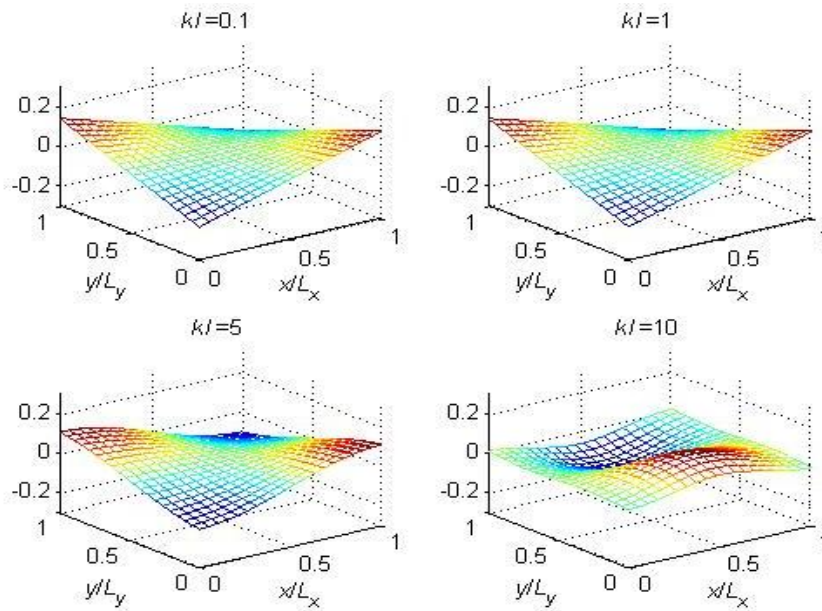
(a)



(b)



(c)



(d)

Figure 2.4: (a) First, (b) second, (c) third and (d) fourth ARM shapes of a rectangular 2-D structure when dimensionless frequency $kl = 0.1, 1, 5$ and 10 , respectively.

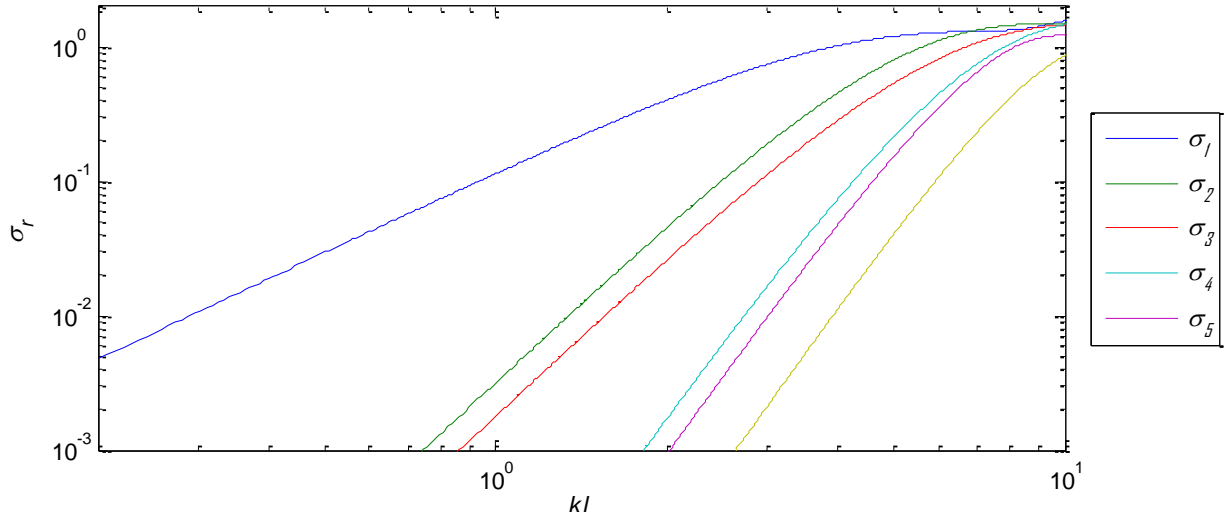


Figure 2.5: Radiation efficiencies of individual ARMs of the plate.

2.4 Equation of motion of the radiators

In this research, a thin simply supported beam and a thin, rectangular, clamped plate are used to simulate the one and two-dimensional radiators, respectively. This section presents the equations of motion and the developed expressions for the frequency response functions (FRFs) in terms of modal sums. Finally numerical examples of the structural mode shapes and the radiated sound power are presented.

2.4.1 Simply supported beam

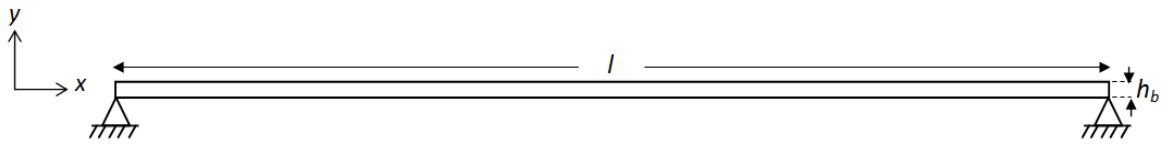


Figure 2.6: Thin beam.

Consider a thin beam of width b , thickness h_b and length l lying along the x -axis as shown in Figure 2.6. The half-space (x, y) above the beam is occupied by an acoustic fluid. Euler-Bernoulli beam theory is used to model the behaviour. For a uniform beam that undergoes undamped free vibration, the governing equation of motion can be obtained as [58]

$$EI \frac{\partial^4 w(x,t)}{\partial x^4} + m_b \frac{\partial^2 w(x,t)}{\partial t^2} = 0, \quad (2.14)$$

where $w(x,t)$ is the transverse displacement of the neutral axis (at point x and time t) due to bending, E is the Young's modulus, m_b is the mass per unit length of the beam, $I = bh_b^3/12$ is the area moment of inertia.

Using the modal analysis approach, the displacement can be separated into space and time functions of the form

$$w(x,t) \approx \sum_p \varphi_p(x) \mu_p(t), \quad (2.15)$$

where $\varphi_p(x)$ and $\mu_p(t)$ are the mass normalised mode shapes and the modal coordinates, respectively. Substituting Equation (2.15) into Equation (2.14) yields

$$\frac{1}{\varphi_p(x)} \frac{\partial^4 \varphi_p(x)}{\partial x^4} = -\frac{m_b}{EI} \frac{1}{\mu_p(t)} \frac{\partial^2 \mu_p(t)}{\partial t^2}. \quad (2.16)$$

Since the left side of Equation (2.16) is independent of time t and the right side is independent of x , the equality holds for all values of t and x . Assuming each side of Equation (2.16) to be equal to α_p^4 , the variables can be separated into

$$\frac{\partial^4 \varphi_p(x)}{\partial x^4} - \alpha_p^4 \varphi_p(x) = 0, \quad (2.17)$$

$$\frac{\partial^2 \mu_p(t)}{\partial t^2} + \omega_p^2 \mu_p(t) = 0, \quad (2.18)$$

where ω_p is the p^{th} natural frequency and the relationship between ω_p and α_p is given by

$$\omega_p^2 = \frac{EI \alpha_p^4}{m_b}. \quad (2.19)$$

The general solution to the differential equation, i.e. Equation (2.17), is

$$\varphi_p(x) = A_1 \sin(\alpha_p x) + A_2 \cos(\alpha_p x) + A_3 \sinh(\alpha_p x) + A_4 \cosh(\alpha_p x), \quad (2.20)$$

where A_1 , A_2 , A_3 and A_4 are constants. For the simply supported beam, the boundary conditions are

$$\varphi(x) = \frac{\partial^2 \varphi(x)}{\partial x^2} = 0 \text{ at } x=0 \text{ and } x=l. \quad (2.21)$$

Substituting Equation (2.20) into the boundary conditions in Equation (2.21) yields

$$A_2 = A_3 = A_4 = 0, \quad (2.22)$$

$$\alpha_p = \frac{p\pi}{l}, \quad (2.23)$$

$$\varphi_p(x) = A_1 \sin\left(\frac{p\pi}{l}x\right). \quad (2.24)$$

Substituting Equation (2.23) into Equation (2.19), the p^{th} natural frequency of the beam is

$$\omega_p = \sqrt{\frac{EI}{m_b}} \left(\frac{p\pi}{l}\right)^2. \quad (2.25)$$

The vibration modes are orthogonal. Substituting Equation (2.19) into Equation (2.18) yields

$$EI \frac{\partial^4 \varphi_p(x)}{\partial x^4} - \omega_p^2 m_b \varphi_p(x) = 0. \quad (2.26)$$

Similarly for mode q ,

$$EI \frac{\partial^4 \varphi_q(x)}{\partial x^4} - \omega_p^2 m_b \varphi_q(x) = 0. \quad (2.27)$$

Multiplying Equation (2.26) and Equation (2.27) by $\varphi_p(x)$ and $\varphi_q(x)$, respectively, and integrating over the length of the beam yields

$$\omega_p^2 \int_0^l m_b \varphi_p(x) \varphi_q(x) dx - \int_0^l EI \varphi_q(x) \frac{\partial^4 \varphi_p(x)}{\partial x^4} dx = 0, \quad (2.28)$$

$$\omega_q^2 \int_0^l m_b \varphi_p(x) \varphi_q(x) dx - \int_0^l EI \varphi_p(x) \frac{\partial^4 \varphi_q(x)}{\partial x^4} dx = 0. \quad (2.29)$$

Subtracting Equation (2.28) from Equation (2.29) yields

$$(\omega_p^2 - \omega_q^2) \int_0^l m_b \varphi_p(x) \varphi_q(x) dx = \int_0^l EI \left(\varphi_q(x) \frac{\partial^4 \varphi_p(x)}{\partial x^4} - \varphi_p(x) \frac{\partial^4 \varphi_q(x)}{\partial x^4} \right) dx. \quad (2.30)$$

Performing integration by parts on the right side of Equation (2.30) and applying boundary conditions from Equation (2.21) yields

$$(\omega_p^2 - \omega_q^2) \int_0^l m_b \varphi_p(x) \varphi_q(x) dx = 0. \quad (2.31)$$

Taking into account the fact that $\omega_p \neq \omega_q$ if $p \neq q$, then Equation (2.31) is reduced to

$$\int_0^l m_b \varphi_p(x) \varphi_q(x) dx = \delta_{pq}, \quad (2.32)$$

where δ_{pq} is the Kronecker delta function defined by

$$\delta_{pq} = \begin{cases} 0 & \text{if } p \neq q, \\ 1 & \text{if } p = q. \end{cases} \quad (2.33)$$

Equation (2.32) implies orthogonality of eigenfunctions with respect to the mass distribution. For a simply supported beam, the mass-normalised mode shape is given by

$$\varphi_p(x) = \sqrt{\frac{2}{m_b l}} \sin\left(\frac{p\pi x}{l}\right). \quad (2.34)$$

Substituting Equation (2.32) into Equation (2.28), performing integration by part on the left side of the equation, and applying boundary conditions, yields

$$\int_0^l EI \frac{\partial^2 \varphi_p(x)}{\partial x^2} \frac{\partial^2 \varphi_q(x)}{\partial x^2} dx = \omega_p^2 \delta_{pq}, \quad (2.35)$$

which implies that the eigenfunctions are orthogonal with respect to the stiffness distribution.

The response to external excitation is now expressed in terms of modal contributions. The equation of motion of a uniform beam subjected to an external force $f(x,t)$ per unit length is given by [58]

$$EI \frac{\partial^4 w(x,t)}{\partial x^4} + m_b \frac{\partial^2 w(x,t)}{\partial t^2} = f(x,t). \quad (2.36)$$

Substituting Equation (2.15) into Equation (2.36) gives

$$EI \frac{\partial^4}{\partial x^4} \sum_{p=1}^{\infty} \varphi_p(x) \mu_p(t) + m_b \frac{\partial^2}{\partial t^2} \sum_{p=1}^{\infty} \varphi_p(x) \mu_p(t) = f(x,t). \quad (2.37)$$

Multiplying both sides of Equation (2.37) by the mass-normalised mode shapes $\varphi_q(x)$ and integrating over the length of the beam, yields

$$\begin{aligned} \sum_{p=1}^{\infty} \mu_p(t) \int_0^l \varphi_q(x) EI \frac{\partial^4}{\partial x^4} \varphi_p(x) dx + \sum_{p=1}^{\infty} \frac{\partial^2}{\partial t^2} \mu_p(t) \int_0^l \varphi_q(x) m_b \varphi_p(x) dx \\ = \int_0^l \varphi_q(x) f(x,t) dx \end{aligned} \quad (2.38)$$

Substituting the orthogonality relations of Equations (2.32) and (2.35) into Equation (2.38) and considering the boundary conditions given by Equation (2.21), the equation reduces to

$$\frac{\partial^2}{\partial t^2} \mu_p(t) + \omega_p^2 \mu_p(t) = F_p(t), \quad (2.39)$$

where

$$F_p(t) = \int_0^l \varphi_p(x) f(x,t) dx, \quad (2.40)$$

is the generalised force on mode p . Using the Duhamel integral, the solution for Equation (2.39) for zero initial conditions can be expressed as

$$\mu_p(t) = \frac{1}{b\omega_p} \int_0^t F_p(\tau) \sin \omega_p(t-\tau) dt. \quad (2.41)$$

In real life, free vibration of any structure will die gradually due to the internal damping effect. It is found that in practice the presence of damping can be included for time harmonic behaviour by allowing the elastic modulus to be complex, i.e. $E = E(1 + i\eta_b)$, where η_b is the loss factor of the beam and is generally much smaller than unity. Assuming the external force $f(x,t) = Fe^{i\omega t} \delta(x-x_0)$ is a time harmonic point force of frequency ω and amplitude F acting at point x_0 , Equation (2.41) becomes [59]

$$\mu_p(t) = \frac{\varphi_p(x_0) Fe^{i\omega t}}{\omega_p^2(1 + i\eta_b) - \omega^2}. \quad (2.42)$$

Thus, from Equation (2.15), the response of the beam becomes

$$w(x,t) = \sum_{p=1}^{\infty} \frac{\varphi_p(x) \varphi_p(x_0) Fe^{i\omega t}}{\omega_p^2(1 + i\eta_b) - \omega^2}, \quad (2.43)$$

and is hence a sum of contributions from the modes of vibration. The surface velocity of the beam at point x_n is, in the frequency domain for time harmonic excitation, [57, 60]

$$V_n(\omega) = i\omega \sum_{p=1}^{\infty} \frac{\varphi_p(x_0)\varphi_p(x_n)}{\omega_p^2(1+i\eta_b) - \omega^2} F. \quad (2.44)$$

2.4.1.1 Numerical simulation: Structural mode shapes and natural frequencies

The parameters of the simply supported beam used in the numerical examples are given in Table 2.1. The mass-normalised mode shapes of the beam are shown in Figure 2.7 and the natural frequencies are given in Table 2.2. There are 5 structural modes within the frequency range up to 1 kHz.

Table 2.1: Parameters of simply supported beam and fluid

Parameter	Value
Length l	0.5 m
Width b	0.04 m
Thickness h_b	0.004 m
Density of beam ρ_b	7800 kg m ⁻³
Young Modulus E	200 GPa
Loss factor η_b	0.02
Density of air, ρ_0	1.239 kg m ⁻³
Speed of sound in air, c_0	340 m s ⁻¹

Table 2.2: Natural frequency of the simply supported beam

Mode number	1	2	3	4	5
Frequency (Hz)	36.7	147.0	330.6	587.8	918.5

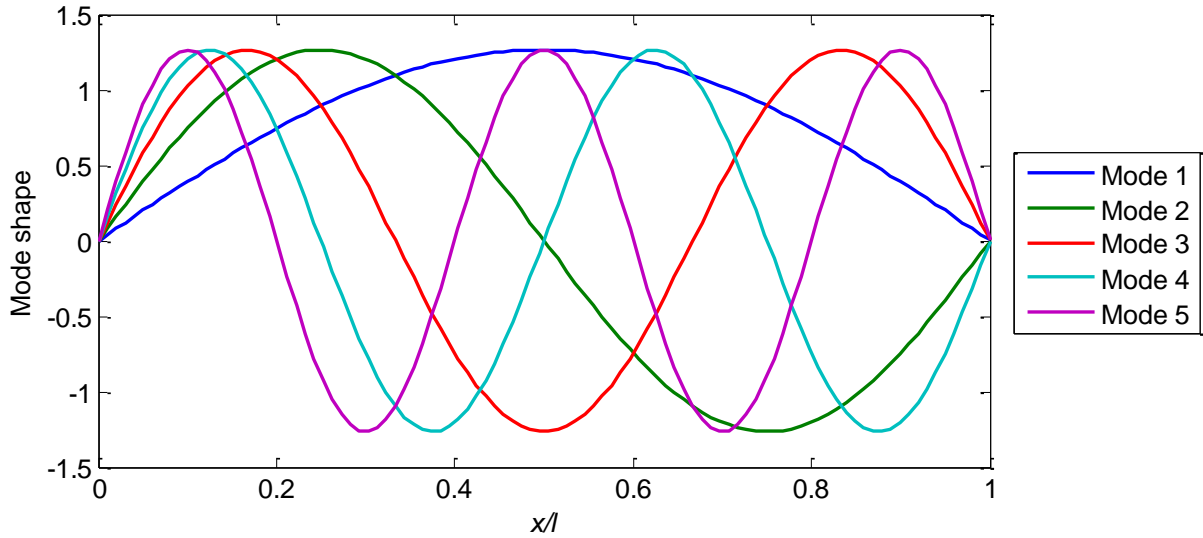


Figure 2.7: Mode shapes of a simply supported beam.

2.4.1.2 Numerical simulation: Radiated sound power of beam radiator

Suppose the beam is excited by a point force at $x_0 = 0.075$ m. The radiated sound power of the beam calculated from Equation (2.12) and Equation (2.13) are shown in Figure 2.8. From the total sound power plot (black line), there are 5 peaks corresponding to 5 natural frequencies and 3 ARMs with radiation efficiencies greater than 0.1 below 1 kHz. It can be seen that there is strong radiation around the structural resonances due to the large response at the resonance frequencies.

Figure 2.9 shows the ratio of the sound power contributed by the individual ARMs to the total sound power. For the lower frequency range below 110 Hz, the power is dominantly contributed by the first ARM. The second ARM begins to radiate power efficiently near the second resonance frequency while the third ARM begins near the fifth resonance frequency. It is also shown in the figure that the first ARM does not radiate significant power around the second and the fourth resonance frequencies. This is due to the asymmetric nature of the second and fourth structural mode shapes that have zero displacement, hence velocity, at the centre of the beam. These modes dominate the response and the total radiated power around their natural frequencies. As shown earlier in Figure 2.2, at higher frequencies, the first ARM radiates more power from the central region of the beam and less power from the beam's edges. Similar statements can be made for the second ARM which does not radiate power near the third resonance frequency, as the second ARM radiates less power at the centre

region of the beam due to its dipole-like ARM shape. All these phenomena are due to the fact that for both vibration and acoustic radiation modes, the odd modes are symmetric, while the even modes are antisymmetric. Around one resonance, one vibration mode dominates, and hence only ARMs with similar symmetry are the strong radiators. For this particular case, the radiated sound power of the beam for frequencies up to 1 kHz is mostly determined by the first 3 ARMs.

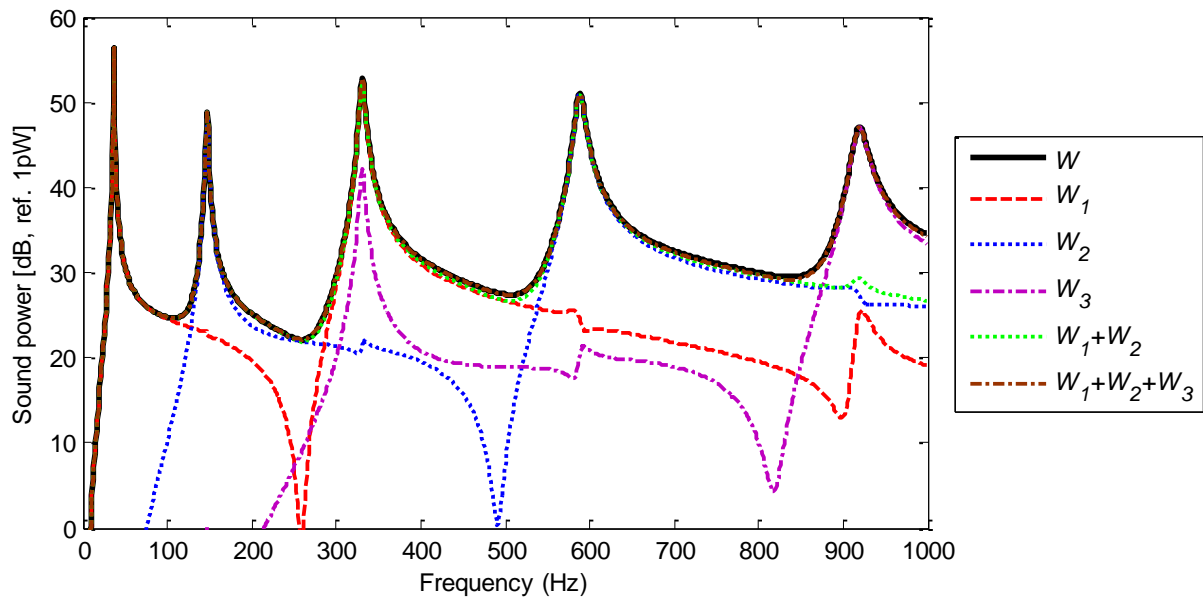


Figure 2.8: Radiated sound power of beam radiator.

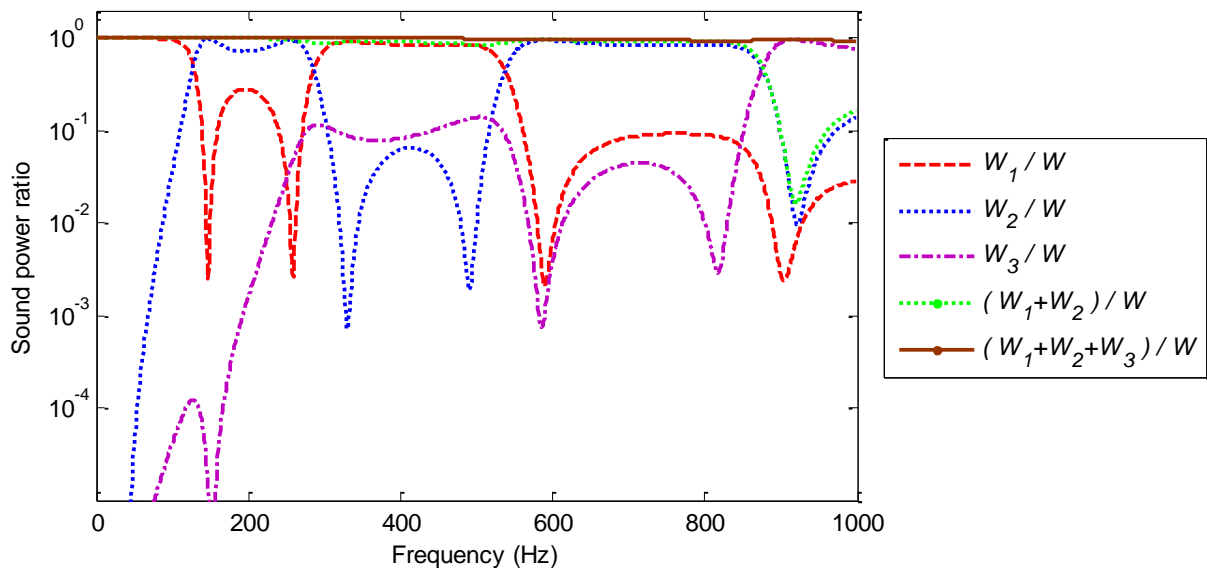


Figure 2.9: Ratio of sound powers of individual ARMs to the total sound power of beam radiator.

2.4.2 Clamped rectangular plate

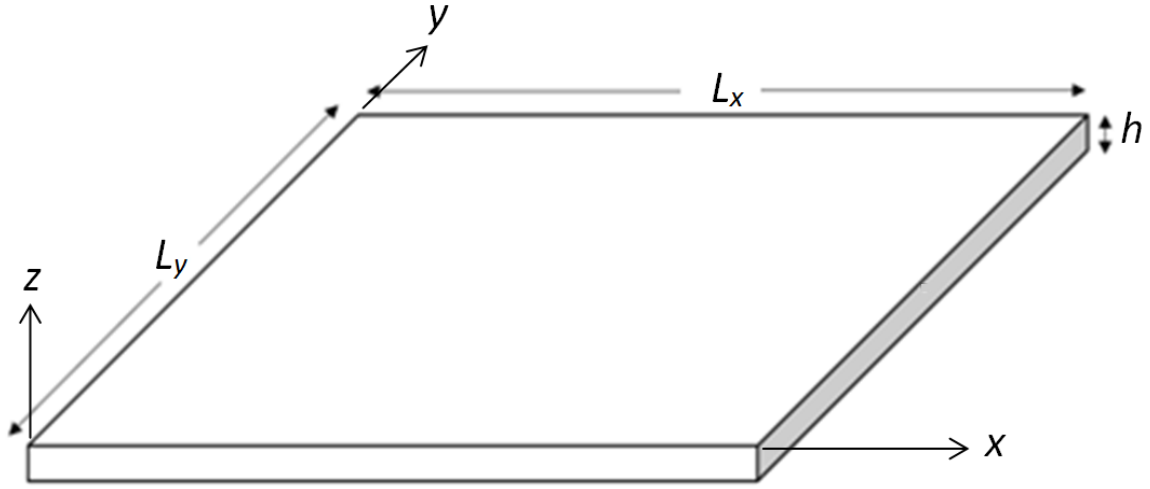


Figure 2.10: Thin plate.

Suppose the two-dimensional radiating surface is a rectangular thin plate. Assuming the classical Kirchhoff thin plate theory (i.e. the plate is thin with respect to the wavelength and rotary inertia and shear deformation of the cross-section are neglected), the deformations can be described entirely in terms of the deformation of the mid-surface plane; hence, the plate is reduced to the study of a two-dimensional problem consisting of the plate mid-surface. The plate lies in the region $0 \leq x \leq L_x$ and $0 \leq y \leq L_y$ as shown in Figure 2.10 and is subjected to an external pressure excitation $f(x, y, t)$. The governing equation of bending vibration is given by the Kirchhoff equation [61]

$$D \left(\frac{\partial^4}{\partial x^4} + 2 \frac{\partial^4}{\partial x^2 \partial y^2} + \frac{\partial^4}{\partial y^4} \right) w(x, y, t) + m_s \frac{\partial^2 w(x, y, t)}{\partial t^2} = f(x, y, t), \quad (2.45)$$

where $w(x, y, t)$ is the transverse displacement in the z direction at the point (x, y) , $D = Eh^3/12(1-\nu^2)$ is the plate's bending stiffness, E is the Young's modulus, h is the plate thickness, ν is the Poisson's ratio, and m_s is the mass per unit area of the plate material. In the homogeneous form, Equation (2.45) becomes

$$D \left(\frac{\partial^4}{\partial x^4} + 2 \frac{\partial^4}{\partial x^2 \partial y^2} + \frac{\partial^4}{\partial y^4} \right) w(x, y, t) + m_s \frac{\partial^2 w(x, y, t)}{\partial t^2} = 0. \quad (2.46)$$

The displacement $w(x, y, t)$ can be expressed as the superposition of an infinite number of mode shape functions $\Phi_{pq}(x, y)$ as in the case of a beam in section 2.4.1. Here the approximation

$$w(x, y, t) \approx \sum_{p=1}^{\infty} \sum_{q=1}^{\infty} \Phi_{pq}(x, y) \mu_{pq}(t) \quad (2.47)$$

is used, where μ_{pq} is the modal amplitude of the $(p, q)^{\text{th}}$ mode of the plate, and p and q are the mode number in x - and y -directions, respectively. Substituting Equation (2.47) into Equation (2.46) yields

$$-\frac{D/m_s}{\Phi_{pq}(x, y)} \nabla^4 \Phi_{pq}(x, y) = \frac{1}{\mu_{pq}(t)} \frac{\partial^2 \mu_{pq}(t)}{\partial t^2}, \quad (2.48)$$

where $\nabla^4 = \frac{\partial^4}{\partial x^4} + 2 \frac{\partial^4}{\partial x^2 \partial y^2} + \frac{\partial^4}{\partial y^4}$ is the biharmonic operator. Let each side of Equation (2.48) equal γ_{pq}^4 , thus the variables can be separated into

$$\nabla^4 \Phi_{pq}(x, y) - \gamma_{pq}^4 \Phi_{pq}(x, y) = 0, \quad (2.49)$$

$$\frac{\partial^2 \mu_{pq}(t)}{\partial t^2} + \omega_{pq}^2 \mu_{pq}(t) = 0, \quad (2.50)$$

where ω_{pq} is the $(p, q)^{\text{th}}$ natural frequency and

$$\gamma_{pq}^4 = \frac{m_s \omega_{pq}^2}{D}. \quad (2.51)$$

As an assumption, it is now assumed that the mode shape functions are written as the product of two independent beam functions [62-63]

$$\Phi_{pq}(x, y) = \varphi_p(x) \varphi_q(y), \quad (2.52)$$

where the function $\varphi_p(x)$ is the p^{th} mode shape for a clamped-clamped beam. General solution to the differential equation, i.e. Equation (2.49), is given by

$$\varphi_p(x) = A_1 \sin(\alpha_p x) + A_2 \cos(\alpha_p x) + A_3 \sinh(\alpha_p x) + A_4 \cosh(\alpha_p x), \quad (2.53)$$

where A_1, A_2, A_3 and A_4 are constants. The mode shape functions $\varphi_p(x)$ and $\varphi_q(y)$ in Equation (2.52) can be arbitrarily chosen if and only if they are orthogonal i.e.

$$\int_0^{L_x} \varphi_p(x) \varphi_j(x) dx = \int_0^{L_x} \frac{\partial^2 \varphi_p(x)}{\partial x^2} \frac{\partial^2 \varphi_j(x)}{\partial x^2} dx = 0 \quad \text{if } p \neq j, \quad (2.54)$$

$$\int_0^{L_y} \varphi_q(y) \varphi_k(y) dy = \int_0^{L_y} \frac{\partial^2 \varphi_q(y)}{\partial y^2} \frac{\partial^2 \varphi_k(y)}{\partial y^2} dy = 0 \quad \text{if } q \neq k, \quad (2.55)$$

and both of them satisfy the boundary conditions given by

$$\begin{aligned} \varphi(x) = \frac{\partial \varphi(x)}{\partial x} = 0 \quad \text{at } x=0 \quad \text{and } x=L_x, \\ \varphi(y) = \frac{\partial \varphi(y)}{\partial y} = 0 \quad \text{at } y=0 \quad \text{and } y=L_y. \end{aligned} \quad (2.56)$$

Substituting Equation (2.53) into the boundary conditions in Equation (2.56) yields [62]

$$\varphi_p(x) = \cosh\left(\frac{\alpha_p x}{L_x}\right) - \cos\left(\frac{\alpha_p x}{L_x}\right) - \frac{\cosh(\alpha_p) - \cos(\alpha_p)}{\sinh(\alpha_p) - \sin(\alpha_p)} \left[\sinh\left(\frac{\alpha_p x}{L_x}\right) - \sin\left(\frac{\alpha_p x}{L_x}\right) \right], \quad (2.57)$$

where α_p and α_q are the roots of the equation $\cosh(\alpha)\cos(\alpha)=1$.

From Equation (2.48), using the orthogonality relationship in Equations (2.54) and (2.55), the natural frequencies are given by [62]

$$\omega_{pq} = \sqrt{\frac{D}{m_s}} \cdot \sqrt{\frac{I_1 I_2 + 2I_3 I_4 + I_5 I_6}{I_2 I_6}}, \quad (2.58)$$

where

$$\begin{aligned} I_1 &= \int_0^{L_x} \frac{\partial^4 \varphi_p(x)}{\partial x^4} \varphi_p(x) dx, & I_2 &= \int_0^{L_y} (\varphi_q(y))^2 dy, & I_3 &= \int_0^{L_x} \frac{\partial^2 \varphi_p(x)}{\partial x^2} \varphi_p(x) dx, \\ I_4 &= \int_0^{L_y} \frac{\partial^2 \varphi_q(y)}{\partial y^2} \varphi_q(y) dy, & I_5 &= \int_0^{L_y} \frac{\partial^4 \varphi_q(y)}{\partial y^4} \varphi_q(y) dy, & I_6 &= \int_0^{L_x} (\varphi_p(x))^2 dx. \end{aligned} \quad (2.59)$$

Substituting Equation (2.47) into Equation (2.45) yields

$$D \nabla^4 \sum_{p=1}^{\infty} \sum_{q=1}^{\infty} \Phi_{pq}(x, y) \mu_{pq}(t) + m_s \frac{\partial^2}{\partial t^2} \sum_{p=1}^{\infty} \sum_{q=1}^{\infty} \Phi_{pq}(x, y) \mu_{pq}(t) = f(x, y, t). \quad (2.60)$$

Multiplying both sides of Equation (2.60) by the mass-normalised mode shapes $\Phi_{pq}(x, y)$ and integrating over the length and width of the plate yields

$$\begin{aligned} \sum_{p=1}^{\infty} \sum_{q=1}^{\infty} \mu_{pq}(t) \int_0^{L_x} \int_0^{L_y} D \nabla^4 \Phi_{pq}(x, y) \Phi_{jk}(x, y) dy dx + \sum_{p=1}^{\infty} \sum_{q=1}^{\infty} \frac{\partial^2}{\partial t^2} \mu_{pq}(t) \int_0^{L_x} \int_0^{L_y} \Phi_{pq}(x, y) m_s \Phi_{jk}(x, y) dy dx \\ = \int_0^{L_x} \int_0^{L_y} \Phi_{pq}(x, y) f(x, y, t) dy dx \end{aligned} \quad (2.61)$$

After applying the orthogonality conditions, assuming the external pressure $f(x, y, t) = F \delta(x - x_0) \delta(y - y_0) e^{i\omega t}$ is a time harmonic point force of frequency ω and amplitude F acting at point (x_0, y_0) , the modal displacement becomes [59]

$$\mu_{pq}(t) = \frac{\Phi_{pq}(x_0, y_0) F e^{i\omega t}}{\omega_{pq}^2 - \omega^2}. \quad (2.62)$$

Allowing the elastic modulus to be complex, i.e. $E = E(1 + i\eta_s)$, to represent the internal damping for time harmonic behaviour, where η_s is the loss factor of the plate, Equation (2.62) becomes

$$\mu_{pq}(t) = \frac{\Phi_{pq}(x_0, y_0) F e^{i\omega t}}{\omega_{pq}^2 (1 + i\eta_s) - \omega^2}. \quad (2.63)$$

Thus, from Equation(2.47), the response of the plate is given by

$$w(x, y, t) = \sum_{p=1}^{\infty} \sum_{q=1}^{\infty} \frac{\Phi_{pq}(x, y) \Phi_{pq}(x_0, y_0) F e^{i\omega t}}{\omega_{pq}^2 (1 + i\eta_s) - \omega^2}, \quad (2.64)$$

and is hence a sum of contributions from the modes of vibration. The surface velocity of the plate at point (x_n, y_n) is, in the frequency domain for time harmonic excitation, [57, 60]

$$V_n(\omega) = i\omega \sum_{p=1}^{\infty} \sum_{q=1}^{\infty} \frac{\Phi_{pq}(x_0, y_0) \Phi_{pq}(x, y) F}{\omega_{pq}^2 (1 + i\eta_s) - \omega^2}. \quad (2.65)$$

Detailed derivation of these equations can be found in [57, 60, 64-65].

2.4.2.1 Numerical simulations: Mode shapes and natural frequencies

The parameters of the clamped rectangular plate used in the numerical simulation are given in Table 2.3. The mode shapes $\Phi_{pq}(x, y)$ of the plate are shown in Figure 2.11 while the natural frequencies are tabulated in Table 2.4. There are 12 structural modes below 1 kHz, which is the upper frequency limit in the numerical simulations presented later in this thesis.

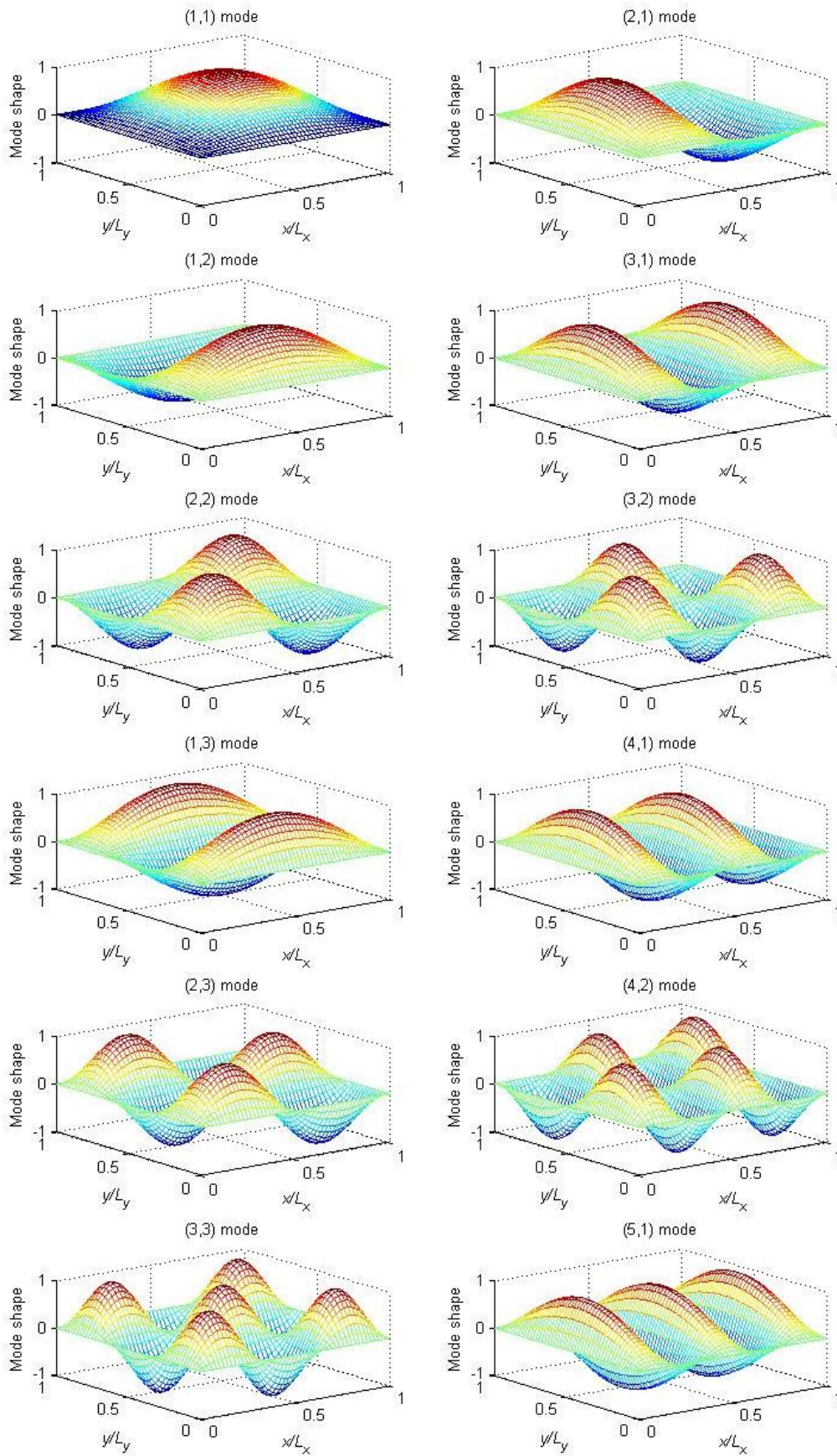


Figure 2.11: Mode shapes of the clamped plate.

Table 2.3: Parameters of clamped plate

Parameter	Value
Length L_x	0.4 m
Width L_y	0.3 m
Thickness h	0.002 m
Density ρ	7800 kg m ⁻³
Young Modulus E	200 GPa
Loss factor η_s	0.01
Poisson's ratio ν	0.3

Table.2.4: Natural frequencies of the clamped plate

Mode (p, q)	Frequency (Hz)	Mode (p, q)	Frequency (Hz)
1, 1	156.1	4, 1	675.0
2, 1	262.2	1, 3	688.6
1, 2	367.5	2, 3	784.3
3, 1	436.8	4, 2	862.6
2, 2	466.0	3, 3	942.6
3, 2	630.9	5, 1	974.9

2.4.2.2 Numerical simulations: Radiated sound power of plate radiator

Suppose the plate is excited by a point force at $(x_0, y_0) = (0.06 \text{ m}, 0.045 \text{ m})$. From Equations (2.12) and (2.13), the radiated sound power W of the plate can be calculated and is plotted in Figure 2.12. The figure also shows the individual contribution W_j of the j^{th} radiation mode.

There are 12 peaks shown in the total radiated sound power plot which correspond to the 12 natural frequencies of the plate below 1 kHz. These peaks also indicate strong radiation due to the large response at the resonance frequencies. Similar to the beam radiator case, this figure also shows that some individual ARMs are strong radiators at certain frequencies and weak radiators at other frequencies. These happen when the shapes of individual ARMs are similar to the vibration mode shapes at a particular resonance frequency.

For example, the first ARM radiates most of the power at resonance frequencies number one (mode (1, 1)), four (mode (1, 3)) and eight (mode (3, 1)), which are symmetric about the plate centreline about both the x and y axes. These three vibration modes have the highest net volume displacement and hence the velocity at the central area of the plate, while the first ARM also has a large amplitude in this area. In contrast, the first ARM radiates weakly at other vibration modes, which are antisymmetric about one or both centrelines of the plate. This issue is related to symmetry of the mode and ARM shapes. Around one resonance, one vibration mode dominates, and hence only ARMs with similar symmetry are the strong radiators. Similar statements can be made to explain the reasons behind the strong radiation by other ARMs, for instances, the second ARM radiates strongly at resonance frequencies number three (mode (1, 2)) and six (mode (3, 2)), and the third ARM at resonance frequencies number two (mode (2, 1)), seven (mode (4, 1)) and nine (mode (2, 3)).

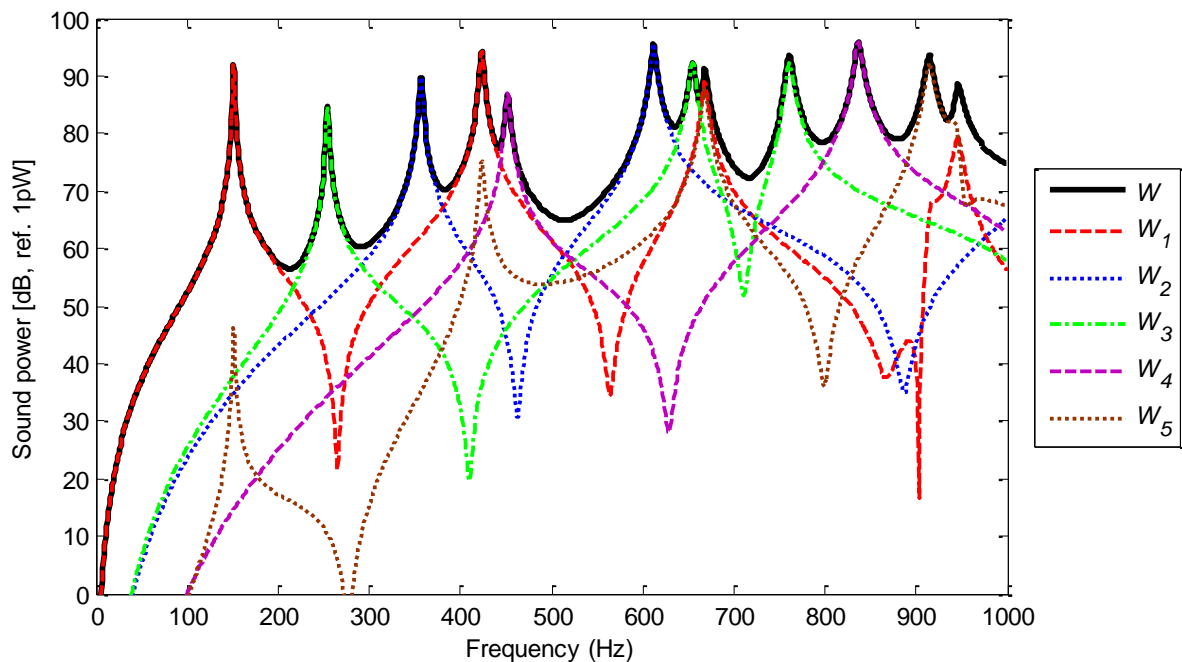


Figure 2.12: Radiated sound power of plate radiator, where W_j is the individual sound power from j^{th} ARM.

Figure 2.13 shows the ratio of the sound power contributed by the individual ARMs to the total sound power. For the lower frequency range below 210 Hz, the sound power is dominated by the first ARM. The sound power contributed by the first two ARMs is dominant up to the fifth resonance frequency (mode (2, 2)), except at the mode (2, 1), while

the first three ARMs generate most of the sound power below 800 Hz, except at the fifth resonance frequency, where ARM 4 contributes strongly. This is because they are more efficient radiators as compared to higher order ARMs. If the first five ARMs are considered, the sound power can be accurately estimated for frequencies up to 900 Hz. For this particular case, the radiated sound power of the plate for frequencies up to 1 kHz can be accurately estimated using five ARMs.

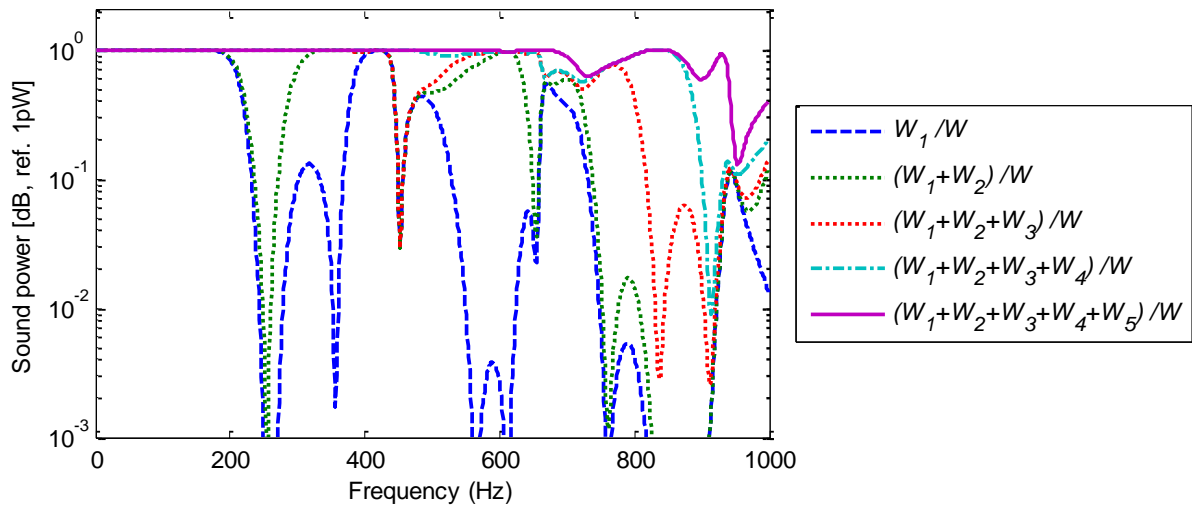


Figure 2.13: Ratio of sound powers of individual ARMs to the total sound power of plate radiator.

2.5 Summary

In summary, this chapter concerns the theoretical calculation of radiated sound power from vibrating structures. This chapter provides the theoretical basis for the time-domain estimation of radiated sound power which will be discussed in the next chapter. This chapter began by discussing the sound power radiated by vibrating structures. Expressions were developed for radiated sound power in Equation (2.4). Then the concept of acoustic radiation modes (ARMs) was described. These are found from eigenanalysis of the radiation resistance matrix in Equation (2.5), where the eigenvectors are the ARMs and their radiation efficiencies are functions of the corresponding eigenvalues. Note that the shapes of the ARMs depend only on radiator geometry and frequency. Their radiation efficiencies are also frequency dependent, where the lower ARMs are seen to be more efficient radiators than the higher ARMs especially at low frequencies.

Next, the dynamics of a simply supported beam and a clamped rectangular plate, which are used to illustrate the 1-D and 2-D radiators, were described. Finally, numerical examples of the sound power radiated from vibrating beam and plate were presented. It is found that there is a strong radiation when the vibration mode and ARM shapes are both symmetric or both anti-symmetric, and weak radiation when otherwise.

The next chapter concerns time-domain estimation of ARM amplitudes and radiated sound power. These are then used in Chapter 4 in an active noise control system aimed at controlling the ARMs, which are the most significant radiators. Experimental verification of estimation and active control of radiated sound power based on time domain ARM estimates is then carried out and presented in Chapter 5.

CHAPTER 3 : TIME-DOMAIN ESTIMATION OF ACOUSTIC RADIATION MODE AMPLITUDES

3.1 Introduction

This chapter describes the method for estimating the ARM amplitudes and hence radiated sound power in real time, which is implemented in discrete time. The chapter begins with the development of Finite Impulse Response (FIR) filters for real-time estimation of ARM amplitudes and sound power. These are estimated from measurements of the response at a number of points on the structure. Causality is seen to be an issue for real-time implementation. Various forms of filters are discussed. To verify the performance of the estimation method, numerical simulations are presented. These include the performance of the proposed filters in estimating the ARMs and the structural response of the radiator, as well as comparison between theoretical and estimated radiated sound power.

3.2 Acoustic radiation modes estimated using FIR filters

As described in Section 2.3, the ARM shapes are frequency-dependent, thus the ARM amplitude vector, $\mathbf{y}(\omega)$, can be written in the frequency domain as

$$\mathbf{y}(\omega) = \mathbf{Q}(\omega)^T \mathbf{v}(\omega), \quad (3.1)$$

where $\mathbf{Q}(\omega)$ is the ARM matrix and $\mathbf{v}(\omega)$ is the velocity vector. Note that Equation (3.1) is meant for a continuous structure. In a practical application, the surface of the radiator is discretised into many elemental radiators. The discretisation is based on the zero-order elements strategy found in the Boundary Element Method (BEM). This technique requires single node per element and each element is assumed to be monopole [53, 66].

Now suppose that these ARM estimates are given by measuring the response of the structure at a relatively small number of discrete points on the radiating surface and then

weighting and summing these point measurements. Suppose N_s structural sensors are used to estimate the ARMs. Hence the ARM amplitudes in Equation (3.1) are approximated by

$$\begin{bmatrix} Y_1(\omega) \\ \vdots \\ Y_r(\omega) \\ \vdots \\ Y_R(\omega) \end{bmatrix} \approx \begin{bmatrix} Q_{1,1}(\omega) & \cdots & Q_{1,n}(\omega) & \cdots & Q_{1,N_s}(\omega) \\ \vdots & \ddots & & & \vdots \\ Q_{r,1}(\omega) & & \ddots & & Q_{r,N_s}(\omega) \\ \vdots & & & \ddots & \vdots \\ Q_{R,1}(\omega) & \cdots & Q_{R,n}(\omega) & \cdots & Q_{R,N_s}(\omega) \end{bmatrix} \begin{bmatrix} V_1(\omega) \\ \vdots \\ V_n(\omega) \\ \vdots \\ V_{N_s}(\omega) \end{bmatrix}, \quad (3.2)$$

where $V_n(\omega)$ is the velocity at the n^{th} sensor location and $Q_{r,n}(\omega)$ is the value of the r^{th} ARM at the n^{th} sensor location. In effect this means that a (small) number of point response measurements are taken and then filtered by $Q_{r,n}(\omega)$ and summed to provide an estimate (in the frequency domain) of the ARM amplitude $Y_r(\omega)$,

$$Y_r(\omega) \approx \sum_{n=1}^{N_s} Q_{r,n}(\omega) V_n(\omega). \quad (3.3)$$

3.3 Practical implementation of ARM FIR filters

The multiplication in the frequency domain becomes a convolution in the time domain. The ARM amplitude, $y_r(t)$ can be approximated in real-time by passing the measured velocity signals through the array of ARM FIR filters [67]

$$y_r(t) \approx \sum_{n=1}^{N_s} q_{r,n}(t) * v_n(t), \quad (3.4)$$

where $q_{r,n}(t)$ and $v_n(t)$ are the inverse Fourier transforms of $Q_{r,n}(\omega)$ and $V_n(\omega)$, respectively, and $*$ denotes a convolution. This implies the ARM amplitude can be calculated by applying a filter whose frequency response is $Q_{r,n}(\omega)$ and whose impulse response is $q_{r,n}(t)$ to the sensor velocities $v_n(t)$, and then summing the outputs from each of these point sensor measurements together. The configuration of ARM filters used to measure the real-time ARM amplitude $y_r(t)$ from an array of sensor velocities is illustrated in Figure 3.1.

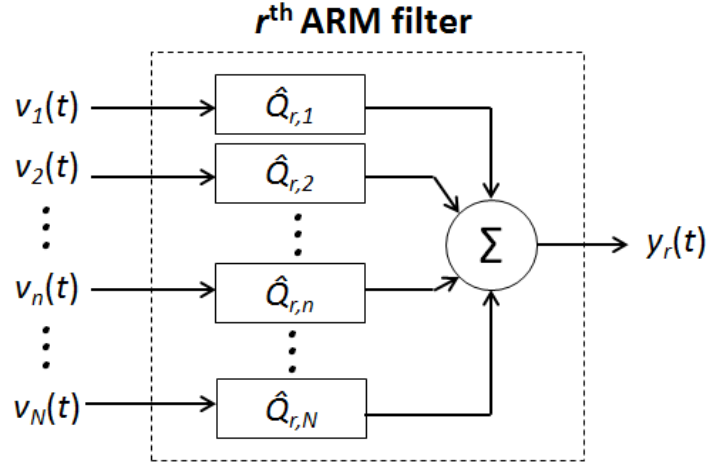


Figure 3.1: Real-time r^{th} ARM filter.

In discrete-time applications, the ARMs can be estimated at discrete times $t=m\tau$, where τ is the sampling period and $f_s=1/\tau$ is the sampling frequency, and m is the sample index. Hence, Equation (3.4) becomes

$$y_r(m) \approx \sum_{n=1}^{N_s} \left\{ \sum_{s=-\infty}^{+\infty} q_{r,n}(s) v_n(m-s) \right\}, \quad (3.5)$$

where $y_r(m)$ and $q_{r,n}(m)$ are the estimate of the r^{th} ARM amplitude and sampled value of $q_{r,n}(t)$, respectively.

Due to finite approximation using an FIR filter, in a practical implementation the infinite sum has to be truncated. Given that $Q_{r,n}(\omega)$ always has zero phase, the best approximation will have $q_{r,n} = q_{r,-n}$, but this implies the FIR filter will be non-causal. However, a non-causal filter is not practical due to the fact that future values of $v_n(m-s)$ (with $s < 0$) are not known in real-time. For real time implementation, the filter must be causal, i.e. $q_{r,n}(s) = 0$ for all $s < 0$, so that the sum over s in Equation (3.5) can only run from 0 to $+\infty$. These restrictions lead to the approximated, causal ARM amplitude estimate

$$y_r(m) \approx \sum_{n=1}^{N_s} \left\{ \sum_{s=0}^S q_{r,n}(s) v_n(m-s) \right\}. \quad (3.6)$$

The causal FIR filter in Equation (3.6) will never be better than a non-causal filter that uses future values of v_n , i.e. for $s < 0$, because causality adds a constraint to the approximation. Figure 3.2 illustrates the differences between causal and non-causal FIR filters of 7-th order which approximate the same zero-phase frequency response. In this figure, the coefficients of the non-causal FIR filter are symmetric about $m=0$, suggesting a good approximation of the impulse response occurs at $m=0$. However, the causal FIR filter is only able to approximate half of the impulse response. Note also that the non-causal filter has zero phase but the causal filter does not.

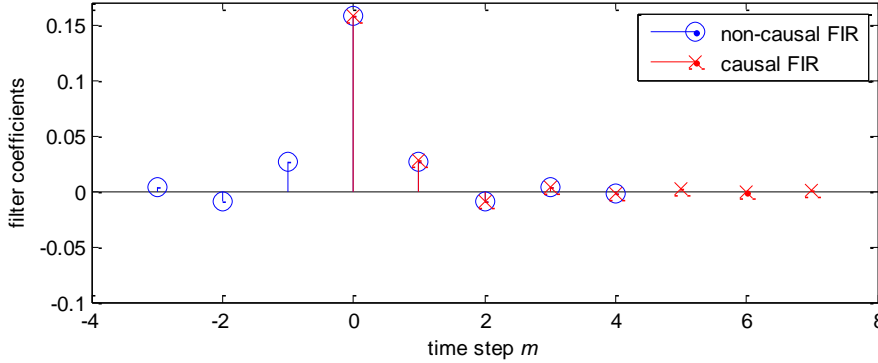


Figure 3.2: Coefficients of non-causal and causal FIR filters for $q_{1,n}$, $q_{2,n}$ and $q_{3,n}$ for ARMs 1, 2 and 3 as functions of time sample index m , for $d=7$.

To make a causal, practically realisable filter for real-time implementation that provides a good approximation to the non-causal filter, a causal version of the filter is introduced by delaying the non-causal filter by d samples [68]. This new filter will be called the *causal delayed filter* throughout this thesis. This filter approximates a frequency response $Q_{r,n}(\omega)\exp(-i\omega d/f_s)$ and produces an approximation of $y_r(m)$ at time sample $m+d$. The phase is linear with a time delay of d steps. It uses $(2d + 1)$ coefficients for the optimal estimation of $Q_{r,n}(\omega)$ in the least square sense, i.e.

$$y_r(m) \approx \sum_{n=1}^{N_s} \left\{ \sum_{s=0}^{2d} q_{r,n}(s) v_n(m-s-d) \right\}. \quad (3.7)$$

As an illustration, the FIR filter coefficients for the first three ARM shapes for the rectangular plate ($L_y / L_x = 0.75$) at point $(0.1L_x, 0.3L_y)$ are shown in Figure 3.3. In this figure, both the causal FIR filter from Equation (3.6) and causal-delayed FIR filter from Equation (3.7) are 15th order filters. Here, 7 samples delay are implemented in the causal-delayed FIR filters (i.e. $d=7$). These filters are symmetric, that is $q_{r,n}(s) = q_{r,n}(2d - s)$.

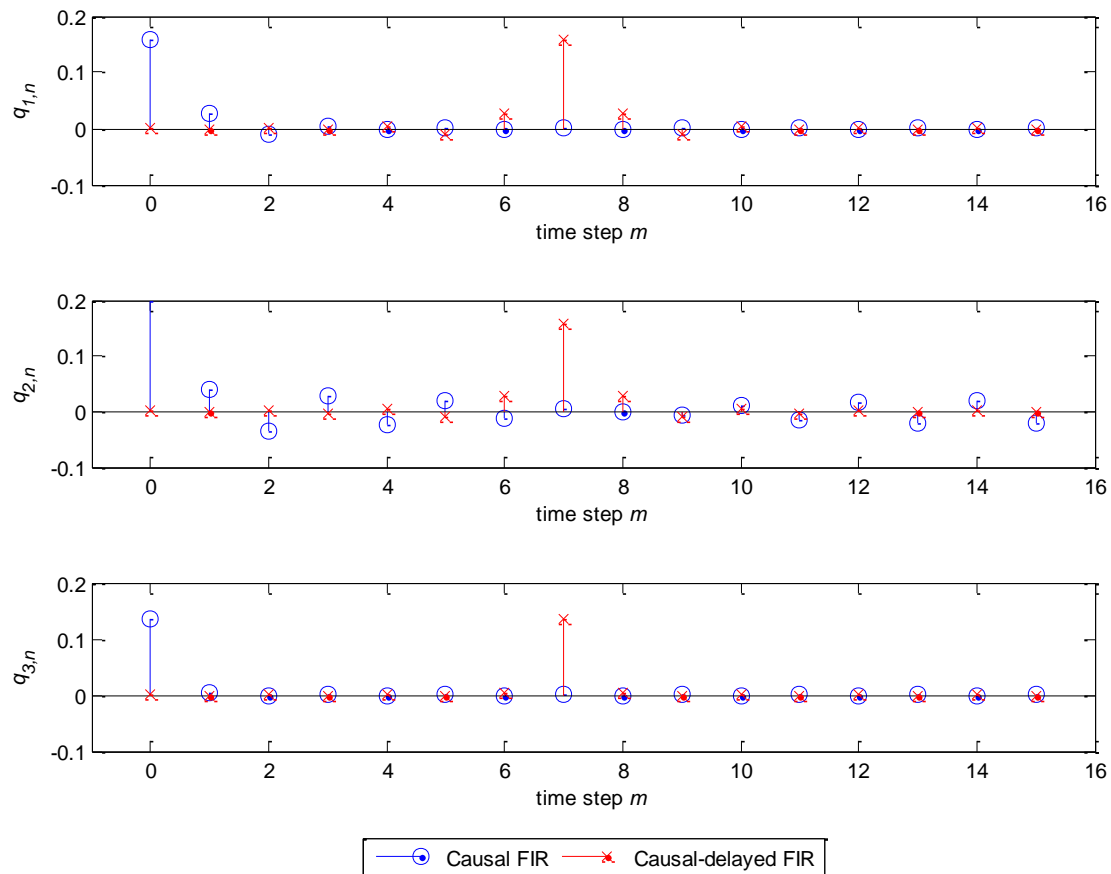


Figure 3.3: Coefficients of FIR filters for $q_{1,n}$, $q_{2,n}$ and $q_{3,n}$ for ARMs 1, 2 and 3 as functions of time step m , for $d=7$, measured at point $(0.1L_x, 0.3L_y)$.

For certain applications, such as in estimating the radiated sound power or using the ARM amplitude as an error function in adaptation schemes, allowing d samples delay to derive an ARM estimate will not be important. The output of the filter then provides an estimate at time step m of the ARM amplitude (or radiated sound power) at the time $m-d$, i.e. d time steps earlier.

3.4 Filter quality

This section briefly discusses the quality of the ARM estimates of the filters using finite number of discrete sensors. In general, n sensors are required to estimate n ARMs exactly. The sensor outputs are passed to a set of ARM filters to estimate the ARM amplitude. The weights of these ARM filters depend on the sensor locations on the radiator. The sensor outputs are of course affected by motion in the other ARMs. Thus the filter estimates are also affected by the presence of other ARMs, and this is called as observation spillover. The locations of the sensors affect the amount of spillover, hence the location of the sensors can be selected to minimise the sensitivity to certain ARMs. The same thing occurs for control using a number of point actuators. The location of point actuators must be selected carefully in order to excite a specific ARM and also to avoid control spillover occurs.

3.5 Structural response estimation using IIR filters

For real-time simulation purposes, the structural response must be estimated in real-time. The clamped plate is selected as the reference model to illustrate the approach used to estimate the structural response in real time, although it is also applicable to the one-dimensional radiator. Re-arranging Equation (2.64), the structural FRF in terms of a sum of modal contributions is given by

$$H(x, y) = i\omega \sum_{q=0}^{\infty} \sum_{p=0}^{\infty} \left(\omega_{pq}^2 (1 + i\eta) - \omega^2 \right)^{-1} \varphi_{pq}(x_0, y_0) \cdot \varphi_{pq}(x, y). \quad (3.8)$$

These transfer functions have many resonance peaks. Thus, it is not practical to estimate the response using FIR filters due to the very large number of filter coefficients required for the FIR filter to give an accurate estimate. Instead, infinite impulse response (IIR) filters are more suitable for this case. However, care must be taken to ensure the IIR filters are stable. To ensure the filter's stability, each resonant modal response is approximated by an IIR filter, and these modal IIR filters are summed to give the total response of the structure.

A general IIR filter is defined as

$$y(m) = \sum_{k=1}^K a_k \cdot y(m-k) + \sum_{j=0}^{J-1} b_j \cdot x(m-j), \quad (3.9)$$

where $y(m)$ and $x(m)$ are the output and input of the filter at time m , respectively, and there are K 'feedback' coefficients a_k and J 'feedforward' coefficients b_j . The z -transform of Equation (3.9) can be written in the form of the transfer function [69]

$$H(z) = \frac{Y(z)}{X(z)} = \frac{B(z)}{A(z)}, \quad (3.10)$$

where

$$A(z) = 1 - a_1 z^{-1} \dots - a_K z^{-K}, \quad (3.11)$$

$$B(z) = b_0 + b_1 z^{-1} \dots + b_{J-1} z^{-J+1}. \quad (3.12)$$

Assuming N_β resonance frequencies in the frequency range of interest, the velocity response at the n^{th} sensor can be approximated in the time domain by

$$v_n(t) \approx \sum_{\beta=1}^{N_\beta} \varphi_{\beta,n} \varphi_{\beta,0} \cdot h_\beta(t) * f(t), \quad (3.13)$$

where $*$ denotes a convolution, $\varphi_{\beta,n}$ is the mode shape of mode β at location (x_n, y_n) , $\varphi_{\beta,0}$ is the mode shape of mode β at the excitation point (x_0, y_0) and $f(t)$ is a point force at the excitation point. $h_\beta(t)$ is the impulse response of mode β and its frequency response is

$$H_\beta(\omega) = \frac{i\omega}{\omega_\beta^2 (1 + i\eta) - \omega^2}. \quad (3.14)$$

In the discrete time domain, the velocity at location (x_n, y_n) contributed by mode β can be estimated using IIR filters [69]

$$v_n^{(\beta)}(m) = \varphi_{\beta,n} \varphi_{\beta,0} \cdot \left(\sum_{s_b=1}^{n_b} b_s^{(\beta)} \cdot f(m-s_b) + \sum_{s_a=0}^{n_a-1} a_s^{(\beta)} \cdot v_n(m-s_a) \right), \quad (3.15)$$

where $b_s^{(\beta)}$ ($s_b = 0, 1, \dots, n_b^{(\beta)}$), and $a_s^{(\beta)}$ ($s_a = 0, 1, \dots, n_a^{(\beta)}$), are the coefficients of the numerator and denominator of $H_\beta(\omega)$, respectively. The z-transform of the Equation (3.15) is

$$H_\beta(z) = \frac{b_0 + b_1 z^{-1} \dots + b_{n_b-1} z^{-n_b+1}}{1 - a_1 z^{-1} \dots - a_{n_a} z^{-n_a}}. \quad (3.16)$$

These IIR filters, as illustrated in Figure 3.4, are used to estimate the response in each resonant mode and will be called *resonant filters* throughout the thesis.

The real time velocity at a particular position on the radiator is then obtained by multiplying the output of the resonant filters with the array of shape function constants. The velocity of the radiating structure at point (x_n, y_n) is the sum of all modes

$$v_n(m) \approx \sum_{\beta=1}^{N_\beta} \varphi_{\beta,n} \varphi_{\beta,0} \cdot \left(\sum_{s_b=1}^{n_b} b_s^{(\beta)} \cdot f(m-s_b) + \sum_{s_a=0}^{n_a-1} a_s^{(\beta)} \cdot v_n(m-s_a) \right). \quad (3.17)$$

Figure 3.5 shows the configuration of the resonant filters and the arrays of shape functions used to estimate structural surface velocities of the radiator in real time. This is later implemented in Simulink for real-time simulations. Each resonant modal response given in Equation (3.15) can be approximated sufficiently by a 3rd order IIR filter, where the coefficients are calculated using Matlab function *invfreqz*.

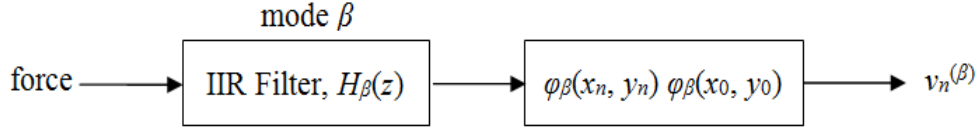


Figure 3.4: Resonant filter of mode β , $H_\beta(z)$.

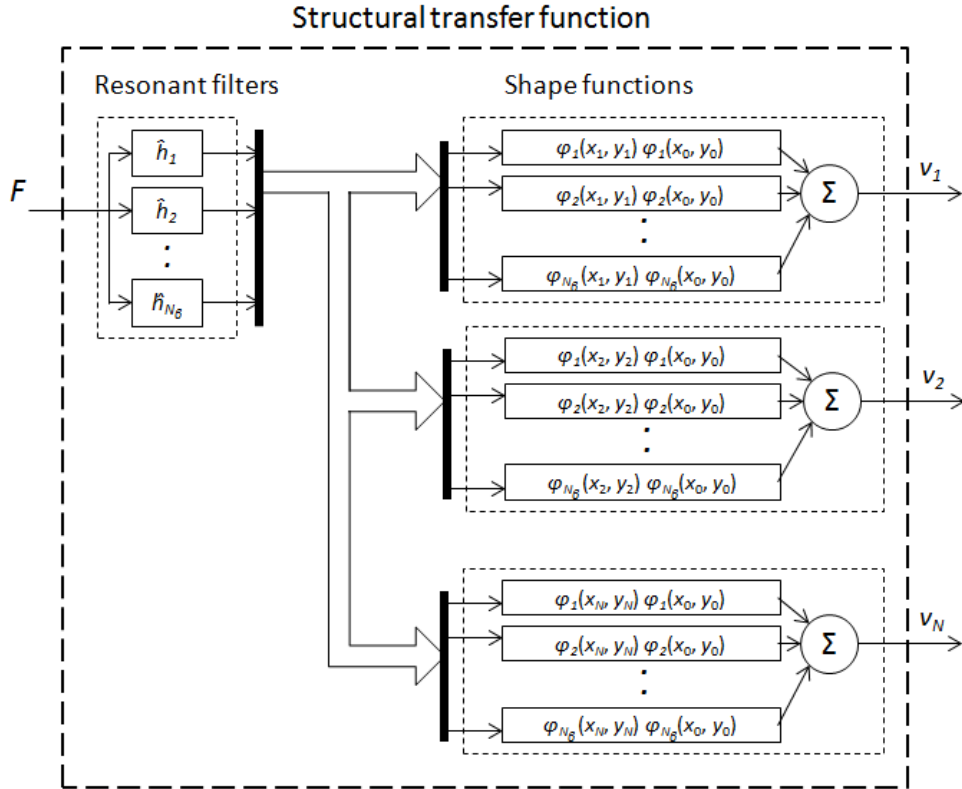


Figure 3.5: Configuration of resonant filters to simulate the real-time structural surface velocities.

3.6 Estimation of radiated sound power

This section describes the method used in this thesis to estimate the sound power based on the ARM estimates developed in the previous section. The estimates of the ARM amplitudes are found by filtering the time series of the surface velocities measured by sensors at points on the radiator with the array of causal-delayed ARM filters, before summing them. Note that each ARM amplitude requires a number N_s of ARM filters. As mentioned in Chapter 2,

information on the shapes of the ARMs and vibration modes within a particular frequency range provide a general guess of the optimal locations for the structural sensors. However, optimisation of the sensor locations will not be covered in this thesis. Instead, for simplicity, an equally spaced array of sensors will be used in the rest of this thesis.

Figure 3.6 shows the block diagram of the method to estimate the radiated sound power. Here, the number of sensors required must be equal to or greater than the number of ARMs of the radiating structure within the frequency range of interest that it is desired to estimate. The measured surface velocities are filtered and summed to estimate the ARM amplitude y_j . The radiated sound power is estimated by calculating the product of the square of these amplitudes with the corresponding eigenvalues. To compare real-time estimates with the actual radiated sound power, the power was also estimated in the frequency domain. In the simulations below, short-time Fourier transform was applied to the time series of ARM amplitudes y_j using 512-points Hann-window with 50% frame-overlap which created 30 frames. Zero-padding (1536-points zeros) was applied for interpolating the power spectrum. Then the frequency-domain estimate of the ARM amplitude was obtained by finding the average of the power spectrum across frames of these time series.

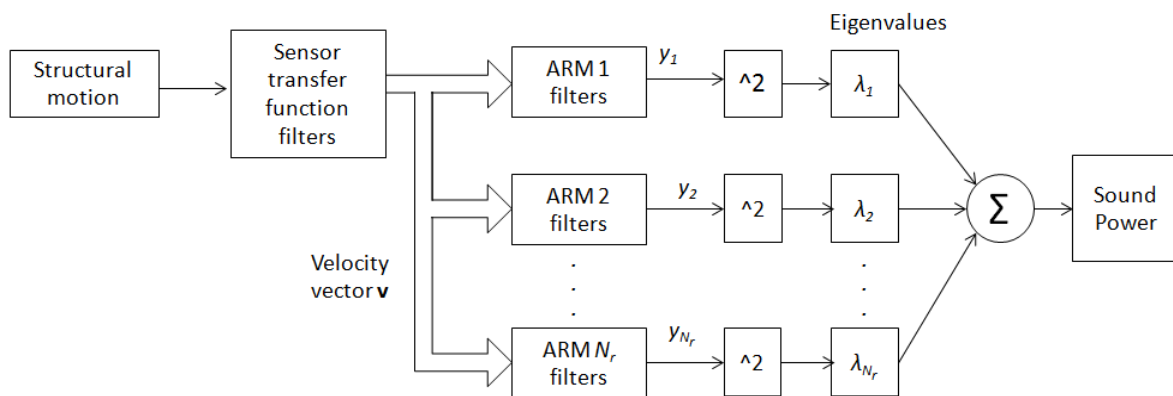


Figure 3.6: Block diagram representation of the time domain radiated sound power estimation.

3.7 Numerical simulations

This section begins with numerical examples of the performance of the ARM filters and structural transfer function filters in approximating the theoretical ARM shapes and structural

responses, respectively. The methods are illustrated using a baffled rectangular plate as the radiating structure, although the methods are also applicable to a one-dimensional radiator. A total of N_s structural sensors, equally spaced, are used to measure the surface velocities of the radiator. Finally simulations on estimating the radiated sound power with reference to one and two-dimensional radiators are performed. The parameters of the beam and plate radiators are given in Table 2.1 and Table 2.3, respectively.

3.7.1 Performance of acoustic radiation mode filters

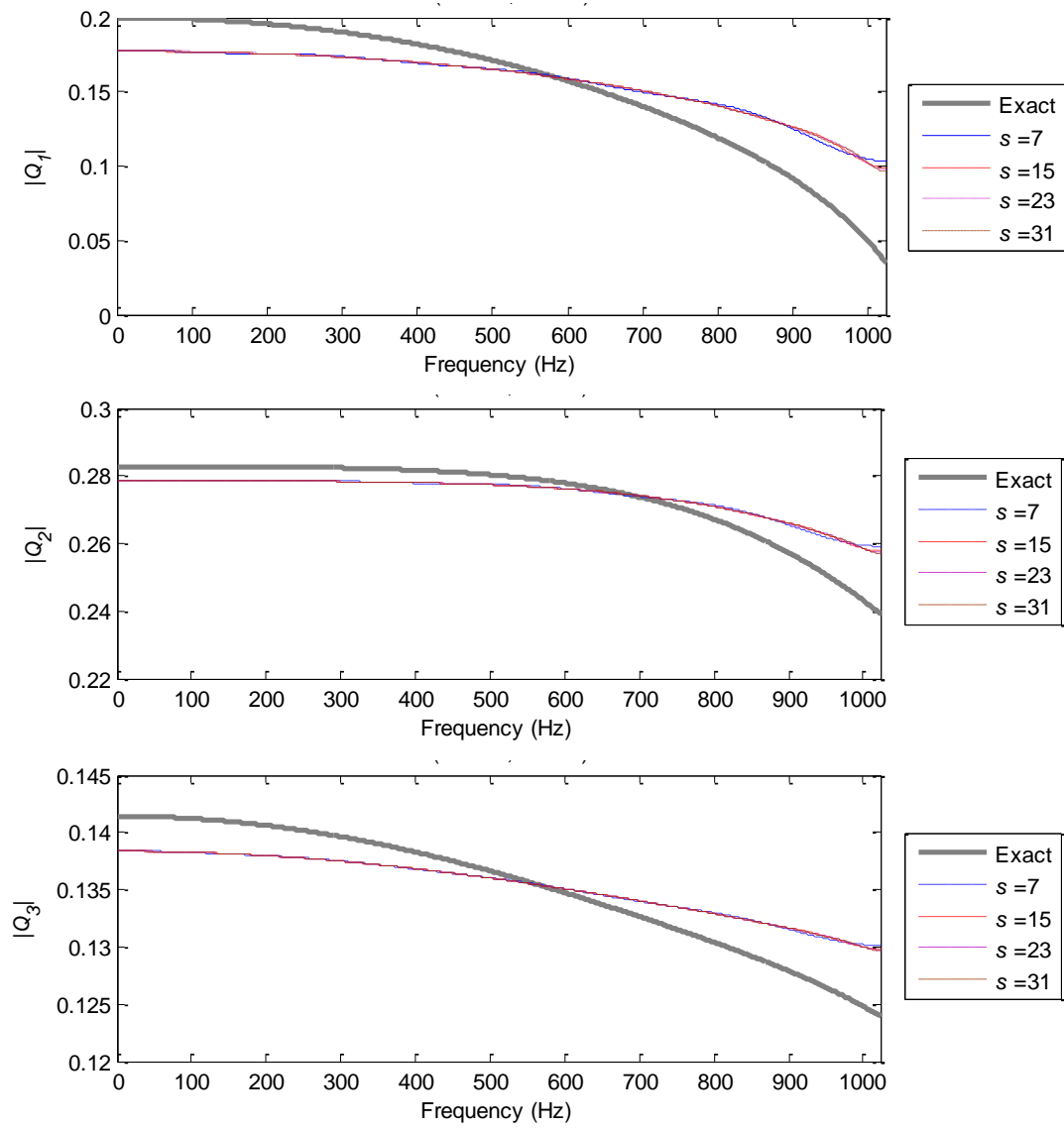
The implementation of ARM filters $\mathcal{Q}_{r,n}(\omega)$ to approximate the theoretical ARM amplitude is illustrated with reference to a baffled plate model with parameters given in Table 2.3. These FIR filters are designed by a weighted least-squares fit to the ideal frequency responses at 1000 uniformly spaced frequencies from 0 Hz to the Nyquist frequency f_n , i.e. 1 kHz with rectangular-windowed weighting from $0.1f_n$ to $0.9f_n$. Here, the Matlab function *invfreqz* is used to calculate the filter coefficients of the FIR filters and the frequency response of the implemented filter is calculated using the function *freqz*. The performance of the ARM filter is measured in term of mean square error

$$\text{MSE} = \frac{\sum_{f_i}^{f_f} (|\mathcal{Q}_{r,n}(f)| - |\hat{\mathcal{Q}}_{r,n}(f)|)^2}{f_h - f_l}, \quad (3.18)$$

where f_l and f_h are the low and high cut-off frequencies whose values are chosen to be $0.1f_n$ and $0.9f_n$, respectively. In practice the low and high frequency components of the signals will often be filtered out, for example by anti-aliasing filters and by AC coupling, and this will substantially reduce the effects of the poor approximation in these frequency ranges.

Examples of the magnitudes of the frequency response of the ARM filters approximated using causal FIR filters, are plotted in Figure 3.7(a) for various order of filter coefficients s . Based on this figure, the causal FIR filters provide accurate estimates in the middle region of the frequency range but not in the lower and upper frequency ranges. Figure 3.7 (b) shows the mean square error as a function number of filter order for the first six ARM

filters. Increasing the filter order does not improve the estimation significantly as the mean squares errors of all six ARM filters are greater than 10^{-3} . This is because, as mentioned earlier, the causal FIR filter is only able to approximate half of the impulse response of ARM, i.e. that for which $t \geq 0$.



(a)

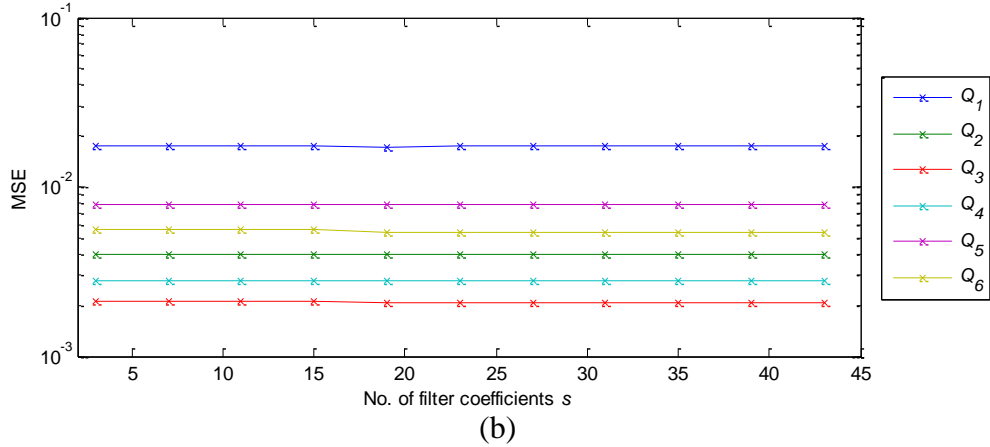


Figure 3.7: (a) Magnitude of the frequency response of the ARM filters for the first three ARMs using causal FIR filters and (b) mean square error as a function of number of filter coefficient s .

Next, the ARM filters are estimated using causal-delayed FIR filters and their performance is illustrated in Figure 3.8. As mentioned earlier, the estimation of ARMs can be further improved by implementing the causal-delayed FIR filters. Looking at Figure 3.8(a), it can be seen that the magnitude is estimated much more accurately using the causal-delayed FIR filter. Moreover, Figure 3.8(b) shows the mean square error as a function filter order for the first six ARM filters approximated using causal-delayed FIR filters. In this figure, the mean square errors decrease with the increase in the number of filter coefficients. There is therefore a trade-off between accuracy of ARM filters (i.e. improved by larger d) and controller delay (improved by decreasing d). Here, the mean square errors are below 10^{-3} for the first three ARM filters when the filter length is 23 (i.e. when $d = 11$). Hence, a 22th order causal-delayed FIR filters will be used as the ARM filters throughout the rest of the thesis.

Comparison of the phases between the theoretical and estimated ARMs is shown in Figure 3.9. It is worth emphasising that the phases of the causal-delayed ARM filters are exact, since the coefficients are symmetric about the filter centre and the phase is linear due to the time delay. Stability is also guaranteed due to the nature of FIR filters.

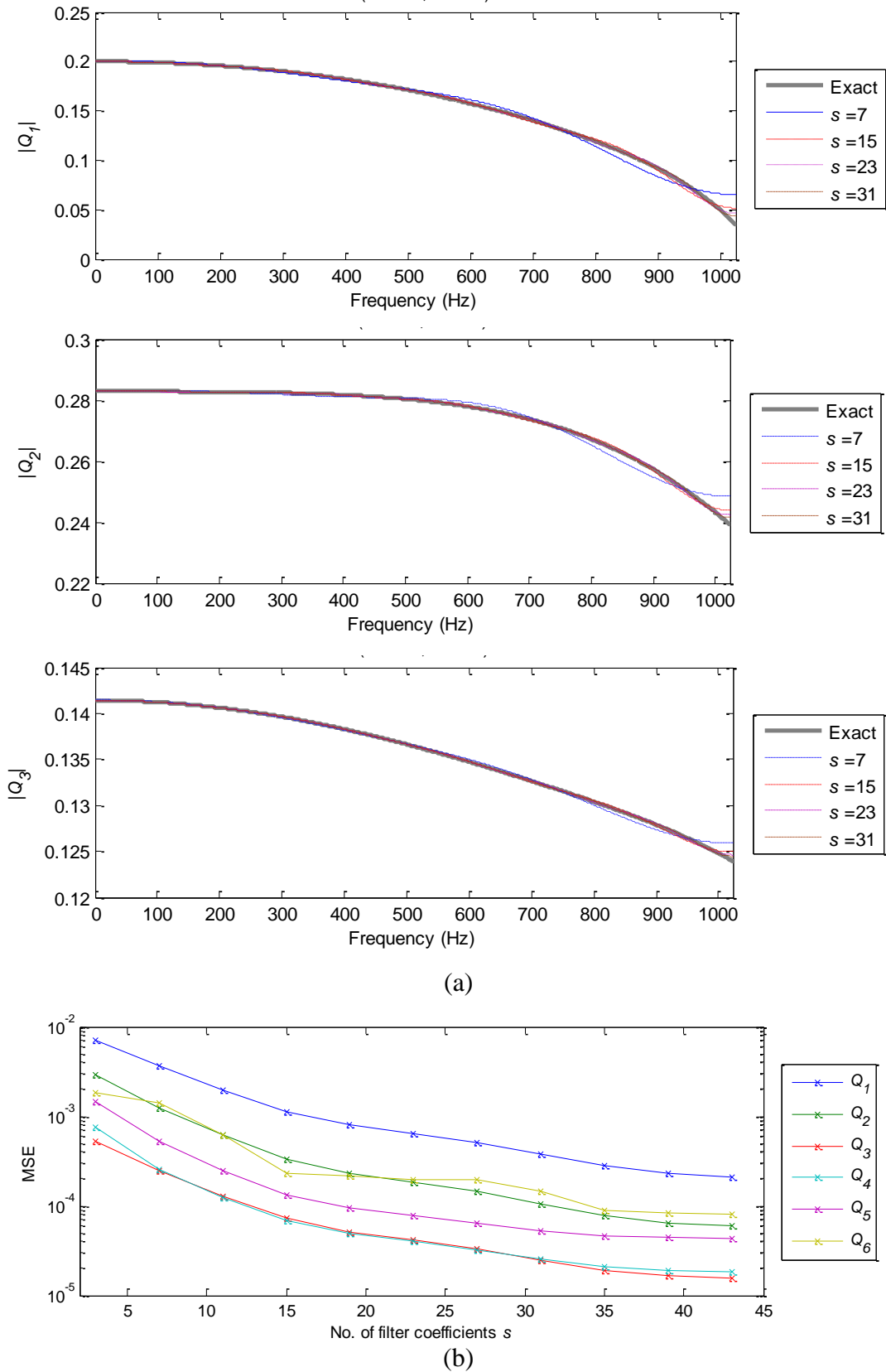


Figure 3.8: (a) Magnitude of the frequency response of the ARM filters for the first three ARMs using causal-delayed FIR filters and (b) mean square error as a function of number of filter coefficient s (where $s=2d+1$).

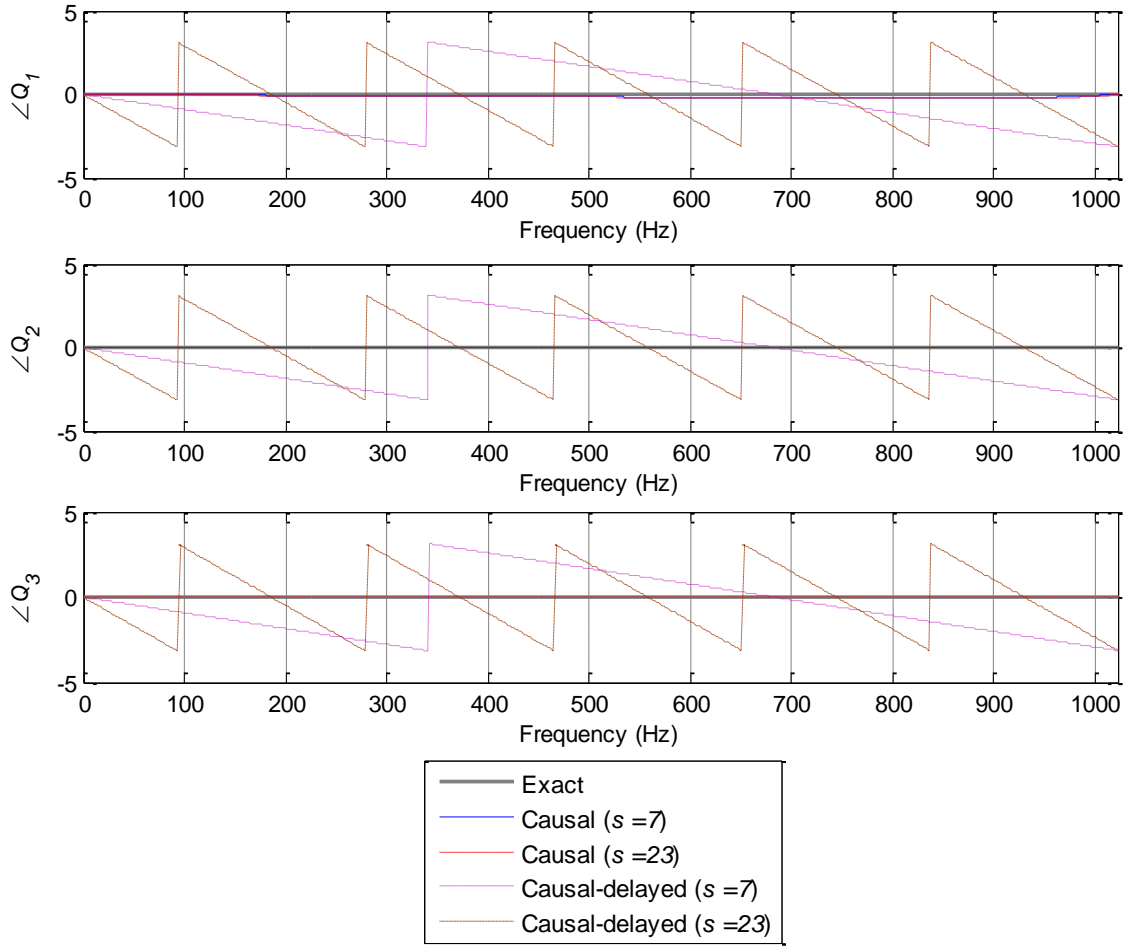


Figure 3.9: Phases comparison of the theoretical and estimated first 3 ARM frequency responses using causal and causal-delayed FIR filters, measured at $(0.1L_x, 0.3L_y)$.

3.7.2 Structural transfer function filters

Each resonant mode is modelled by an IIR filter using the Matlab function *invfreqz* and the frequency response of the implemented filter is calculated using the function *freqz*. Figure 3.10 shows the performance of the IIR filters in approximating the frequency response of the plate at $(0.3L_x, 0.1L_y)$ for the first three structural modes, when the force is applied at $(0.15L_x, 0.15L_y)$. In this figure, the frequency responses are well approximated for both magnitude and phase within the range $0.1f_n$ to $0.9f_n$. Note that the frequencies below or above this range are not important and will often be filtered out. These resonant filters are also stable. Based on the z-plane diagrams in Figure 3.11, all poles are inside the unit circle for each structural

mode which confirms their stability. In numerical simulations, the estimated velocity frequency response is obtained by performing a fast Fourier transform on the time-domain velocity signals. It is found that the magnitude of the estimated frequency response agrees with the theoretical value within the range $0.1f_n$ to $0.9f_n$, as illustrated in Figure 3.12.

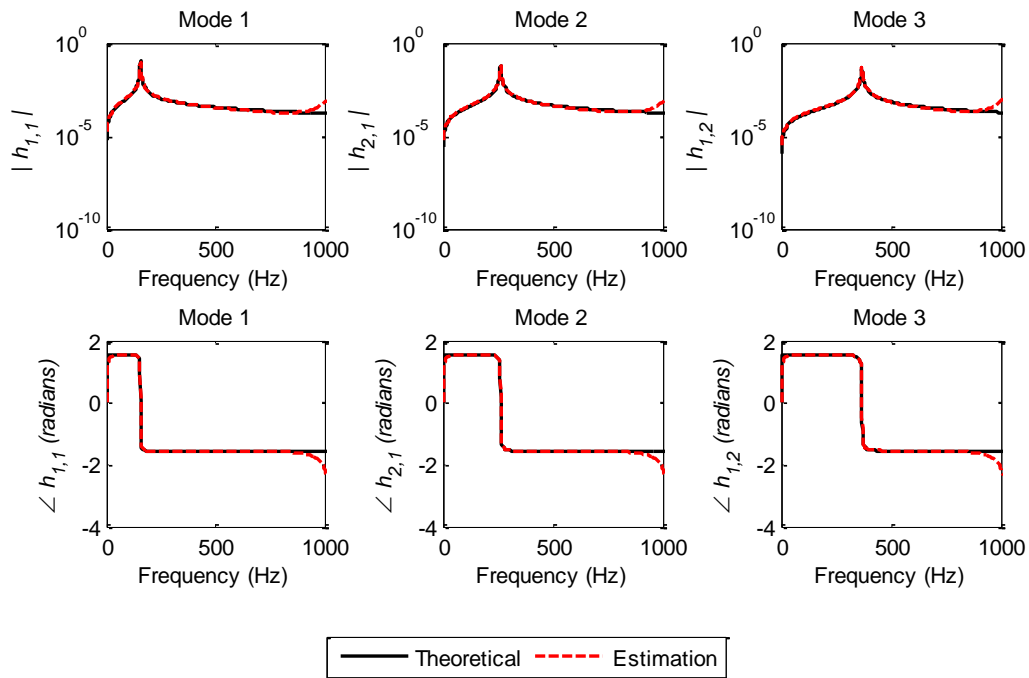


Figure 3.10: Magnitudes and phases of the theoretical and estimated modal frequency responses for the first three modes.

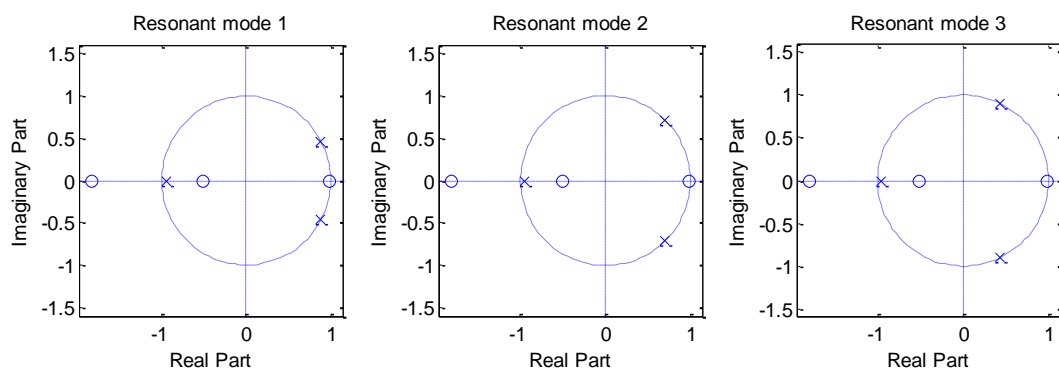


Figure 3.11: z-plane pole-zero plots of the estimated resonant filters $\hat{h}_{m,n}$ for each resonant mode, where 'o' is zero and 'x' is pole.

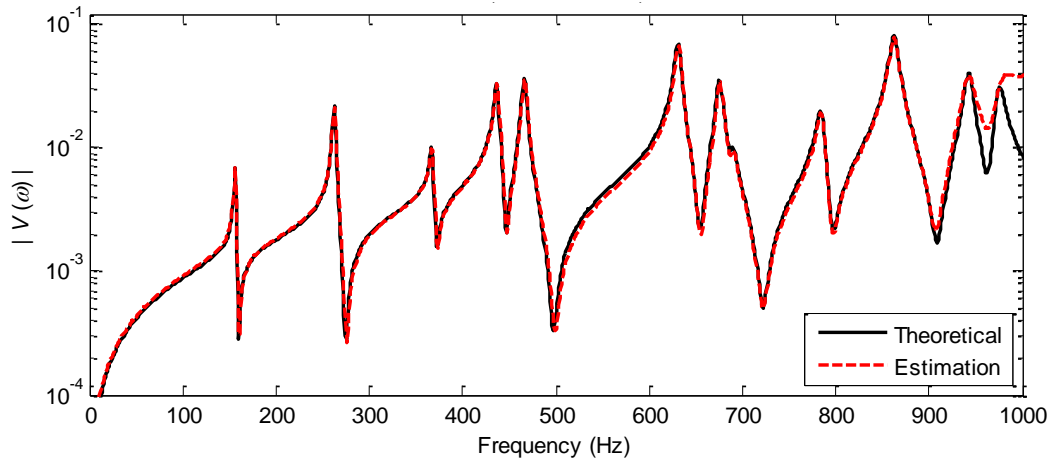


Figure 3.12: (a) Magnitude and (b) phase of the velocity frequency response at $(0.3L_x, 0.1L_y)$.

3.7.3 Estimation of radiated sound power

In this section, real time simulations of the estimation of radiated sound power for one and two-dimensional radiators using Matlab and Simulink are presented.

3.7.3.1 Baffled beam

The method is illustrated with reference to a baffled, simply supported beam with parameters given in Table 2.1. The simulation is run for 10 seconds with sampling frequency $f_s = 1024$ Hz, long enough for the frequency range and resolution shown. For these parameters, there are 3 vibration modes and 2 acoustic radiation modes with efficiencies greater than 0.1 in the frequency range $0.1f_n$ to $0.9f_n$. Therefore 3 resonant filters and 2 ARM filters are used in the estimation of the radiated sound power. The ARM filters are constructed in the time domain using 23rd order FIR filters with 11-step delay. These FIR filters are designed by a weighted least-squares fit to the ideal frequency responses at 512 uniformly spaced frequencies between 0 Hz and the Nyquist frequency, i.e. 512 Hz, with rectangular window weighting between $0.1f_n$ to $0.9f_n$.

The primary source is a random point force, $F_p(t)$ (band-pass filtered using a 5th order elliptical filter with normalised edge frequencies of $0.1f_n$ and $0.9f_n$, 0.5 dB passband ripple

and 20 dB stopband attenuation) acting on the beam at $x_0/l = 0.15$. The number of sensors used must be equal or greater than the number of ARMs. Because there are 3 radiation modes involved here, a total of at least 3 sensors are required. The sensors are located at the centre of every one-third length of the beam, i.e. at $x/L = 1/6, 1/2$ and $5/6$. These make the distance between the radiator's edges and the closest sensors from the edges, and the distance between each sensor be $l/6$ and $l/3$, respectively. The sensors and point force locations are shown in Figure 3.13.

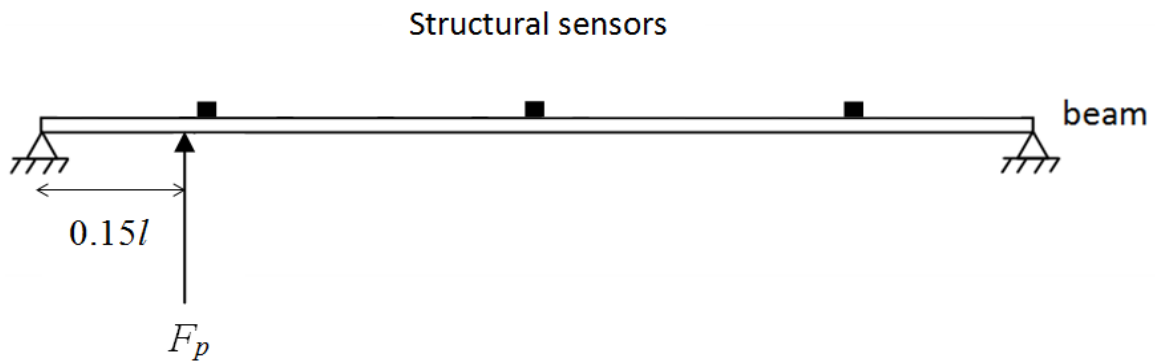


Figure 3.13: Sensor and point force arrangements on the simply supported beam.

Figure 3.14 shows the radiated sound power obtained using the theoretical and time-domain estimation methods. There are 3 significant peaks corresponding to 3 natural frequencies at 37 Hz, 147 Hz and 331 Hz, suggesting strong radiation occurs at the resonance frequencies. Here, only the first two ARM filters were used in the computation. This is because for this frequency range, only the first two ARMs are important (i.e. radiation efficiency more than 0.1) in radiating the sound power. It is seen that the radiated sound power estimated from the time-domain ARM method using only two ARM filters, is in good agreement with the theoretical value, except above $0.9f_n$ where the signals are filtered out. Figure 3.15 shows the theoretical and estimated sound power radiated by the first and second ARMs. Again, it can be seen the individual sound powers are approximated well using the time-domain ARM estimation method.

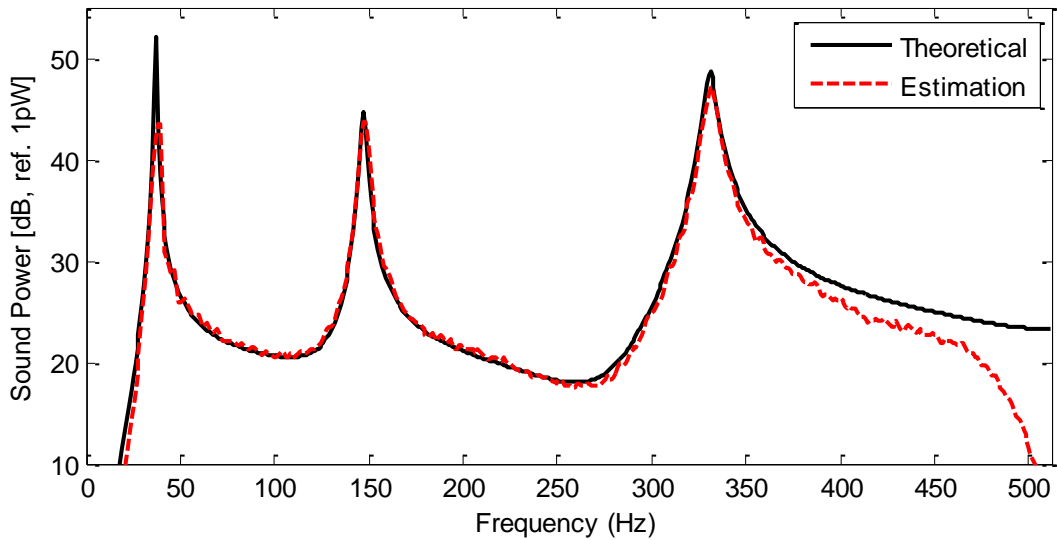


Figure 3.14: The sound power radiated from beam with primary force located at $x_0/l = 0.15$, estimated by ARM filters.

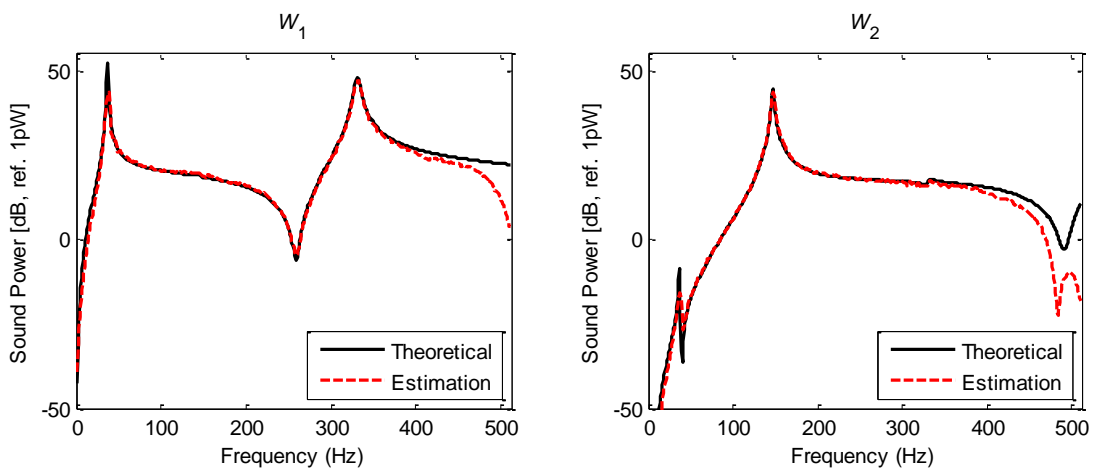


Figure 3.15: The individual sound powers radiated from beam with primary force located at $x_0/l = 0.15$, estimated by the first two ARM filters.

3.7.3.2 Baffled plate

For the case of a two-dimensional radiator, a baffled rectangular steel plate clamped at all edges with parameters given in Table 2.3 is used as a model. The simulation is performed with a sampling frequency f_s of 2 kHz for 10 seconds. For these parameters, there are 12 vibration modes and 8 acoustic radiation modes with efficiency more than 0.1 in the

frequency range $0.1f_n$ to $0.9f_n$. Thus, 12 resonant filters and 8 ARM filters are used in the computation.

The causal-delayed ARM filters used here are constructed in the time domain using 23^{rd} order FIR filters with 11-samples delay. These FIR filters are designed by the least-squares method to fit to the ideal frequency responses at 1000 uniformly spaced frequencies up to the Nyquist frequency, i.e. 1 kHz, with rectangular window weighting between $0.1f_n$ to $0.9f_n$. The sensor's transfer functions are represented in the time domain using a set of modal filters with each a 3^{rd} order IIR filter.

The structure is excited by a random primary point force, $F_p(t)$ (band-passed filtered using a 5^{th} order elliptical filter with normalised edge frequencies of $0.1f_n$ and $0.9f_n$) acting at $(x_0/L_x, y_0/L_y) = (0.15, 0.15)$. The real-time surface velocities of the plate are measured from a 5×5 array of equally spaced sensors. The distance of the sensor array from the edges in the x and y axes are thus $L_x/10$ and $L_y/10$, respectively, and the spacing between the sensors to be $L_x/5$ and $L_y/5$ in x and y directions, respectively. Figure 3.16 shows the arrangements of the accelerometers and the point force on the plate.

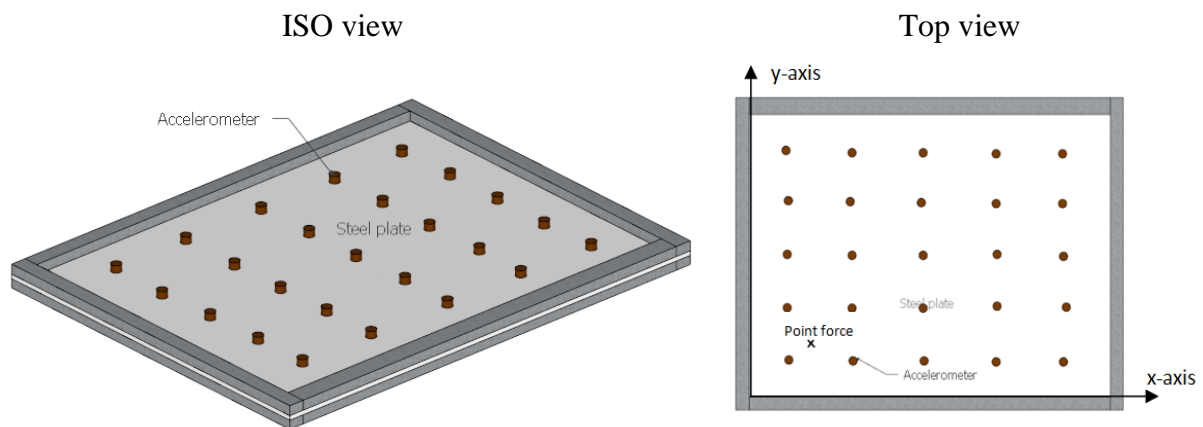


Figure 3.16: Location of sensors and point force on the clamped plate.

The comparison of the theoretical radiated sound power and its time domain estimation using ARMs is given in Figure 3.17. Note that there are 12 peaks corresponding to 12 resonance frequencies below 1 kHz, which are the same as in Table 2.4. It can be seen that the radiated sound power is estimated well across the whole frequency band of interest, i.e.

0.1 f_n to 0.9 f_n . Figure 3.18 shows the theoretical and estimated individual sound powers radiated by the first eight ARMs whose efficiencies are more than 0.1. Here, for each ARM, the estimated and theoretical sound powers are overlapped across the frequency range of interest, implying the design accuracy of these eight ARM filters. It is also clearly shown in this figure, that more sound powers are generated from the lower order ARMs at low frequencies. This is because the lower ARMs are more efficient radiators, as mentioned in Chapter 2.

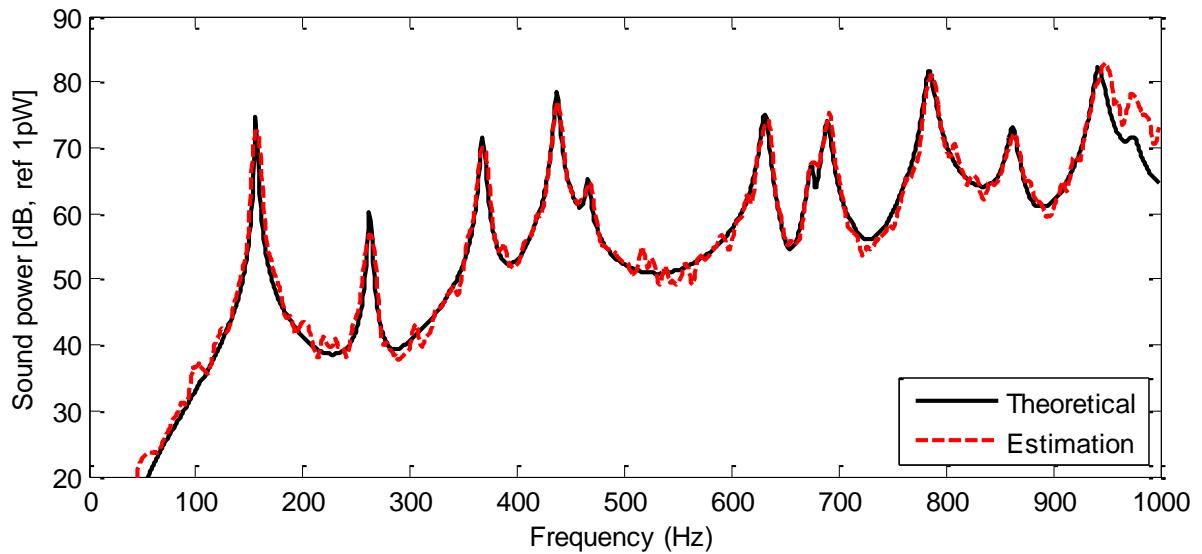


Figure 3.17: The sound power radiated from plate with primary force located at $(x_0/L_x, y_0/L_y) = (0.15, 0.15)$, estimated by ARM filters.

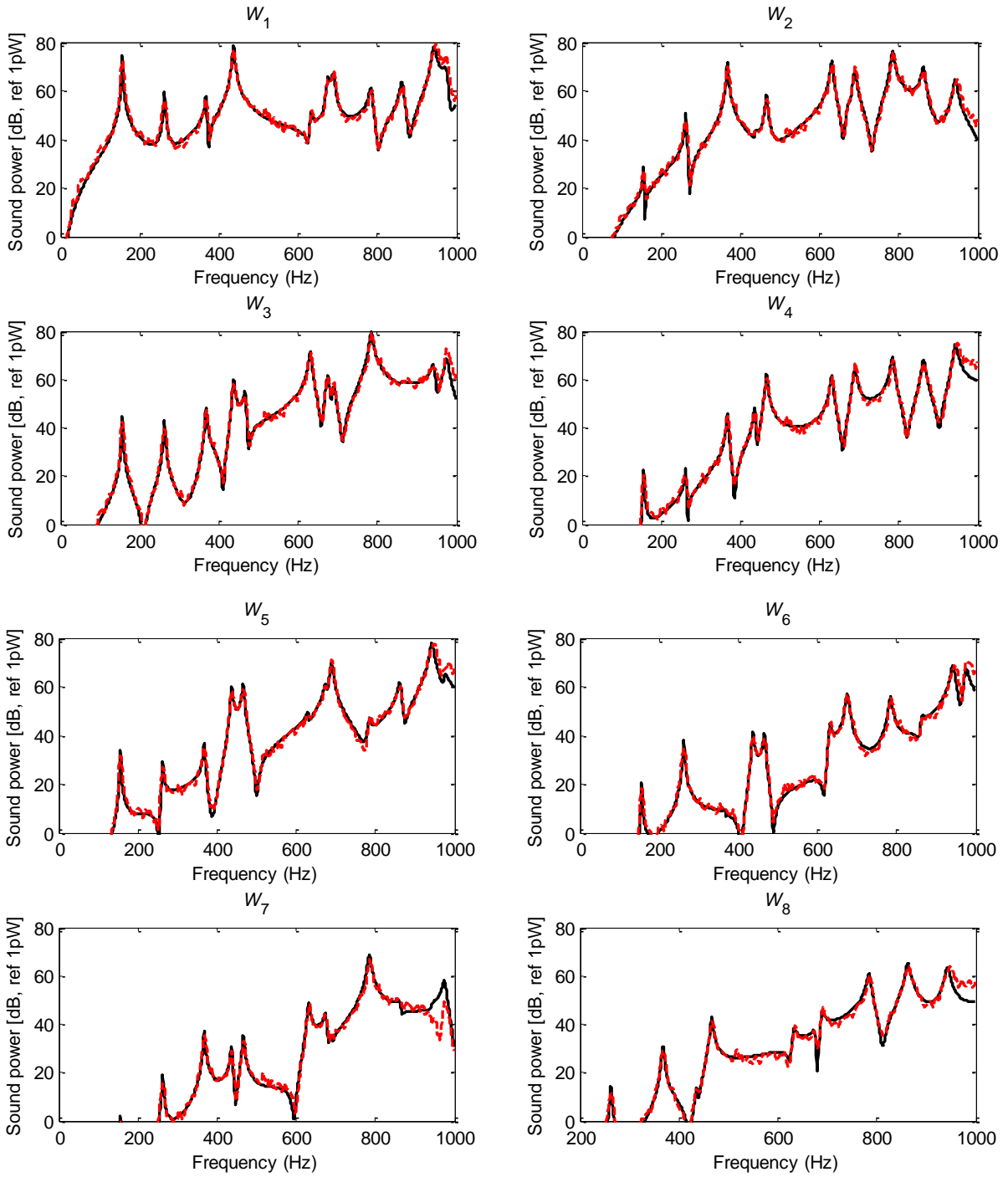


Figure 3.18: The individual sound powers radiated from plate with primary force located at $(x_0/L_x, y_0/L_y) = (0.15, 0.15)$, estimated by the first eight ARM filters.

3.8 Summary

In this chapter, a method of estimating the ARM amplitudes and hence the radiated sound power from the time-domain estimates of acoustic radiation modes was presented. The method estimates the ARM amplitudes in discrete time domain using digital filters. The chapter began with the derivation of real time ARM estimates using FIR filters. Causality is seen to be an issue, and here, causal-delayed ARM filters are proposed. This ARM filter is designed by introducing a time delay in the frequency response of the ARM estimator, so that the output of the filter will be some time later. This approach is found able to approximate the ideal frequency response of ARMs better than a truncated causal FIR filter, and thus leads to more accurate estimation. Moreover, the mean square errors between theoretical and implemented frequency response of ARMs using this approach decrease with the increase in the number of delays, hence filter coefficients, implying there is a trade-off regarding the accurate ARM filters (i.e. large d) and the amount of delays caused by the algorithm. Here, the chosen filter size of the ARM filters to be used throughout the thesis is 23, i.e. when the MSE for the first three ARM filters are below 1×10^{-3} .

For real-time simulation purposes, the structural responses from an array of sensors mounted on the radiating surface can be reconstructed in the time domain using an array of resonant filters, with each being a 3rd order IIR filter. The outputs from these resonant filters are then multiplied with the corresponding shape functions and summed to give the total response of the structure. Finally, numerical examples comparing theoretical and estimated radiated sound power from vibrating beam and plate were presented. The benefit of the real-time estimates of ARM approach is that it gives broadband estimation of radiated sound power from strongly radiating vibration. At low frequencies, it approximates the sound power as in the volume velocity approach. The ARM filters allow for the frequency dependence of the ARM shapes, and hence give a better approximation across the frequency range of interest.

The next chapter concerns real-time attenuation of radiated sound power from vibrating structures, where the feedforward controller is designed in a way that it cancels the first few ARM amplitudes. In Chapter 5, the real-time estimation of radiated sound power and control methods are verified experimentally.

CHAPTER 4 : ACTIVE CONTROL OF RADIATED SOUND POWER OF VIBRATING STRUCTURES

4.1 Introduction

The active control of radiated sound power from a vibrating structure requires knowledge of sound generation and propagation. Reduction of the structural response via active vibration control or control of the near-field acoustic field does not guarantee that the far-field sound is attenuated accordingly. This chapter outlines the methods of attenuating radiated sound power from vibrating structures actively using feedforward control strategies. Numerical simulations of real-time control are presented for two cases in this chapter, a beam and a plate, with experimental results for a plate presented in Chapter 5. As mentioned in Chapter 2, at low frequencies the first few ARMs contribute the most to the sound power radiated from a vibrating structure. This also means, using superposition, that significant sound attenuation can be achieved by introducing one or more control actuators that cancels these first few ARMs.

In Chapter 3, the real time ARM estimates were developed. They are used to estimate the instantaneous ARM amplitudes, hence the radiated sound power of a vibrating structure. Thus, in this chapter, the controller is designed in a way that it minimises the real-time ARM amplitudes. Here, two control cases are considered. The first case (Section 4.3) is the reduction of radiated sound power from a vibrating beam using feedforward control. Assuming the disturbance signal is known, the controller model is obtained from the transfer function ratio of the primary path to the secondary path and reconstructed in discrete time using an FIR filter. The second control case, discussed in Section 4.4, is adaptive feedforward control of radiated sound power from a vibrating plate. The filtered-x least mean square (LMS) algorithm is used for the automatic adjustment of an FIR digital filter used as the controller. In each case, numerical simulations showing the control performances are presented.

Next, the optimal actuator locations for the second control case, i.e. when a baffled rectangular plate is the radiator, are determined through offline optimisation. Note that the

second control case is verified experimentally and discussed in Chapter 5. Different control actuator locations give different control performance and changing the control actuator locations in the real environment is difficult. Therefore in the last part of this chapter, the offline optimisation of the actuator locations is performed using an ant colony optimisation (ACO) algorithm, although other optimisation algorithms can equally be used.

4.2 Cancellation of the first few acoustic radiation modes

As was seen in Chapter 2, the lower order ARMs are more efficient in radiating sound and generally contribute more to the radiated sound power. This also means that reducing the first few ARM amplitudes can give significant attenuation. In theory, at least j actuators are needed to control j ARM amplitudes [57]. To obtain a significant sound attenuation, ideally the first j controlled ARM amplitudes should be zero, so that

$$\mathbf{y}_c = \mathbf{Q}_c^T \mathbf{v} = \mathbf{0}, \quad (4.1)$$

where \mathbf{Q}_c is the $N_s \times j$ matrix of controlled ARMs, \mathbf{v} is the $N_s \times 1$ vector of surface velocities, N_s is the number of structural sensors and \mathbf{y}_c is the $j \times 1$ controlled ARM amplitudes. Furthermore, as a direct consequence of the linearity of the model, the velocity of the controlled plant can be obtained by the superposition principle by adding the part caused by the primary force, \mathbf{v}_p , to that caused by the j secondary forces, \mathbf{v}_s , i.e.

$$\mathbf{v} = \mathbf{v}_p + \sum_j \mathbf{v}_{s,j}. \quad (4.2)$$

Now assume that the radiator is excited by a primary force F_p , Equation (4.2) can then be written as

$$\mathbf{v} = \mathbf{H}_p F_p + \mathbf{H}_s \mathbf{F}_s, \quad (4.3)$$

where \mathbf{H}_p is the $N_s \times 1$ vector of sensor transfer functions of the primary paths (i.e. from primary force to sensor locations), \mathbf{H}_s is the $N_s \times j$ vector of sensor transfer functions of the secondary paths (i.e. the responses at the sensor locations due to the secondary forces), and \mathbf{F}_s is the $j \times 1$ vector of secondary forces. Substituting Equation (4.3) into Equation (4.1) and rearranging, gives

$$\mathbf{F}_s = -(\mathbf{Q}_c^T \mathbf{H}_s)^{-1} \mathbf{Q}_c^T \mathbf{H}_p F_p, \quad (4.4)$$

as the vector of secondary forces required to completely cancel the j ARMs [57]. Equation (4.4) can also be written as

$$\mathbf{F}_s = \mathbf{H}_c F_p, \quad (4.5)$$

where

$$\mathbf{H}_c = -(\mathbf{Q}_c^T \mathbf{H}_s)^{-1} \mathbf{Q}_c^T \mathbf{H}_p \quad (4.6)$$

is the $N \times j$ vector of control frequency responses, relating \mathbf{F}_s and F_p .

Equation (4.5) is a feedforward control law assuming F_p is known. If, on the other hand, some reference signal R is known, and $F_p = H_{pr} R$, then the vector of feedforward control frequency responses becomes such that

$$F_s = \mathbf{H}_r R, \quad (4.7)$$

where

$$\mathbf{H}_r = \mathbf{H}_c H_{pr}. \quad (4.8)$$

4.3 Feedforward active structural acoustic control applied to the vibrating beam

This section discusses feedforward control applied to the active structural acoustic control of a beam. There are two prerequisites to use the feedforward control strategy, which are: (i) the system under control is linear, and (ii) the secondary actuators are fully active [70]. The simulations are performed under certain idealised circumstances, to illustrate the approach. In feedforward control there are at least two signal paths involved. The first one is the primary path. This path consists of everything from the reference signal to the error sensors. This includes the physical system, data converters, analogue anti-aliasing filters and reconstruction filters. The other signal path is called the secondary path, between the controller output and the error sensors.

Figure 4.1 shows the block diagram representation of the feedforward ASAC system used in this thesis. It can be seen from this figure that the same reference signal that drives the primary actuator is used as an input to the series of feedforward controllers. These controllers then produce signals which, when used to drive an appropriate actuation system, are able to reduce the targeted responses. In this case, the targeted responses to be reduced are the ARM amplitudes, hence reducing the overall radiated sound power.

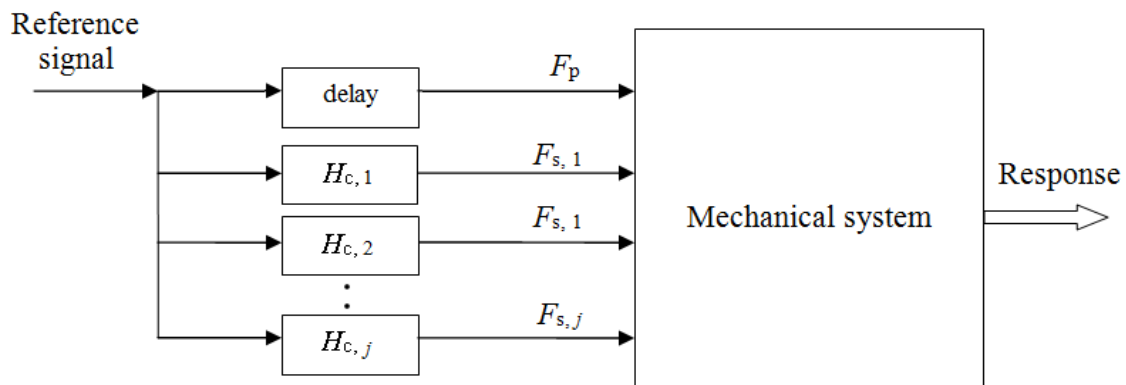


Figure 4.1: Feedforward control system.

Assume that j secondary forces are applied to control j ARMs. From Equation (4.6) the control transfer function to the k^{th} secondary force is

$$H_{c,k} = \frac{F_{s,k}}{F_p} = - \left| [\mathbf{Q}_1 \dots \mathbf{Q}_k]^T \mathbf{H}_{s,k} \right|^{-1} \left| [\mathbf{Q}_1 \dots \mathbf{Q}_k]^T \mathbf{H}_p \right|, \quad (4.9)$$

where $k = 1, 2, 3, \dots, j$. Equation (4.9) shows that the controller transfer function is highly dependent on the structural transfer function of the beam excited by the primary and secondary forces.

4.3.1 Real time implementation of feedforward controller

This section focuses on the design of controller filters to be implemented in real-time. The frequency response of the j^{th} feedforward controller in Equation (4.9) can be written as

$$F_{s,j}(\omega) = H_{c,j}(\omega) F_p(\omega). \quad (4.10)$$

In real-time, the j^{th} secondary force $f_{s,j}(t)$ is approximated by the FIR filter

$$f_{s,j}(t) \approx \sum_{n=1}^{N_s} h_{c,j}(t) * f_p(t), \quad (4.11)$$

where $h_{c,j}(t)$ is the inverse Fourier transform of $H_{c,j}(\omega)$ and also the impulse response of a filter whose frequency response is $H_{c,j}(\omega)$ and $f_p(t)$ is the inverse Fourier transform of $F_p(\omega)$.

The digital feedforward controller is designed in a manner similar to the causal-delayed FIR filter approach discussed in Section 3.2, which is found to be more accurate and stable than using IIR filters. Using the causal-delayed filter approach, a time-delay of the controller d_c is introduced to the frequency response of the j^{th} feedforward controller, which becomes $H_{c,j}(\omega) \exp(-i\omega d_c / f_s)$. By doing this, the controller filter will produce an approximation of the control force signal at time sample $m+d_c$ while the phase is linear with a time delay of d_c samples. It is reported that optimal estimation of the j^{th} controller frequency

response $H_{c,j}(\omega)$ requires $2d_c+1$ coefficients [67-68]. Hence Equation (4.11) can be written in discrete time as

$$F_{s,j}(m) \approx \sum_{s=0}^{2d_c} h_{c,j}(s) F_p(m-s-d_c). \quad (4.12)$$

It is important to highlight that the secondary force signal $F_{s,j}(m)$, which is also the output of the controller filter, is only available after d_c time samples. Moreover, since this control method is non-adaptive, a small error in the timing of the control signal will cause inaccurate control results. Therefore, the same amount of delay must be applied to the primary force reference signal to match the timing between signals from both primary and secondary paths. In numerical simulations, adding a time-delay to the input of the primary path of the system is not an issue.

4.3.2 Real-time simulation: Feedforward active structural acoustic control of beam radiator

This section demonstrates real time simulations of feedforward controller described in Section 4.3.1 in attenuating the sound power radiated from a vibrating beam, using Matlab and Simulink. The beam is simply supported at both ends with parameters given in Table 2.1. The simulation sampling frequency f_s and duration are 1024 Hz and 10 seconds, respectively. For the frequency range between 0 Hz and the Nyquist frequency (i.e. $f_n = 512$ Hz), there are 3 resonance frequencies i.e. at 36.7 Hz, 147.0 Hz and 330.6 Hz, as shown in Table 2.2. The beam is excited with a random point force $F_p(t)$ at point $x_0/l = 0.15$. A total of 3 structural sensors, equally spaced a distance $l/3$ apart, are used to measure the surface velocities of the radiator. The distance between the radiator's ends and the sensors closest from the edges are $l/6$, respectively. The real-time ARM amplitudes are then obtained by filtering the outputs of the structural sensors with the ARM filters described in Chapter 3.

In this simulation, three control cases are considered. These are cancellation of (i) the first, (ii) the first two, and (iii) the first three ARM amplitudes. Note that one control force is only able to control one ARM amplitude [57]. Thus the number of control forces for cases (i),

(ii) and (iii) are at least 1, 2, and 3, respectively. The locations of these actuators are determined by the ARM shapes and vibration modes shapes of the beam, as illustrated in Figure 2.2 and 2.7, respectively, as well as the radiation efficiencies of the ARMs in Figure 2.8. Generally, an actuator placed at a nodal point of a particular vibration mode will not be able to excite this mode of the structure. Due to the simply supported boundary conditions, exciting the structure at the end of the beam is also not possible. Moreover, to attenuate an individual ARM amplitude, the control actuator is best placed near the point where the ARM shape has the highest magnitude. In addition, the efficiency of the ARM to radiate sound power must also be considered. In Figure 2.8, the second ARM begins to radiate efficiently (i.e. efficiency > 0.1) around the second resonance frequency while the third ARM around the fifth resonance frequency (i.e. 918.5 Hz). Hence third ARM is not important here. Considering all these conditions, the chosen locations of the first, second and third secondary actuators are listed in Table 4.1. The configuration of the sensors and the actuators for this feedforward active structural acoustic control system is shown in Figure 4.2.

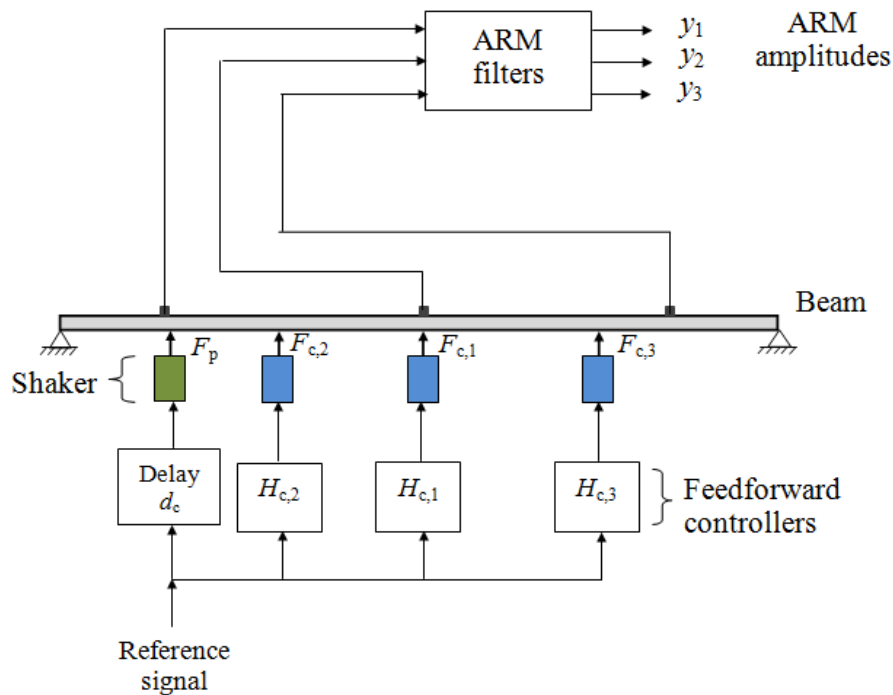


Figure 4.2: The configuration of the sensors and the actuators for the feedforward control of the sound power radiated from a vibrating beam.

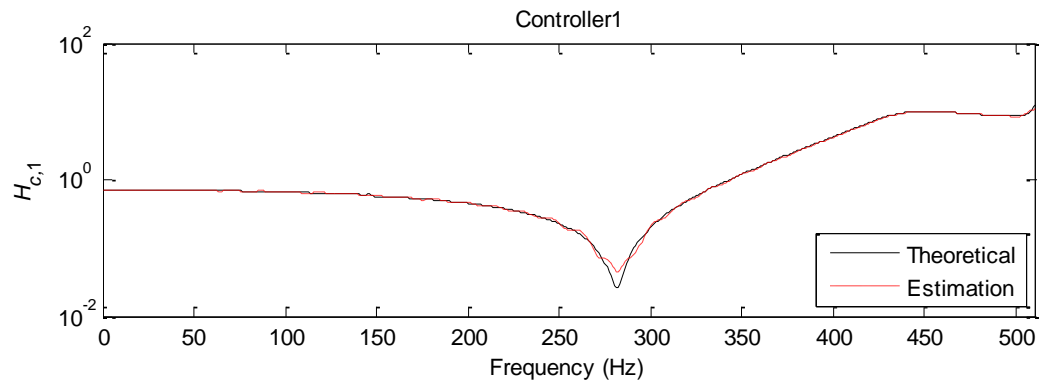
Table 4.1: Locations of the secondary actuators

Secondary actuators	Location on the beam
First	$x_{s,1}/l = 0.5$
Second	$x_{s,2}/l = 0.3$
Third	$x_{s,3}/l = 0.75$

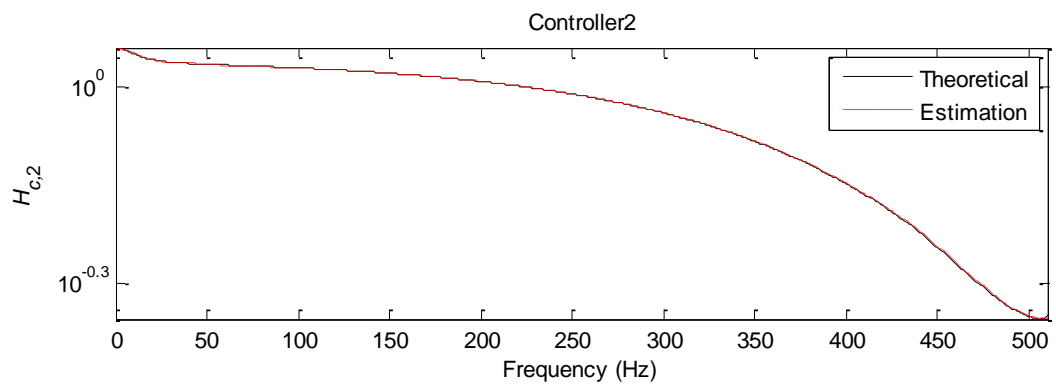
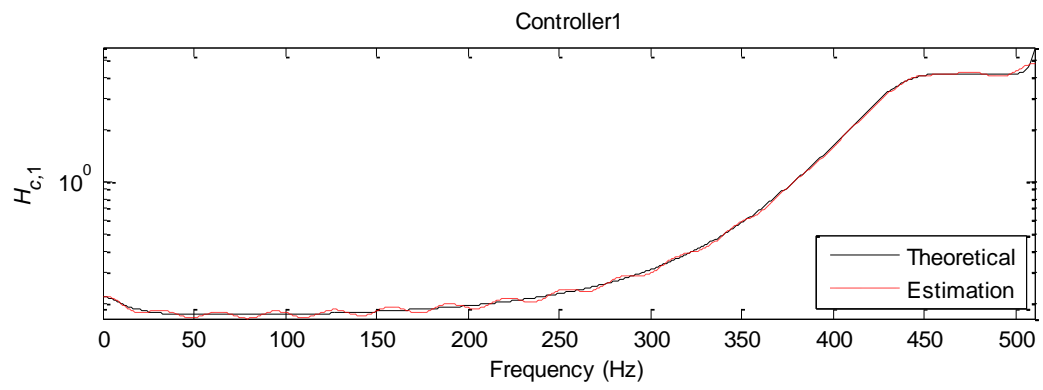
4.3.2.1 Frequency responses of the feedforward controllers

Each control transfer function to the secondary forces obtained from Equation (4.9) is reconstructed in the time domain using a 65th order FIR filter with 32-step delay. The same amount of delay is applied to the primary force reference signal to match the timing between signals from both primary and secondary paths. The calculation of the controller filter coefficients is performed by the Matlab function *invfreqz* and the frequency response of the implemented controller filter is obtained using the function *freqz*. The magnitudes of the FRFs of the theoretical and estimated feedforward controllers for the three cases considered are shown in Figure 4.3.

Overall, the implemented frequency responses of the controller are able to approximate the theoretical values reasonably well. Here, the phases of the controllers FRFs for all cases are linearly approximated with a d_c time delays. Note that these FRFs represent the transfer function ratios of the primary path to the secondary paths. In Figure 4.3(a) the controller transfer function has a minimum value (i.e. almost zero) at 281 Hz, which means that almost no secondary force is needed to control the sound power at this frequency. On the other hand, having a peak in the plot means the sound power is difficult to control at that particular frequency. Generally the occurrences of the maximum or minimum values in the plots are due to the effects of the differences in the transfer function between the primary and secondary paths. If the control force is placed at the same or a symmetric location as the primary force, the controller frequency response is expected to be approximately constant across the whole frequency range.



(a)



(b)

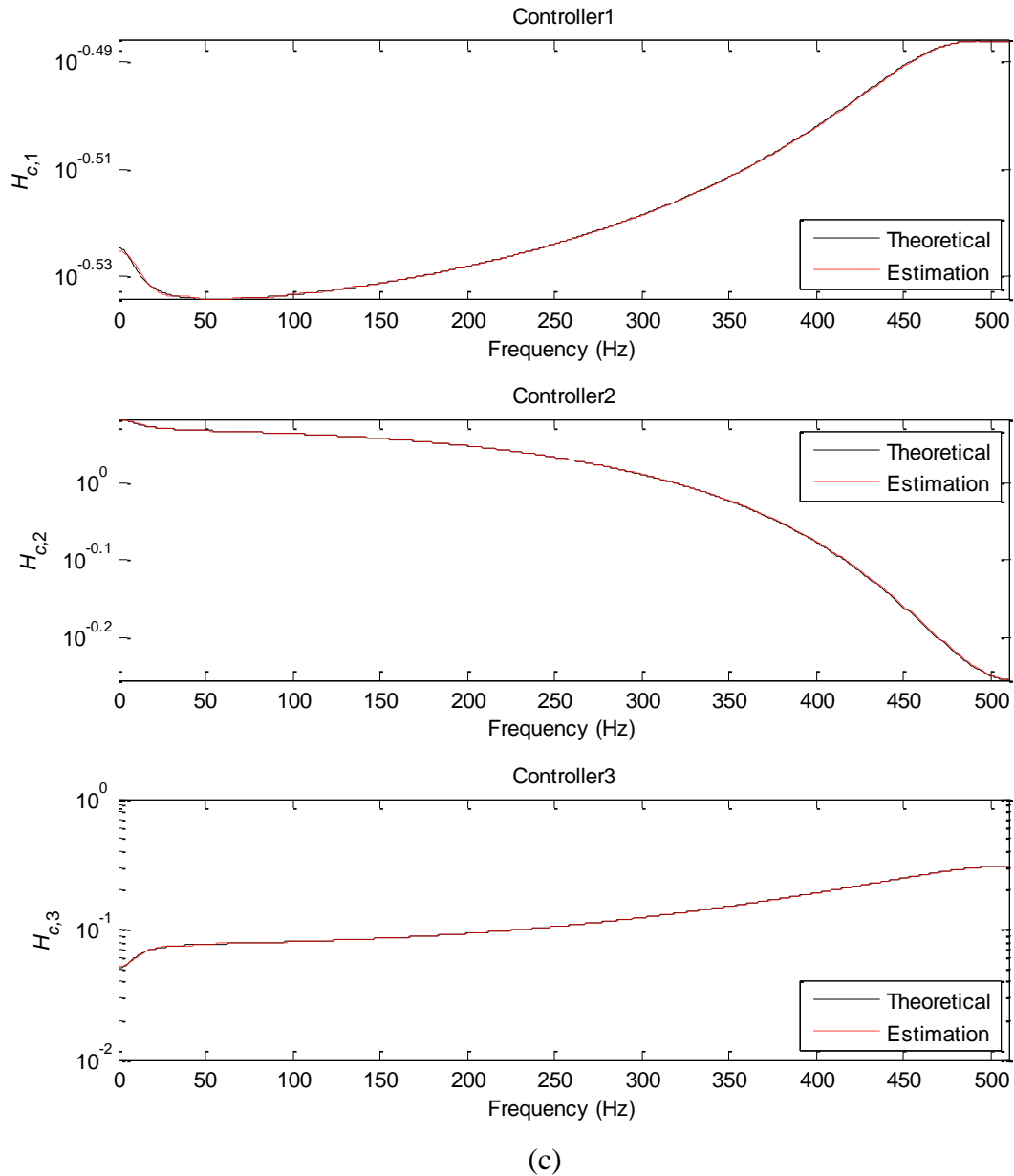


Figure 4.3: Theoretical and estimated frequency responses of the feedforward controllers using causal-delayed FIR filters for the case of cancellation of (a) the first, (b) the first two and (c) the first three ARM amplitudes, using the first, second and third control forces located at points $x_{s,1}/l = 0.5$, $x_{s,2}/l = 0.3$ and $x_{s,3}/l = 0.75$, respectively.

4.3.2.2 Control results

Figure 4.4 shows the amplitudes of the first three ARM amplitudes when cancelling (a) the first, (b) the first two, and (c) the first three ARM amplitudes. The control is turned on at $t = 5$ seconds. Note that, here, only the first 2 ARMs are important i.e. have radiation efficiencies

more than 0.1 (refer Figure 2.3). However, the third ARM amplitude is also included here to illustrate the control performance when more ARM amplitudes are controlled.

Overall, the targeted ARM amplitudes in each case are reduced significantly and almost immediately after the controllers are turned on. However, some of the non-targeted ARM amplitudes are affected as well. In Figure 4.4(a) for example, there is a small reduction in y_3 . There is also a slightly bigger reduction in y_3 when the first two ARM amplitudes are cancelled. These happen because the shapes of the first and the third ARMs are both symmetric. Similarly, those ARMs with similar symmetry will typically experience a similar effect, and vice versa.

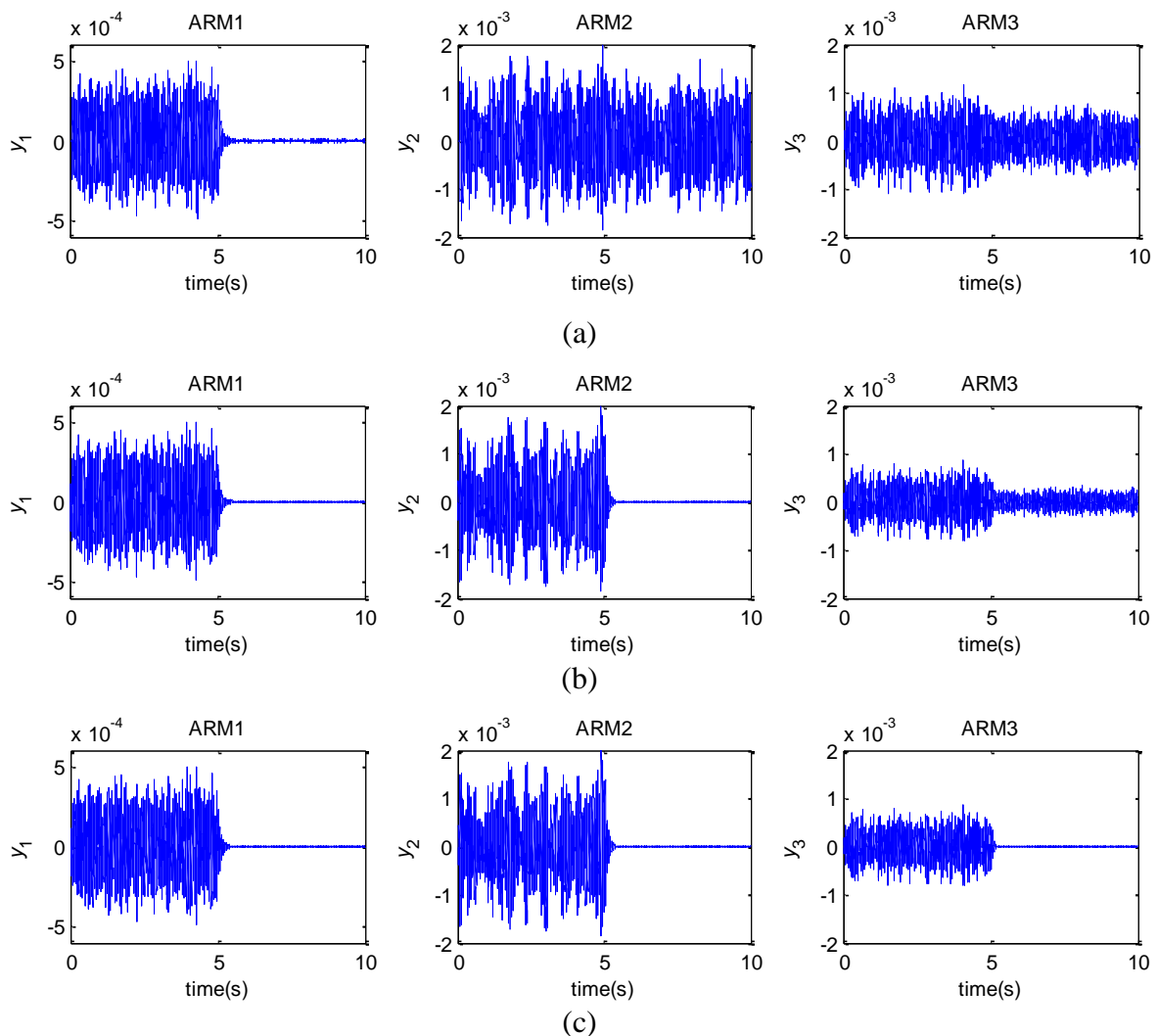
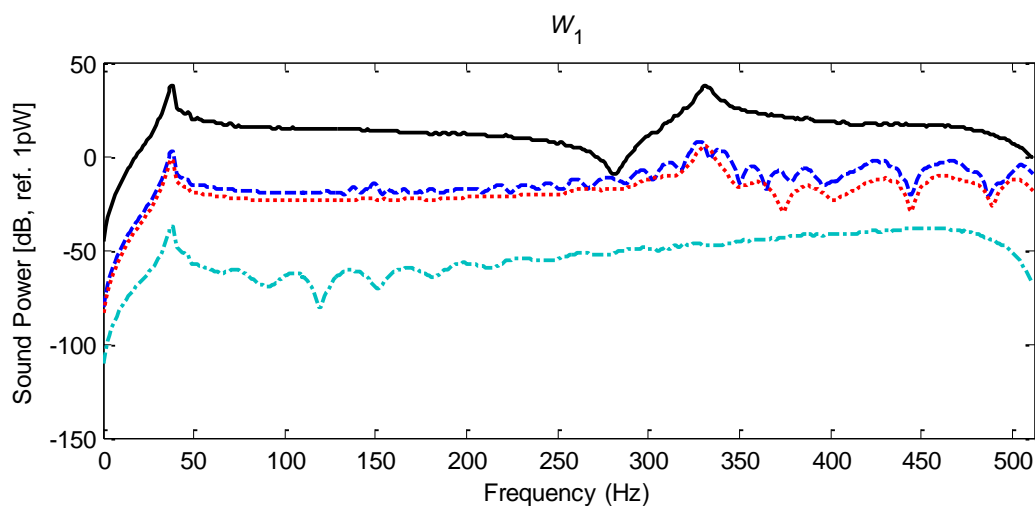
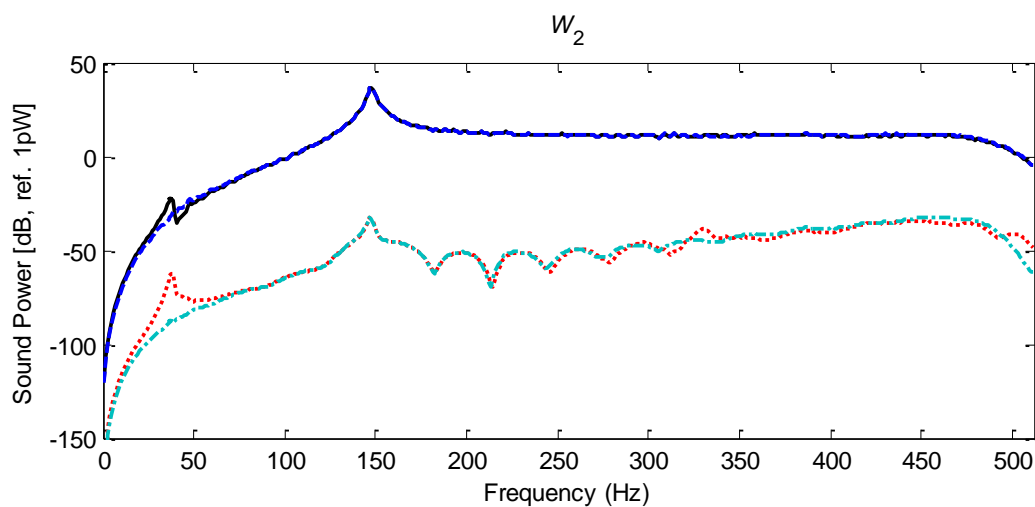


Figure 4.4: Time histories of the first three ARM amplitudes of beam for the cases of cancellation of (a) the first, (b) the first two, and (c) the first three ARM amplitudes, when the controllers are enabled at $t=5$ seconds.

Figure 4.5 shows the spectra of the uncontrolled and controlled individual sound powers from the first ARM (W_1), the second ARM (W_2) and the third ARM (W_3). It can be seen that cancelling the first ARM amplitude reduces W_1 significantly and W_3 slightly. This is due to the fact that the first and the third ARM shapes are symmetric. On the other hand, W_2 is not affected as the location of the first control actuator is at the nodal point of the second ARM. It is also worth noting that the second resonant peak is not evident in W_1 and the first and third resonant peaks are not evident in W_2 . As explained earlier, these phenomena are due to the fact that for both vibration and acoustic radiation modes, the odd modes are symmetric, while the even modes are antisymmetric. Around one resonance, one vibration mode dominates, and hence only ARMs with similar symmetry are strong radiators.



(a)



(b)

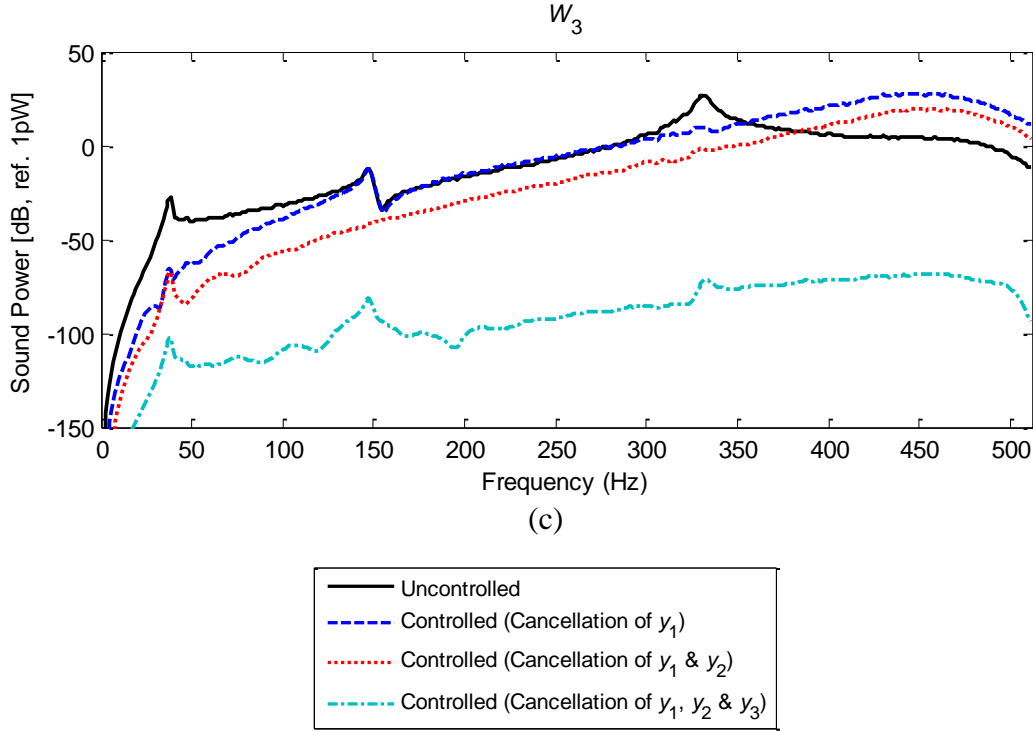


Figure 4.5: The uncontrolled and controlled sound powers from beam, contributed by (a) the first ARM (W_1), (b) the second ARM (W_2) and (c) the third ARM (W_3).

The spectra of the total radiated sound powers can be seen in Figure 4.6 for different numbers of control forces. The attenuations of the radiated sound power at the natural frequencies of the beam using up to three control forces are listed in Table 4.2. Generally, having more shakers and attempting to cancel more ARMs increases the attenuation as well as the control bandwidth. When the first ARM amplitude is cancelled, the sound power is attenuated up to the second resonance frequency, and the control bandwidth increases to 450 Hz when the first two ARM amplitudes are controlled. Moreover, cancellation of the first three ARM amplitudes attenuates the sound power for the whole frequency range of interest (i.e. 0 to 512 Hz). These happen due to the difference in radiation efficiencies of the ARMs, where the lower order ARMs are more efficient radiators (see Figure 2.3). For the frequency range of $0.05f_n$ to $0.95f_n$ (i.e. 26 Hz to 489 Hz), the frequency-averaged reduction achieved when cancelling the first, the first two and the first three ARM amplitudes are 3.1 dB, 14.5 dB and 63.8 dB, respectively.

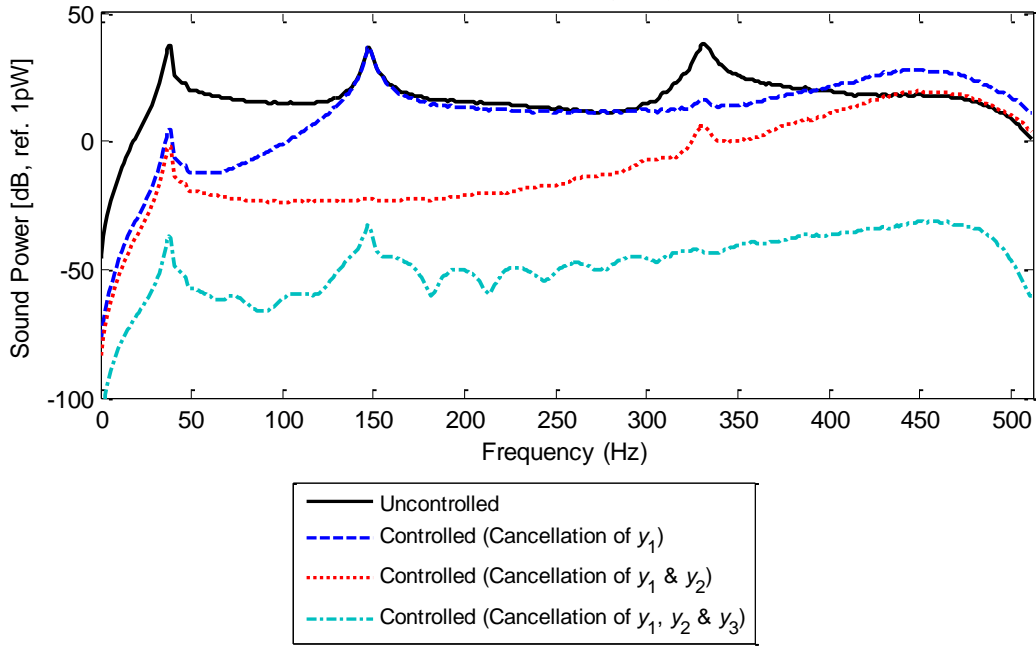


Figure 4.6: The total radiated sound powers from the vibrating beam, controlled using feedforward control.

Table 4.2: Reduction of the radiated sound powers from beam

Frequency (Hz)	Attenuation (dB)		
	Cancellation of y_1	Cancellation of y_1, y_2	Cancellation of y_1, y_2, y_3
37	32.6	39.2	74.5
147	0.0	58.9	69.3
331	21.4	31.6	81.0
Frequency-averaged	3.1	14.5	63.8

4.4 Adaptive control of radiated sound power from a vibrating plate

This section discusses the application of adaptive feedforward control for attenuating the sound power radiated from a vibrating plate. This method is basically an advanced version of the non-adaptive feedforward control discussed in Section 4.3 and it is also more practical. This is because, in an actual physical system, a delay will always exist between the reference signal and the error signal as the reference signal is propagated through the plant transfer function. Since the non-adaptive feedforward controller relies heavily on the inverse of the

transfer function, the system can give poor results due to filter approximation errors, causality issues and phase differences if this delay is not taken into account.

On the other hand, the adaptive controller can cope with effects caused by approximation errors or the delays by iteratively changing the controller filter coefficients so that the error signal is minimised. The optimal solution for the controller filter coefficients is obtained by minimising a cost function. To ensure this solution is optimal, the cost function is required to have a quadratic form. The hyper-parabolic surface characteristic of a quadratic function ensures the presence of a single, global minimum rather than having many local minima. Here, a decentralised control system is employed. In other words, there will be a number j of controllers, each meant to control a single error signal. In this research, the error signal is defined as the individual ARM amplitude.

4.4.1 Filtered-x LMS controller

The adaptive controller is designed by using the filtered-x least mean square (FxLMS) method. Here, two digital filters are required. The first filter is the estimator $\hat{G}_s(z)$ of the secondary path $G_s(z)$, which is between the controller output and the error sensors $e(m)$. The second filter is the controller filter. This filter is used to minimise the error signals from the primary path, $G_p(z)$, which is between the input signal $u(m)$ and the error signal $e(m)$. Figure 4.7 illustrates the block diagram of the filtered-x LMS algorithm. From this figure, the desired signal from the primary path, $d_p(m)$, is given by

$$d_p(m) = \sum_{k=0}^{K_1-1} g_{p,k}(k)u(m-k), \quad (4.13)$$

where K_1 is the number of samples considered for the convolution of the primary path response, and $g_{p,k}$ are the coefficients of the primary path filter.

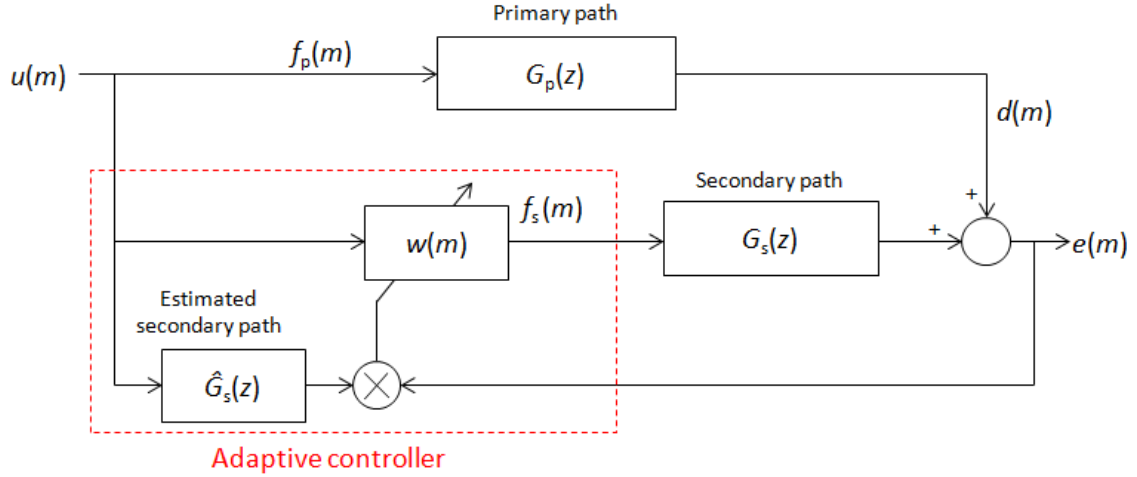


Figure 4.7: Block diagram of the filtered-x LMS algorithm.

The error signal $e(m)$ can then be calculated from

$$e(m) = d_p(m) + \sum_{k=0}^{K_2-1} g_{s,k}(k) f_s(m-k), \quad (4.14)$$

where K_2 is the number of samples considered for the convolution of the secondary path response, $g_{s,k}$ are the coefficients of the secondary path filter, and $f_s(m)$ is the secondary force signal which is also the output of the controller. Here, $f_s(m)$ is calculated from

$$f_s(m) = \sum_{k=0}^{K_3-1} w_k(k) u(m-k), \quad (4.15)$$

where w_k are the coefficients of the controller filter and K_3 is the number of controller filter coefficients. Substituting Equation (4.15) into Equation (4.14) and with some adjustment in the order of the convolutions, the error signal can be written as

$$e(m) = d_p(m) + \sum_{k=0}^{K_3-1} w_k(k) r(m-k), \quad (4.16)$$

where $r(m)$ is the reference signal obtained by filtering the input signal $u(m)$ with the impulse response of the secondary path

$$r(m) = \sum_{k=0}^{K_2-1} g_{s,k}(k)u(m-k). \quad (4.17)$$

Equation (4.16) can be written in vector form as

$$e(m) = d_p(m) + \mathbf{w}^T \mathbf{r}, \quad (4.18)$$

where $\mathbf{w} = \{w_0 \ w_1 \ \dots \ w_{K_3-1}\}^T$ and $\mathbf{r} = \{r(m) \ r(m-1) \ \dots \ r(m-K_3+1)\}^T$.

As mentioned earlier, the cost function J must be a quadratic function of the error signal to ensure the presence of optimal values for the filter weights. The cost function J is defined as the mean square error or the power of the error signal, i.e.

$$J = E[e^2(m)], \quad (4.19)$$

where $E[\]$ is the expected value. Here, the error signal is the relevant ARM amplitude. The FxLMS algorithm updates the filter weights iteratively in real-time. This algorithm relies on the steepest descent technique, in which the filter weights are updated using the negative gradient of the cost function with respect to the filter weights. The updated weights are calculated from [71]

$$\mathbf{w}(m+1) = \mathbf{w}(m) - \mu \frac{\partial J}{\partial \mathbf{w}}(m), \quad (4.20)$$

where μ is the step-size which determines the speed and stability of adaptation, while

$$\frac{\partial J}{\partial \mathbf{w}} = -2E[\mathbf{u}(m)e(m)], \quad (4.21)$$

where $\mathbf{u}(m) = \{u(m) \ u(m-1) \ \dots \ u(m-K_3+1)\}^T$. According to Widrow and Hoff [72], the filter weights can be updated at every sample time using an instantaneous estimate

of the gradient, called *stochastic gradient*. Thus, the update quantity $\frac{\partial J}{\partial \mathbf{w}}$ is equal to the derivative of the instantaneous error with respect to the filter weights,

$$\frac{\partial e^2(n)}{\partial \mathbf{w}} = -2\mathbf{u}(m)e(m). \quad (4.22)$$

Substituting Equation (4.21) into Equation (4.20) yields [71]

$$\mathbf{w}(m+1) = \mathbf{w}(m) + 2\mu e(m)\mathbf{u}(m). \quad (4.23)$$

4.4.2 Estimation of secondary path

For a moderately to highly damped system, the model of the secondary path can be described accurately using an FIR filter. The technique of estimating a transfer function is also called system identification. In this research, offline system identification is adopted. There are at least two ways of estimating the filter coefficients of the secondary path, i.e. (i) a direct method using auto-correlation properties of the signal and (ii) iterative estimation method using LMS algorithm [71].

The first method uses knowledge of the autocorrelation of the reference signal and the cross-correlation between the reference and desired signal to estimate the FIR filter coefficients of the secondary path. This method requires information on the time histories of the signals, which involves a considerable amount of data collection to accurately estimate the path and therefore can be time consuming in practice. Also, the reference and desired signals are assumed to be stationary to avoid their correlation varying with time, which might not be accurate in practical implementation. This method however is easy to implement in simulation and will be used in the numerical simulation in this research.

The second system identification is estimating the FIR filter coefficients adaptively using least mean square (LMS) algorithm. Each filter coefficient is adjusted iteratively in order to minimise the mean square error of the secondary path $e_s(m)$ (calculated from

Equation (4.24)). A new set of weight values is produced at each iteration. If the step-size μ is kept to a sufficiently small value, the weights will gradually converge to one set of values after some time. This set of values is then taken as the FIR filter coefficients of the secondary path. This method is illustrated in Figure 4.8.

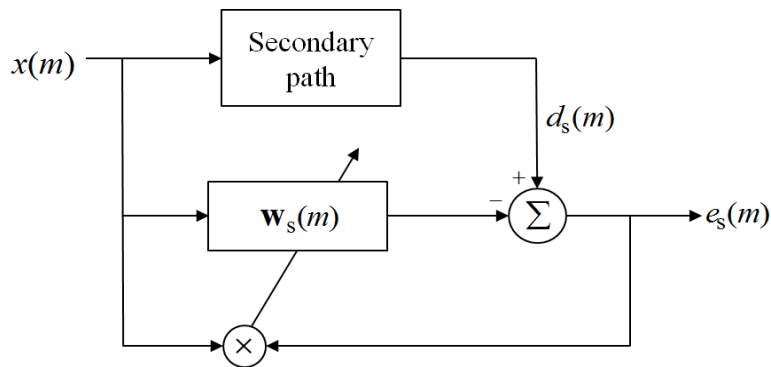


Figure 4.8: Identification of secondary path using LMS algorithm.

Here, the error is calculated from

$$e_s(m) = d_s(m) - \mathbf{w}_s^T \mathbf{x}, \quad (4.24)$$

where $d_s(m)$ is the desired signal from the secondary path, $\mathbf{w}_s = \{w_0 \ w_1 \ \dots \ w_{K_4-1}\}_s^T$ is the vector of weights of the secondary path filter, $\mathbf{x} = \{x(m) \ x(m-1) \ \dots \ x(m-K_4+1)\}^T$ is the reference signal and K_4 is the number of coefficients of the estimated secondary path filter. For the broadband estimation of an ARM amplitude, band-limited noise is used as the reference. The weights of the secondary path filter are then updated using

$$\mathbf{w}_s(m+1) = \mathbf{w}_s(m) + 2 \cdot \mu \cdot e_s(m) \cdot \mathbf{x}. \quad (4.25)$$

System identification using the LMS algorithm is able to automatically re-adjust the filter coefficients if the correlation properties of the desired and reference signals change. Due to its practicality, this system identification technique is used in the experiments described in Chapter 5.

4.4.3 Real-time simulation: Adaptive control of radiated sound power from vibrating plate

This section demonstrates the application of the adaptive controllers to reduce the sound power radiated from the 2-D radiator described in Section 4.3.1 in real-time using Matlab and Simulink. The radiator is a baffled rectangular steel plate clamped at all edges with parameters given in Table 2.3. The simulation is run at sampling frequency $f_s = 2$ kHz for $t = 500$ seconds with the average responses over a 100 s period from $t = 400$ s being found. This time is chosen to allow the controller weights to fully converge. For these parameters, there are 12 vibration modes and 8 acoustic radiation modes with efficiencies more than 0.1 in the frequency range $0.1f_n$ to $0.9f_n$, where $f_n = f_s/2$. Thus, 12 resonant filters and 8 ARM filters will be used here to calculate the radiated sound power.

The plate is excited by a random point force $f_p(t)$, while a 5x5 array of equally spaced sensors is used to measure the surface velocities of the plate. The locations of these sensors and the primary force actuator are adopted from Section 3.6.2.2. Here, three control cases are considered, i.e. cancellation of (i) the first, (ii) the first two, and (iii) the first three ARM amplitudes. Thus, three secondary force actuators are needed. The locations of the three secondary forces are listed in Table 4.3. Note that these are not optimal locations. In the next section, the optimisation of control actuator locations is presented.

Table 4.3: Locations of the control actuators on the plate

Control actuator locations	x and y coordinates
$(x_{c,1}, y_{c,1})$	(300 mm, 225 mm)
$(x_{c,2}, y_{c,2})$	(300 mm, 75 mm)
$(x_{c,3}, y_{c,3})$	(200 mm, 225 mm)

4.4.3.1 Adaptive controller settings

In the filtered-X LMS controller, the estimator filters corresponding to the secondary paths must be designed first. In this simulation, the estimation of the secondary paths is performed using Matlab function *arx*. From the time histories of the reference and the desired signals of the secondary paths, this Matlab function calculates the corresponding FIR filter coefficients of the estimated secondary paths. Here, the estimator filters for all control cases are constructed using 40th order FIR filters. To control the first 3 ARM amplitudes, 3 sets of independent adaptive controllers are needed, as illustrated in Figure 4.9.

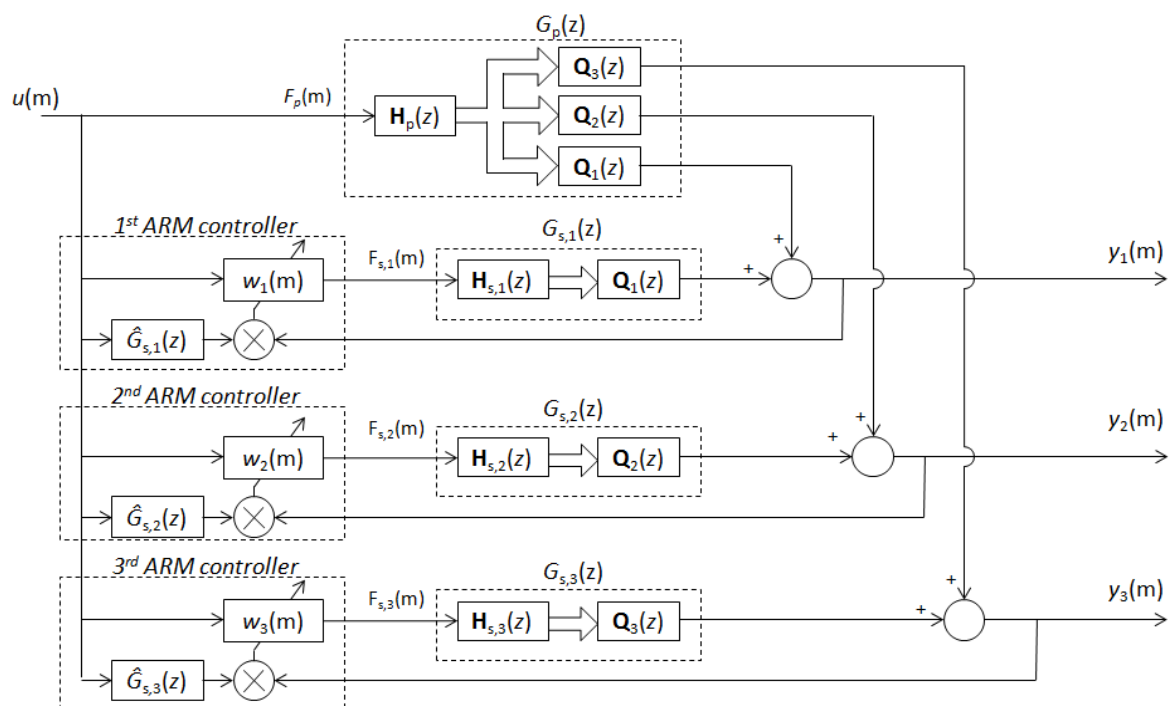


Figure 4.9: Block diagram representation of the adaptive feedforward ASAC using FxLMS algorithm.

When the adaptive controllers are turned on, it will take some time for the controllers to reach their optimum weights. To ensure the convergence of the controller weights, the convergence step-sizes for each control case are set as in Table 4.4. These values were found to be able to make the error signals converge properly.

Table 4.4: Convergence step-size

Control case	Convergence step-size μ		
	μ_1	μ_2	μ_3
Cancellation of y_1	0.0005	-	-
Cancellation of y_1, y_2	0.0002	0.0001	-
Cancellation of y_1, y_2, y_3	0.0005	0.0003	0.0003

4.4.3.2 Results of adaptive control

Figure 4.10 shows the time histories of the first three ARM amplitudes of the plate when cancelling (a) the first, (b) the first two, and (c) first three ARM amplitudes. Here, the adaptive controllers are enabled at $t = 50$ seconds to show the performance of the controllers. It can be seen that the ARM amplitudes (which are also the error signals here), gradually converge to their minimum values. Also, it is worth highlighting that the speed of the convergence is dependent on the step-size values. A larger step-size value produces faster convergence, but there is also risk of instability. In Figure 4.10(a) the magnitude of y_1 is reduced to about one quarter of its original magnitude. There are also slight increases in y_2 and y_3 . This happens because the first ARM shape is symmetric in both x and y directions, while the second and third ARM shapes are asymmetric in one direction. As mentioned earlier, those ARMs with similar symmetry will experience similar effects, and vice versa. Similar statements can be made to the plots in Figure 4.10(b), where when the first two ARM amplitudes (i.e. y_1 and y_2) are cancelled, the magnitude of y_3 is also attenuated.

Figure 4.11 shows the spectra of the uncontrolled and controlled individual sound powers for the vibrating plate contributed by the first ARM (W_1), the second ARM (W_2) and the third ARM (W_3). In general, it can be seen that the sound power from the lower order ARMs are higher at low frequencies. When y_1 is controlled, there is significant reduction in W_1 especially at 156 Hz (mode (1, 1)) and 437 Hz (mode (3, 1)), while W_2 and W_3 are almost unaffected.

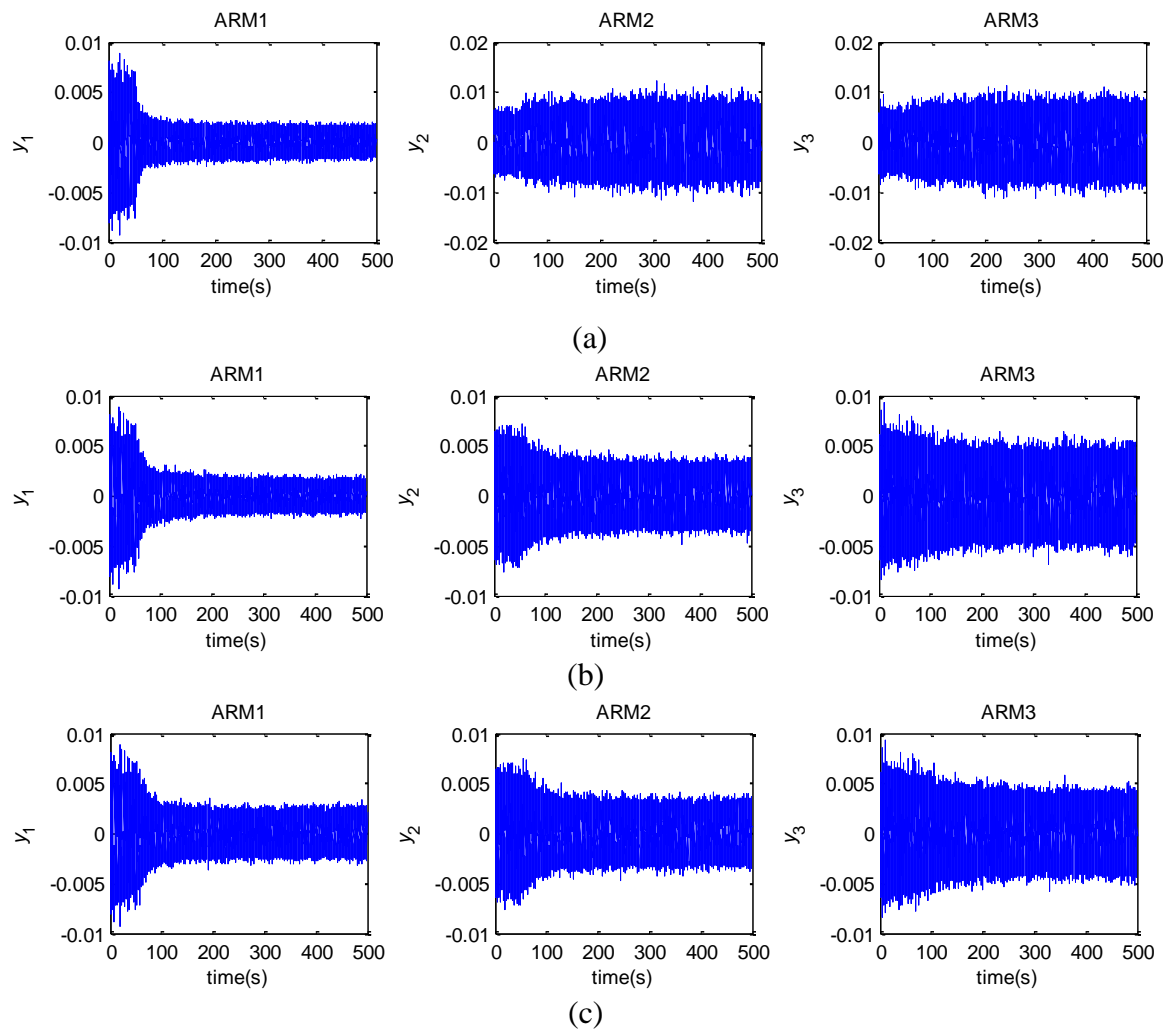
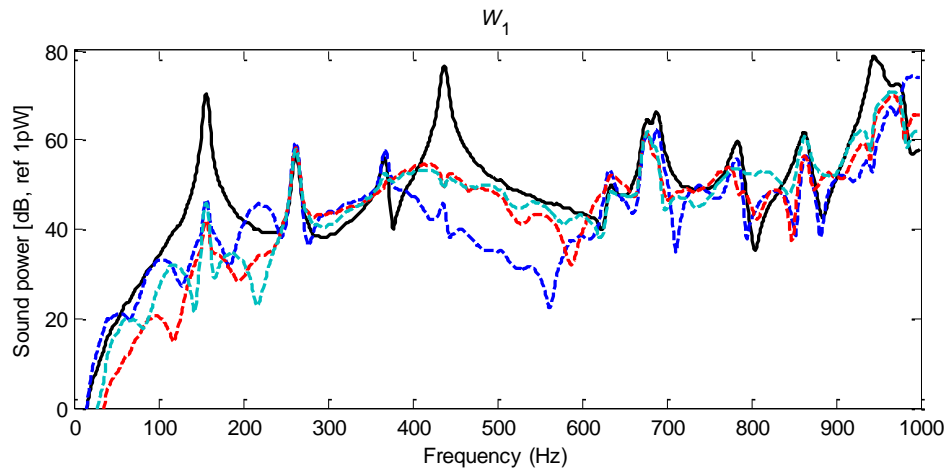
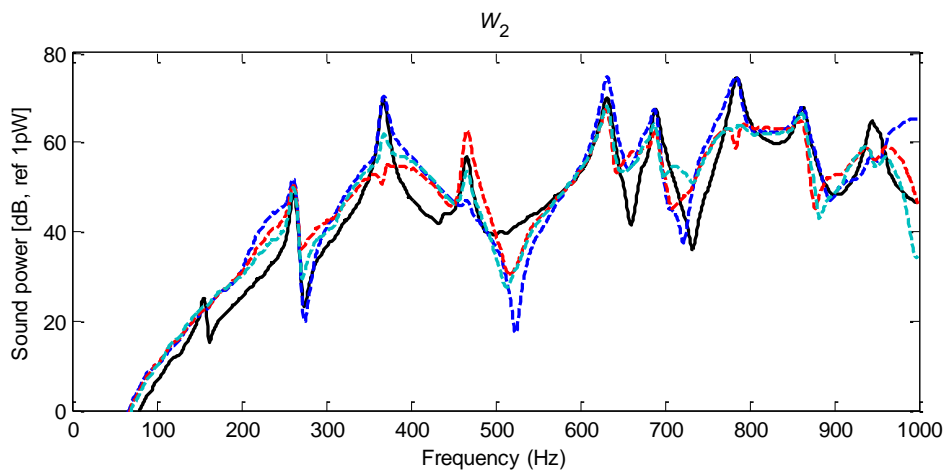


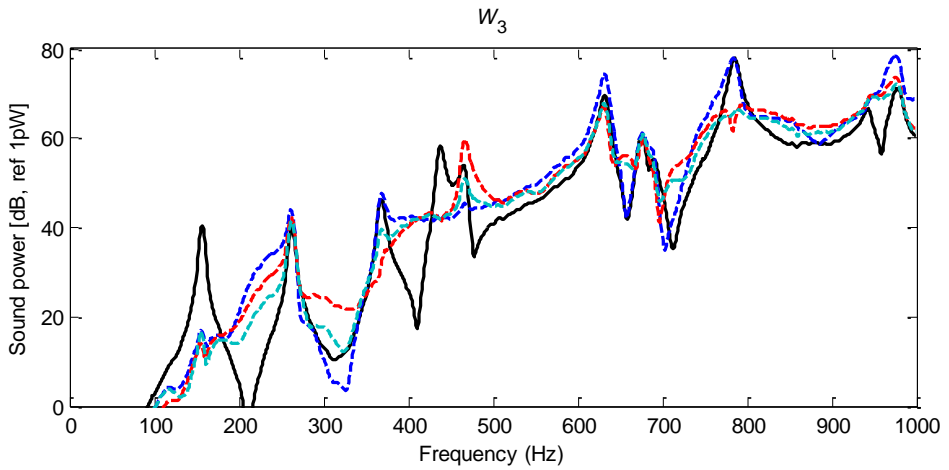
Figure 4.10: Time histories of the first three ARM amplitudes of the plate for cancellation of the first, (b) the first two, and (c) the first three ARM amplitudes, when the adaptive controllers are enabled at $t=50$ seconds.



(a)



(b)



(c)

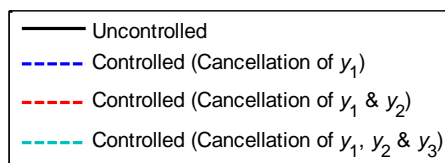


Figure 4.11: The uncontrolled and controlled sound powers from plate, contributed by (a) the first ARM (W_1), (b) the second ARM (W_2) and (c) the third ARM (W_3).

Figure 4.12 shows the results of applying adaptive control in reducing the total radiated sound power from the plate. It can be seen that substantial attenuation is achieved at the first natural frequency due to the high radiation efficiency of the first ARM. The sound powers at some natural frequencies are not necessarily attenuated when the control forces are activated. For example in Figure 4.12, when y_1 is cancelled, a significant reduction of sound power occurs at 156 Hz (mode (1, 1)) and 437 Hz (mode (3, 1)), but poor control performance at 262 Hz (mode (2, 1)). As mentioned in Chapter 2, this issue is related to the symmetry of the vibration mode and ARM shapes as well as the radiation efficiency of this ARM. If they are symmetric, then they will have the same control effect. Since the first ARM shape is symmetric in both the x and y directions, those natural frequencies with symmetric mode shapes (i.e. mode (1, 1) and mode (3, 1)) will experience some reduction in sound powers, provided that the ARM contributes significantly to the total radiated sound power. As illustrated in Figure 2.13, the sound power is dominated by the first ARM at frequencies below 210 Hz and at mode (3, 1), thus illustrating the need to control y_1 . Similar statements can be made for other control results.

The attenuation at the natural frequencies of the plate for each control case is summarised in Table 4.5. For each control case, significant reductions occur at 156 Hz and 437 Hz. Besides, poor control performance occurs at 262 Hz (mode (2, 1)) even when y_1 , y_2 and y_3 are controlled. As shown in Figure 2.12, the radiated sound power at mode (2, 1) is dominated by the third ARM. However, the actuator used to control y_3 is located at the nodal line of mode (2, 1). It can also be seen that at some resonances, employing more secondary actuators reduces the attenuation. The broadband control performances are measured using frequency-averaged reductions. Note that, as shown in Figure 2.5, the first ARM, the first three ARMs, and the first five ARMs radiate efficiently (i.e. radiation efficiency > 0.1) within the frequency ranges of $0.1f_n$ to $0.3f_n$, $0.1f_n$ to $0.5f_n$ and $0.1f_n$ to $0.9f_n$, respectively. The frequency-averaged reductions of the radiated sound power achieved from cancelling the first, the first two, and the first three ARM amplitudes within the frequency range $0.1f_n$ to $0.5f_n$ are 6.1 dB, 6.2 dB and 10.7 dB, respectively. Also, in order to control radiated sound power at higher frequencies (i.e. > 500 Hz), more control actuators are needed to control more ARM amplitudes. Based on Table 4.5, cancelling more ARM amplitudes reduces more sound powers as well increases the control bandwidth. The attenuation level and control

bandwidth can be further improved if the control actuators are placed at the optimal locations, which will be discussed in Section 4.5.

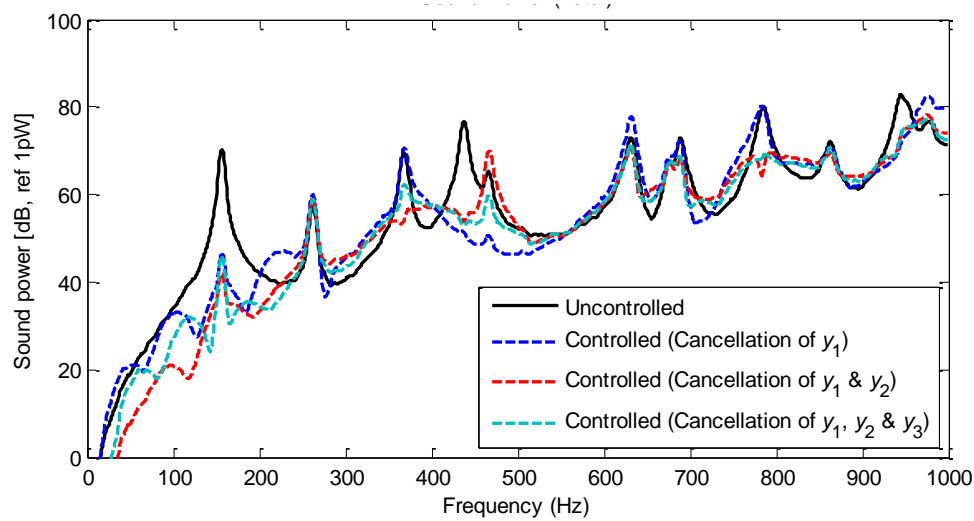


Figure 4.12: The radiated sound powers from vibrating plate, controlled using adaptive controller.

Table 4.5: Reduction of the radiated sound power from plate

Frequency (Hz)	Attenuation (dB)		
	Cancellation of y_1	Cancellation of y_1, y_2	Cancellation of y_1, y_2, y_3
156	23.7	28.3	24.3
262	-2.7	-1.6	-1.4
368	-1.0	15.6	7.4
437	25.2	22.8	23.8
466	14.5	-4.8	5.4
631	-4.7	2.6	1.9
675	-1.3	0.6	-0.1
689	1.0	5.1	4.5
784	-0.3	15.3	11.5
863	1.0	2.5	1.2
Frequency-average ($0.1f_n$ to $0.3f_n$)	8.8	10.1	10.6
Frequency-average ($0.1f_n$ to $0.5f_n$)	6.1	6.2	9.1
Frequency-average ($0.1f_n$ to $0.9f_n$)	-0.5	3.5	4.0

4.5 Optimisation of location of control actuators

This section discusses the selection of the optimal locations of the control actuators to control the radiated sound power from the vibrating plate. Similar to the simulation setup in the Section 4.4, the sensors are placed equally-spaced on the plate in a 5x5 array and the controller gains are determined adaptively. Different locations of the control actuators will result in different levels of sound power attenuation for a particular frequency range of interest. These locations also depend on the plate geometry, mode shapes and ARM shapes. Finding the optimal actuator locations manually is very difficult since there are many possible combinations of actuator locations. Therefore, an optimisation method will be used here. Optimisation is a method to find the best available value (maximum or minimum) of a given objective function from all feasible solutions. The optimisation algorithm used here is based on swarm intelligence called Ant Colony Optimisation (ACO), although other optimisation algorithms can also be used. Similar approach could also be applied to sensor locations, to optimise sensing of the selected ARMs while minimising sensitivity of other ARMs.

4.5.1 Ant colony optimisation algorithm

Ant colony optimisation (ACO) was inspired by the foraging behaviour of ants in searching for food. While searching, these ants deposit a pheromone trail on the ground in order to mark the trails that should be followed by other members of the colony. Over time, the pheromone trails decrease progressively by evaporation. Therefore, the stronger trails will be the most favourable. In most cases, these favourable trails are the shortest path between the nest and the food source.

In the ACO algorithm, artificial ants move from node to node (i.e. possible value of the optimised variable (see Figure 4.14)) and have memory of their previous actions [73]. The amount of pheromone deposited is highly dependent on the quality of the path. Artificial ants use pheromone trails, denoted by τ_{mn} , and heuristic information, denoted by η_{mn} , to build a probability of choosing an edge over others. Note subscript mn refers to the movement of an ant on the edge from node m to node n . The heuristic value is normally set to encode prior knowledge of the problem by favouring the choice of some nodes over others. In

the simple-ACO algorithm (S-ACO), a variation of ACO, the heuristic value is set to unity so that all nodes have equal chances of being selected. This S-ACO algorithm has successfully been used in many optimisation problems [74-76] and will be used here to find the optimal locations of the control actuators.

The artificial ants decide the value of variables based on the probability equation

$$P_k(t) = \begin{cases} \frac{\{\tau_{mn}(t)\}^\alpha}{\sum_{m,n \in T_k} \{\tau_{mn}(t)\}^\alpha}, & \text{if } n \in T_k, \text{ or,} \\ 0, & \text{otherwise} \end{cases} \quad (4.26)$$

where α is constant that define the relative importance of the pheromone values on the decision of an ant, and T_k is the set of all possible paths selected by the ant k at a given time. The value of the tour taken by each ant can be calculated from

$$\Delta\tau_{mn}(t) = \begin{cases} \frac{Q}{L_k}, & \text{if } (m,n) \text{ is walked by ant } k \\ 0, & \text{otherwise} \end{cases} \quad (4.27)$$

where Q is a constant and L_k is the cost of the tour by ant k . After each ant performs a complete tour, the pheromone trails are updated using

$$\tau_{mn}(t) = \sigma\tau_{mn}(t-1) + \sum_{k=1}^{NA} \Delta\tau_{mn}(t), \quad (4.28)$$

where σ is the pheromone decay $0 < \sigma < 1$ to introduce the forgetting of the bad choices and NA is the number of ants. The flowchart of the S-ACO algorithm is shown in Figure 4.13.

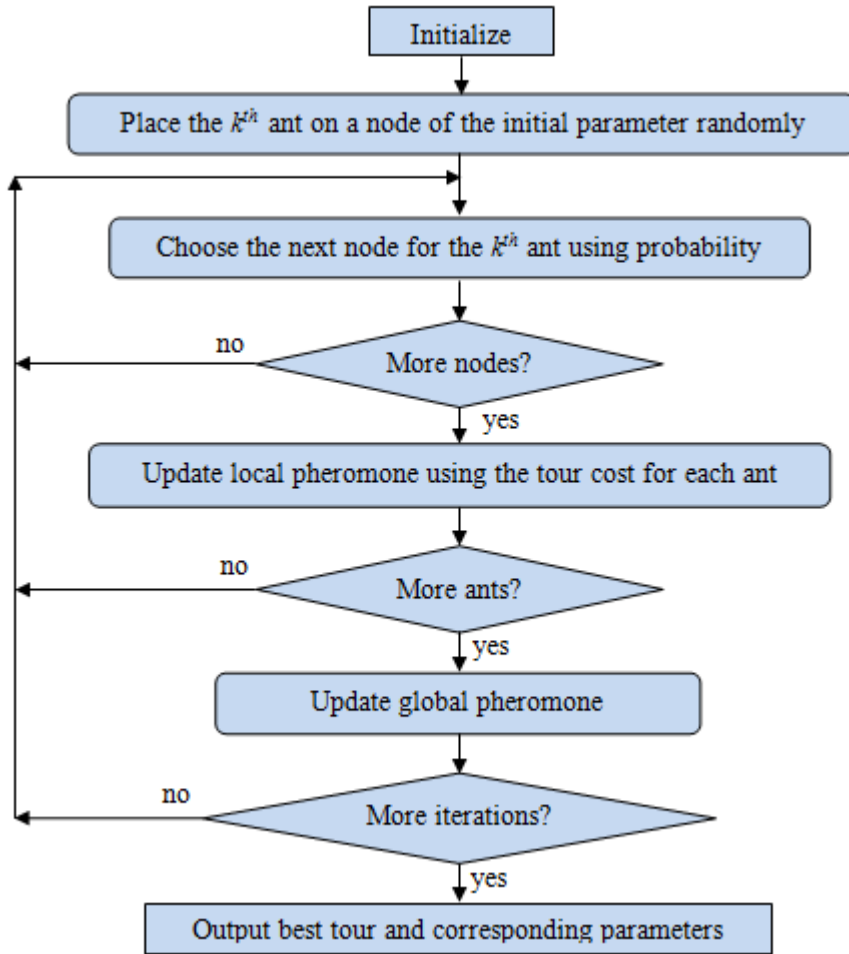


Figure 4.13: Flowchart of Simple Ant Colony Optimisation (S-ACO).

4.5.2 Objective function

This optimisation is aimed to find the three actuator locations, to minimise the first three ARM amplitudes, respectively over a frequency range from f_i to f_f . Note that each control actuator location consists of 2 variables, i.e. the x and y coordinates, thus for 3 control actuators, the number of variables is 6. It is found that optimisation of many variables simultaneously is a time consuming process, but it can be expedited by dividing it into several small optimisation steps [77].

Moreover, since the radiation efficiency of the ARM is higher for the lower order ARMs, it is appropriate to conduct the optimisation sequentially, starting from the actuator location that cancels the lowest order ARM amplitude. Also, to make sure that each location

is optimised at the optimal controller gain, the filtered-x LMS controller developed in Section 4.4, is used. Here, the controllers are allowed to run for 500 seconds to ensure that the controller gains are at their optimal values. The optimisation is divided into these three steps, which are,

- i. enable the first controller and find the optimal location of $(x_{c,1}, y_{c,1})$ that optimises the first objective function J_1 ,
- ii. enable the first and second controllers and find the optimal location of $(x_{c,2}, y_{c,2})$ that optimises the second objective function J_2 while $(x_{c,1}, y_{c,1})$ is the same as the location found in step (i), and,
- iii. enable the first, second and third controllers and find the optimal location of $(x_{c,3}, y_{c,3})$ that optimises third objective function J_3 while $(x_{c,1}, y_{c,1})$ and $(x_{c,2}, y_{c,2})$ are held constant.

The individual objective function (J_j) is defined as the minimum ratio of the controlled to uncontrolled average ARM amplitudes, i.e.

$$\min J_j = \frac{(\bar{Y}_j)_C}{(\bar{Y}_j)_{NC}}, \quad (4.29)$$

where $(\bar{Y}_j)_{NC}$ and $(\bar{Y}_j)_C$ are the frequency-average of the j^{th} ARM amplitude with and without control, respectively. These can be calculated from

$$(\bar{Y}_j)_{NC} = \frac{\sum_{f=f_i}^{f_f} (Y_j(f))_{NC}}{f_f - f_i}, \quad (4.30)$$

$$(\bar{Y}_j)_C = \frac{\sum_{f=f_i}^{f_f} (Y_j(f))_C}{f_f - f_i}, \quad (4.31)$$

where subscripts ‘NC’ and ‘C’ represent without and with control, respectively. Here, f_i and f_f are taken to be $0.1f_n$ and $0.9f_n$, respectively.

4.5.3 Optimisation settings

Due to velocity being zero at the boundaries of the clamped plate, the area in which the actuators are allowed to lie exclude a strip around the perimeter. The width of this strip was chosen to be 0.05 m. Thus, the optimisation is performed in the area $0.05 \text{ m} \leq x \leq L_x - 0.05 \text{ m}$ and $0.05 \text{ m} \leq y \leq L_y - 0.05 \text{ m}$, where L_x and L_y are chosen to be 0.4 m and 0.3 m, respectively. This area is then divided into 100×100 nodes, with the distance between consecutive nodes in the x and y directions being 0.003 m and 0.002 m, respectively. This also means there are 10000 possible locations of the control actuator. The optimisation problem is illustrated in the ACO graph in Figure 4.14. Each ant will first try to find the optimal x coordinate of the control actuator, before moving to the y coordinate. The ACO parameters used are given in Table 4.6. Note that the number of ants will determine how many random locations are chosen for each iteration and 5 ants are found sufficient for this optimisation.

Here, the plate is excited by a point force at point $(x_p/L_x, y_p/L_y) = (0.15, 0.15)$. In theory, the best location for the control actuator is exactly at the disturbance point, since the plate vibration, hence the radiated sound power, can be directly attenuated. However, in reality, it is difficult to obtain information of the external disturbance such as the magnitude and location, that causes vibration or the disturbance could be distributed over the structure. Here, the actuator locations are required to be at least 0.05 m apart.

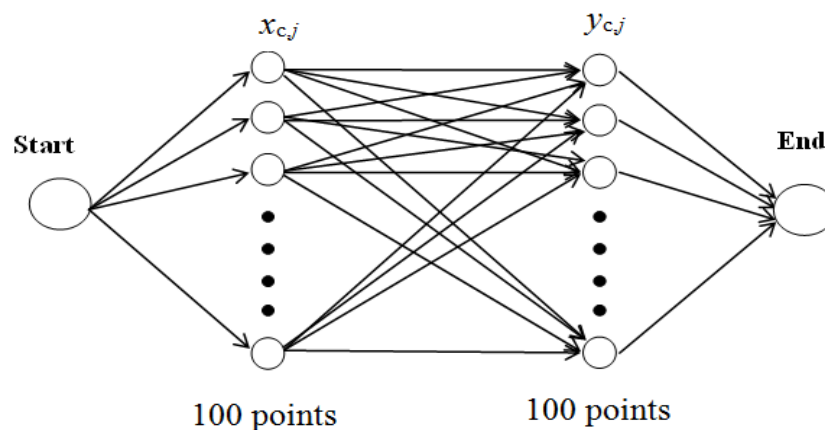


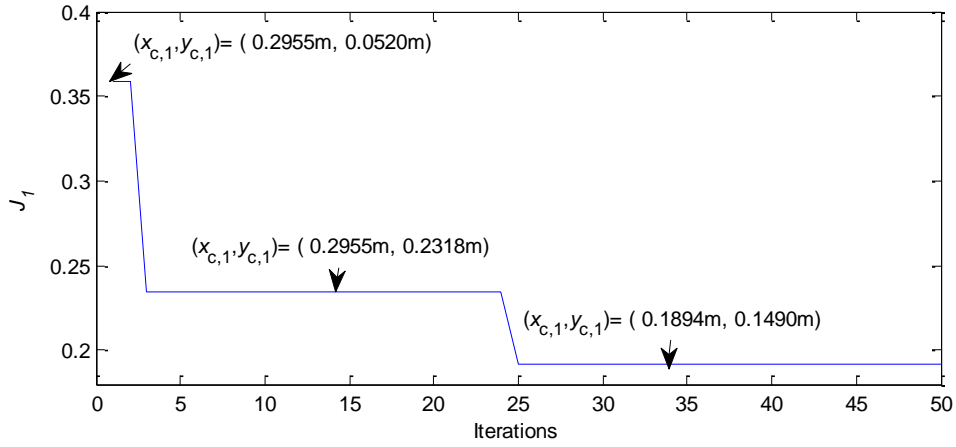
Figure 4.14: ACO graph for optimisation of j^{th} control actuator location.

Table 4.6: ACO parameters

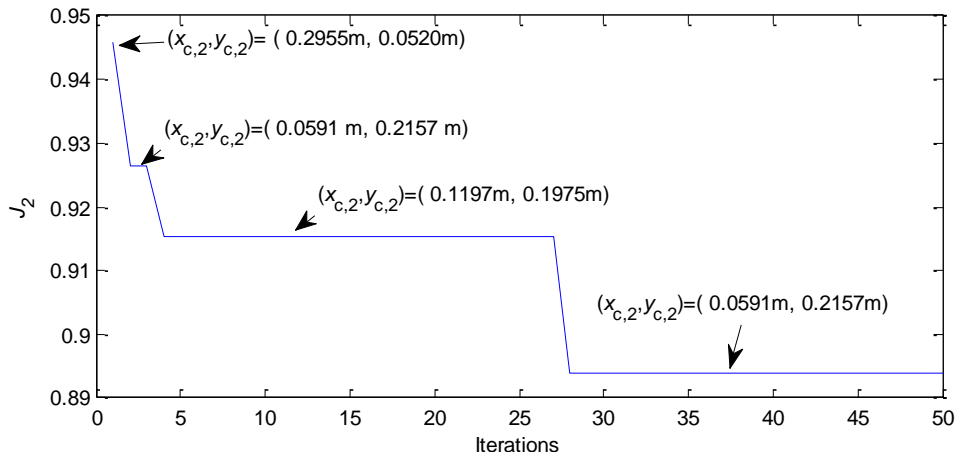
Parameter	Value
Number of ants, NA	5
Maximum generation	50
α	1
Pheromone decay, σ	0.95

4.5.4 Optimisation results

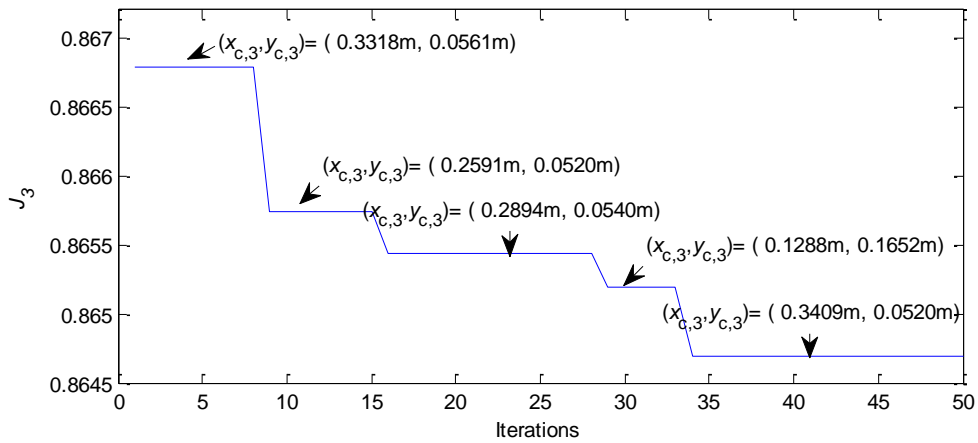
The convergences of the objective functions specified in Equation (4.29) are shown in Figure 4.15. The optimal control actuator locations generated from the optimisation are listed in Table 4.7 and shown in Figure 4.17. Figure 4.16 shows the permissible zone (in red colour) to place the first, the second and the third control actuators. From Table 4.7, it shows that the best location to place a control actuator to reduce the first ARM amplitude y_1 is close to the centre of the plate. This is because the first ARM shape has the highest magnitude at the centre of the plate. As for the second and third control actuators, the best locations obtained are near the edges of the plate. Using these optimal control locations, the time histories of the first three ARM amplitudes are shown in Figure 4.18. In Figure 4.18(a), cancelling y_1 does not affect y_2 and y_3 (as compared to Figure 4.10) because the first control actuator is placed at the node of the second and third ARMs. Since the second and third ARMs are asymmetric while the first ARM is symmetric, the attenuation of y_1 is reduced when y_2 and y_3 are cancelled.



(a)



(b)



(c)

Figure 4.15: Convergence plots when optimizing (a) the first control actuator location, (b) the second control actuator location, and (c) the third control actuator location.

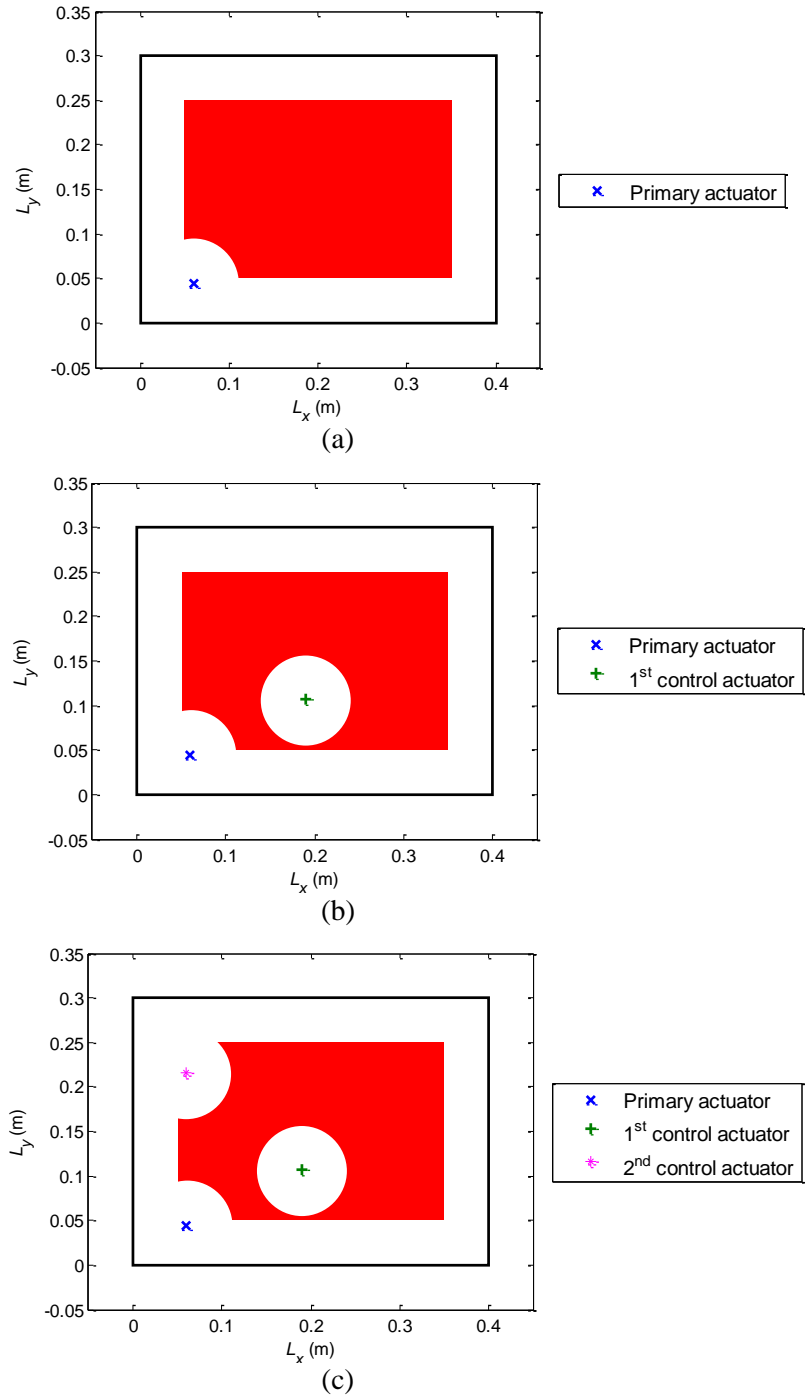


Figure 4.16: Permissible zone (in red colour) to place (a) the first (b) the second, and (c) the third control actuators.

Table 4.7: Optimal locations of the control actuators

Control actuator locations	x and y coordinates
$(x_{e,1}, y_{e,1})$	(0.1894 m, 0.1490 m)
$(x_{e,2}, y_{e,2})$	(0.0591 m, 0.2157 m)
$(x_{e,3}, y_{e,3})$	(0.3409 m, 0.0520 m)

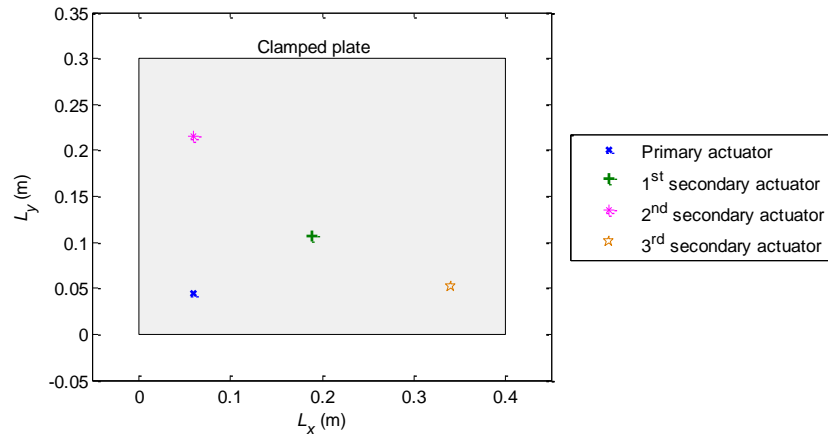


Figure 4.17: Optimal actuator locations.

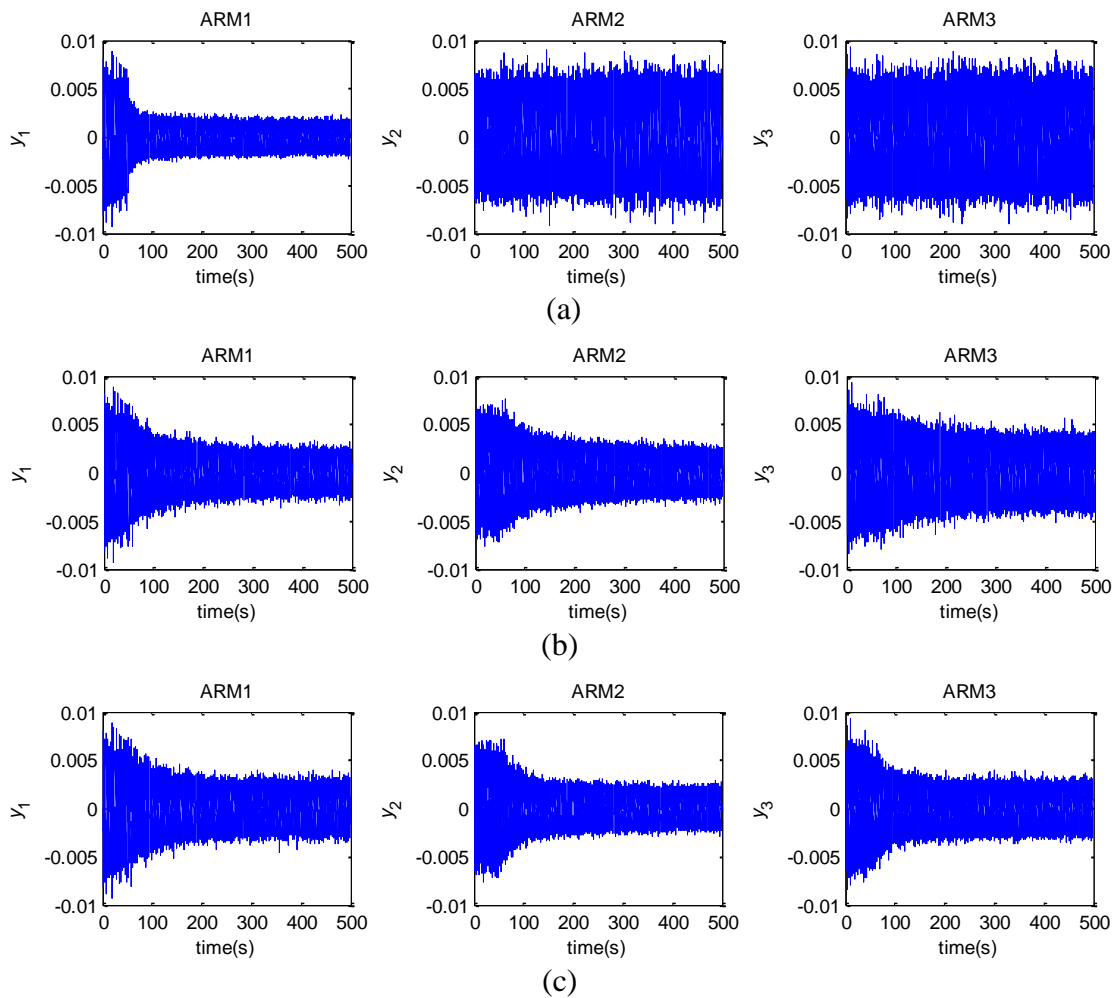


Figure 4.18: Time histories of the first three ARM amplitudes of plate using optimal control actuator locations, for cancellation of (a) the first, (b) the first two, and (c) the first three ARM amplitudes, when the adaptive controllers are enabled at $t=50$ seconds.

Figure 4.19 shows the control results when placing the actuators in the optimal locations while Table 4.8 lists the attenuation at the natural frequencies of the plate for each

control case. In Figure 4.19, substantial attenuation is achieved below 200 Hz for all three control cases, due to the high radiation efficiency of the first ARM in the lower frequency range. Comparing the plots from this figure and from Figure 4.12 (non-optimal actuator locations), the attenuations are improved in general. As shown in Table 4.8, the frequency-averaged reduction within $0.1f_n$ to $0.9f_n$, obtained when cancelling the first, the first two, and the first three ARM amplitudes are 0.5 dB, 5.1 dB and 5.5 dB, respectively. This means, the optimisation of control actuator locations increases the frequency-averaged reductions by 1.0 dB, 1.6 dB and 1.5 dB for control cases (a), (b) and (c), respectively. Similarly, more powers are reduced at the narrowband, i.e. $0.1f_n$ to $0.3f_n$, where the attenuation for control cases (a), (b) and (c) improved by 4.3 dB, 1.4 dB and 1.7 dB, respectively. Note that the results obtained here are determined by the selection of the objective function (Equation (4.29)). Different locations, and hence different levels of the control, may be obtained if a different objective function (e.g. different frequency range or weighting different frequencies by different amounts etc.) is used.

Table 4.8: Reduction of the radiated sound power from plate using optimal control actuators

Frequency (Hz)	Attenuation (dB)		
	Cancellation of y_1	Cancellation of y_1, y_2	Cancellation of y_1, y_2, y_3
156	27.5	30.5	28.4
262	2.4	2.6	2.0
368	-0.7	19.5	11.2
437	25.5	19.6	21.6
466	0.3	-0.2	0.6
631	-0.6	11.3	7.5
675	-1.9	2.7	1.9
689	4.2	7.7	4.4
784	-0.4	10.9	17.5
863	-0.3	8.1	2.7
Frequency-average ($0.1f_n$ to $0.3f_n$)	13.1	11.5	12.3
Frequency-average ($0.1f_n$ to $0.5f_n$)	6.6	8.4	8.6
Frequency-average ($0.1f_n$ to $0.9f_n$)	0.5	5.1	5.5

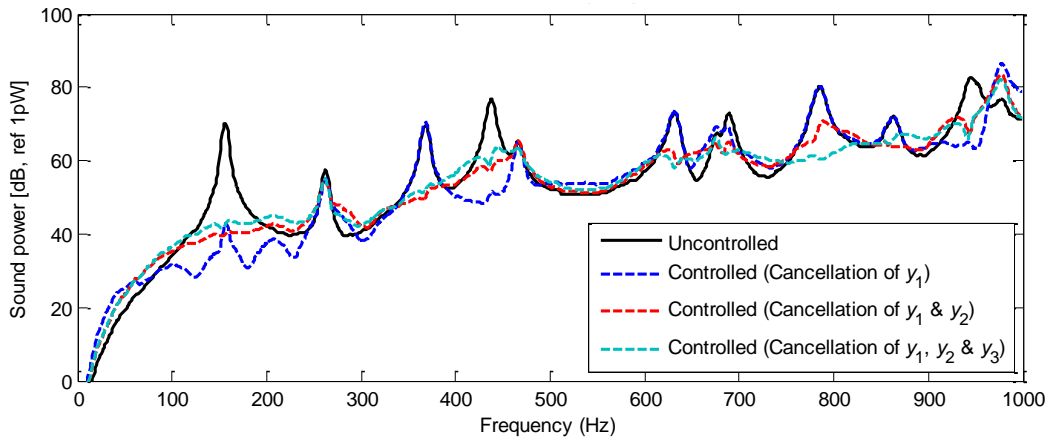


Figure 4.19: The radiated sound powers from vibrating plate using optimal control actuator locations, controlled using adaptive controller.

4.6 Summary

In this chapter, active structural acoustic control methods using non-adaptive and adaptive feedforward control strategies were presented. Numerical simulations of real-time control were presented for two, a beam and a plate, with experimental results for a plate presented in Chapter 5. The chapter began with a derivation of the control transfer functions used to cancel the first few ARM amplitudes. These control transfer functions were then used in the non-adaptive feedforward control of radiated sound power with reference to the baffled beam. For real-time simulation purposes, the controller filter was constructed using the causal-delayed FIR filter approach presented in Section 3.2. The numerical results show that the frequency-averaged attenuations achieved were 0.5 dB, 14.5 dB and 63.8 dB, when cancelling the first, the first two, and the first three ARM amplitudes, respectively.

Next, the adaptive control of radiated sound power from a vibrating plate was discussed. The adaptive controller was designed using the FxLMS algorithm, where the real-time ARM amplitudes are treated as the error signals of the controllers. Numerical simulations were first conducted using non-optimal control actuator locations and the frequency-averaged attenuation obtained from cancelling the first, the first two, and the first three ARM amplitudes within the frequency range $0.1f_n$ to $0.9f_n$ are -0.7 dB, 3.3 dB and 3.7 dB, respectively.

In the last part of the chapter, offline optimisation of the control actuator locations was performed using ACO algorithm, although other optimisation methods can equally be used. The objective of the optimisation is to find the locations that produce the maximum frequency-averaged attenuation, and the optimal locations obtained are listed in Table 4.7. The numerical results show that the attenuation for cancelling the first, the first two, and the first three ARM amplitudes are 0.5 dB (increase by 0.8 dB), 5.1 dB (increase by 1.8 dB) and 2.1 dB (increase by 0.8 dB), respectively. Different optimisation results may be obtained if a different objective function is used.

In Chapter 5, the adaptive controller developed in Section 4.4 will be implemented experimentally, where the control actuators will be placed at the locations found in Section 4.5. It is worth to highlight that the performance achieved in the simulations are not going to be achieved in practice due to other issues such as data acquisition (DAQ) resolution, noise, constraints on achievable dynamic range, small nonlinearities in sensors and etc.

CHAPTER 5 : EXPERIMENT

5.1 Introduction

This chapter presents experimental results, which aim to validate the practicality of the estimation and control of the radiated sound power of vibrating structures using the ARM approach. The radiating structure is a baffled thin rectangular plate. The chapter first describes the experimental setup used in this study, including test structure, instrumentation, sensor arrangements and software-hardware integration. Then procedures of estimating and controlling the radiated sound power are presented. Finally, experimental results are discussed for radiated sound power estimation and various control cases.

5.2 Test structure

The radiator used in the experiment is a steel plate with dimensions of 450 mm x 350 mm x 2 mm. Each edge of the plate is clamped between a pair of steel beams 25 mm wide and 10 mm thick. The screws are 40 mm apart from each other. This produces a plate clamped at all edges with area of 400 mm x 300 mm, as shown in Figure 5.1, which are the same dimensions as in the simulations. It is assumed that the plate has approximately the same parameters as in Table 2.3.



Figure 5.1: Clamped plate.

The tests were conducted in the reverberant chambers of the acoustics laboratories at the University of Auckland. The floor plan of the laboratories is shown in Figure 5.2. The test setup was built by attaching the plate in a wall between reverberation chambers A and C. Figure 5.3 shows the chambers A and C when the wall between them is removed. When the steel doors between the two chambers are fully closed, there is an opening about 1 m wide and 2.7 m high. This gap is used to attach the test structure. The gap is filled with a wall made of a wooden frame, 10 mm medium-density fireboard (MDF) plates and fibre materials for sound insulation purposes. The clamped plate is then fixed to the wooden frame of the wall so that the sound radiation is predominantly made from this steel plate. The location of the clamped plate on the opening is shown in Figure 5.4.

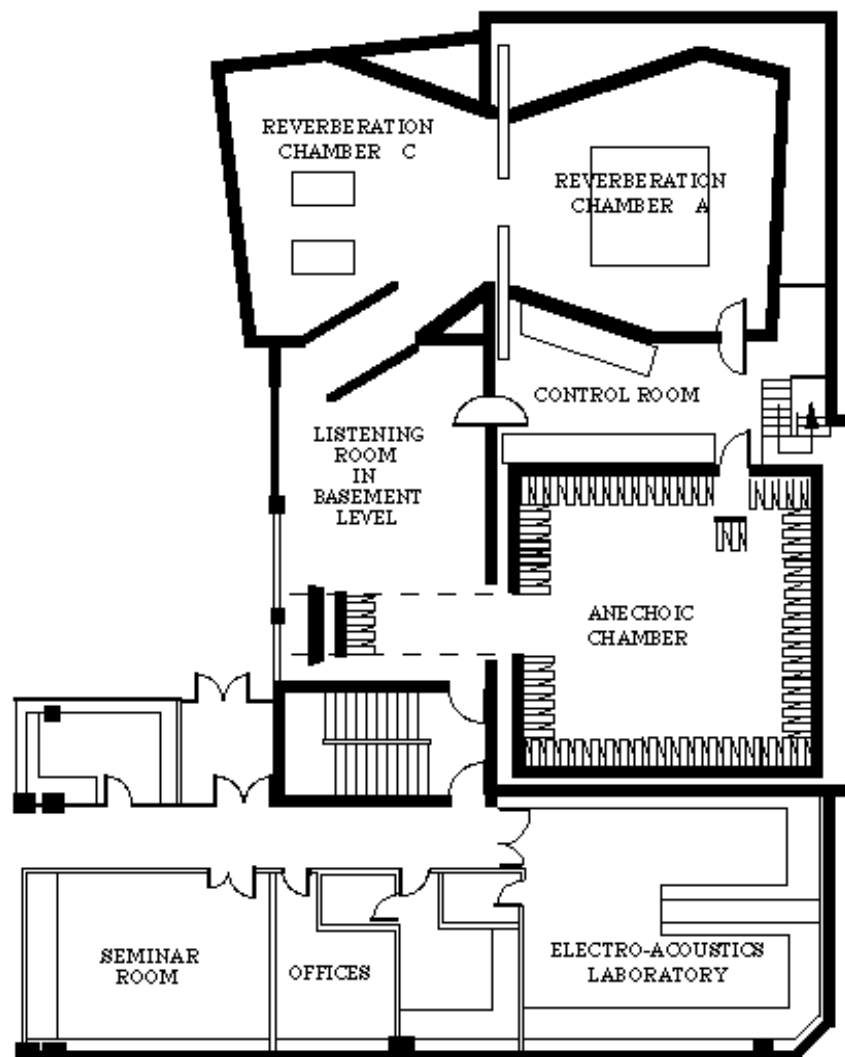


Figure 5.2: Floor plan of the acoustics laboratories at the University of Auckland.

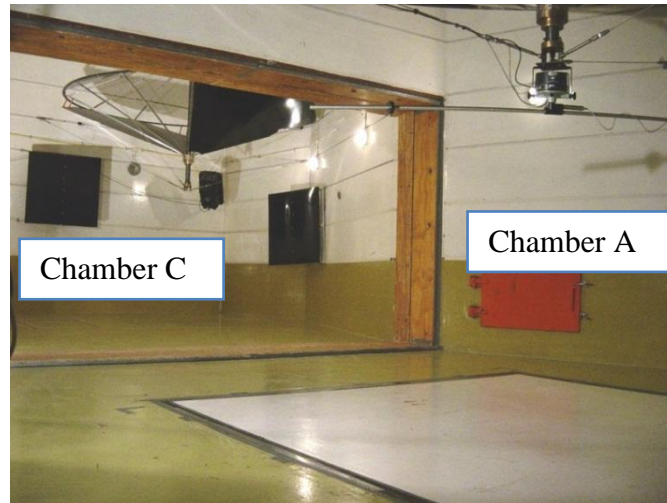


Figure 5.3: View of reverberation chamber A and C when the wall between them is removed.

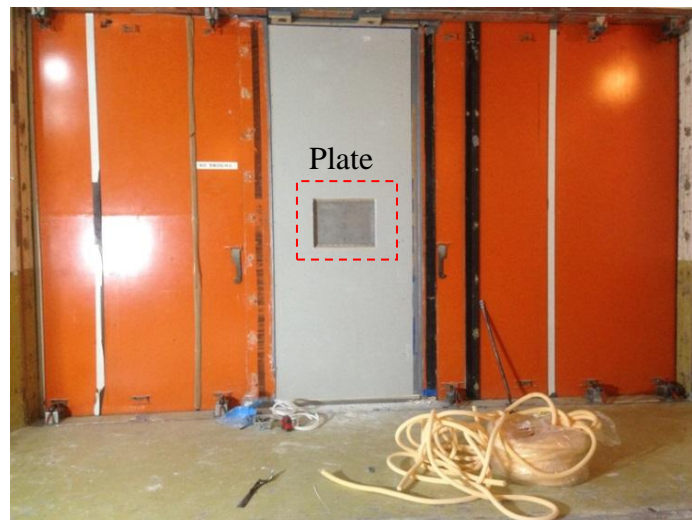


Figure 5.4: Location of the clamped plate on the wall between two reverberation chambers.

5.3 Structural sensors and actuators

The plate response was measured using a 3x3 array of equally spaced small accelerometers model 352C22 (7 units) and 352C23 (2 units) from PCB Piezotronics (Sensor specification is listed in Table 5.1). The acceleration signals from the accelerometers were input to signal conditioners (model 483B21 from PCB Piezotronics) and integrated to generate the corresponding velocity signals, before being input to the controller hardware for signal processing.

A total of four shakers model ET-132 from Labworks Inc. (specification given in Table 5.2) were used to excite the plate. One of the shakers, located at (60 mm, 45 mm) from one corner of the plate, was used to provide the primary disturbance input F_p . The disturbance signal was generated using white noise. This shaker was also equipped with a force sensor (model 208C01 from PCB Piezotronics Inc.). The other three shakers served as the control force actuators, whose aims are to reduce the first three ARM amplitudes. The locations of the control actuators are listed in Table 4.3 and shown in Figure 5.5. These locations were obtained from the optimization results presented in Section 4.5. Due to the space limitation, two shakers were attached to the plate on the side facing reverberation chamber A and the other two shakers in reverberation chamber C, as shown in Figure 5.6.

Table 5.1: Specification of the sensors

Specification	Value		
	Accelerometer model 352C22	Accelerometer model 352C23	Force sensor model 208C01
Sensitivity	(±15%) 1.0 mV/(m/s ²)	(±20%) 0.5 mV/(m/s ²)	(±15%) 112410 mV/kN
Measurement Range	±4900 m/s ² pk	±9810 m/s ² pk	0.04448 kN
Broadband Resolution	0.04 m/s ² rms	0.03 m/s ² rms	0.00045 N-rms
Frequency Range	1.0 to 10000 Hz	2.0 to 10000 Hz	0.01 to 36000 Hz
Weight	0.5 gm	0.2 gm	22.7 gm

Table 5.2: Specification of the shaker model ET-132

Specification	Value
Sine Force	4.5 lbs force pk
Random Force	3.2 lbf rms random
Shock Force	9.6 lbf pk shock
Frequency range	DC to 11000 Hz, Voltage Source mode DC to 14,000 Hz, Current Source mode
Max. Acceleration	64 g pk, bare table 26 g pk, 0.1 lb. load 9.6 g pk, 0.4 lb. load
Max. Displacement	0.20 inch pk-pk, bare table
Power Requirements	200 VA @95-125, 190-250V, 1 ϕ , 50/60 Hz

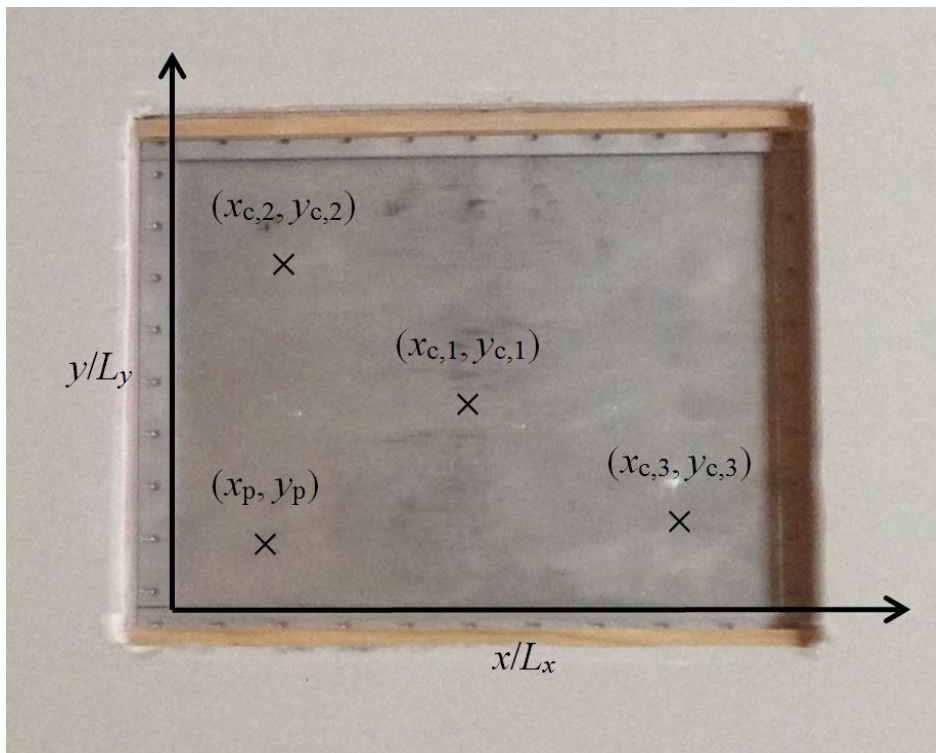


Figure 5.5: Location of the actuators on the plate (view from Chamber C).

Table 5.3: Locations of the control actuators on the plate

Control actuator locations	x and y coordinates
$(x_{c,1}, y_{c,1})$	(0.1894 m, 0.1409 m)
$(x_{c,2}, y_{c,2})$	(0.0591 m, 0.2157 m)
$(x_{c,3}, y_{c,3})$	(0.3409 m, 0.0520 m)

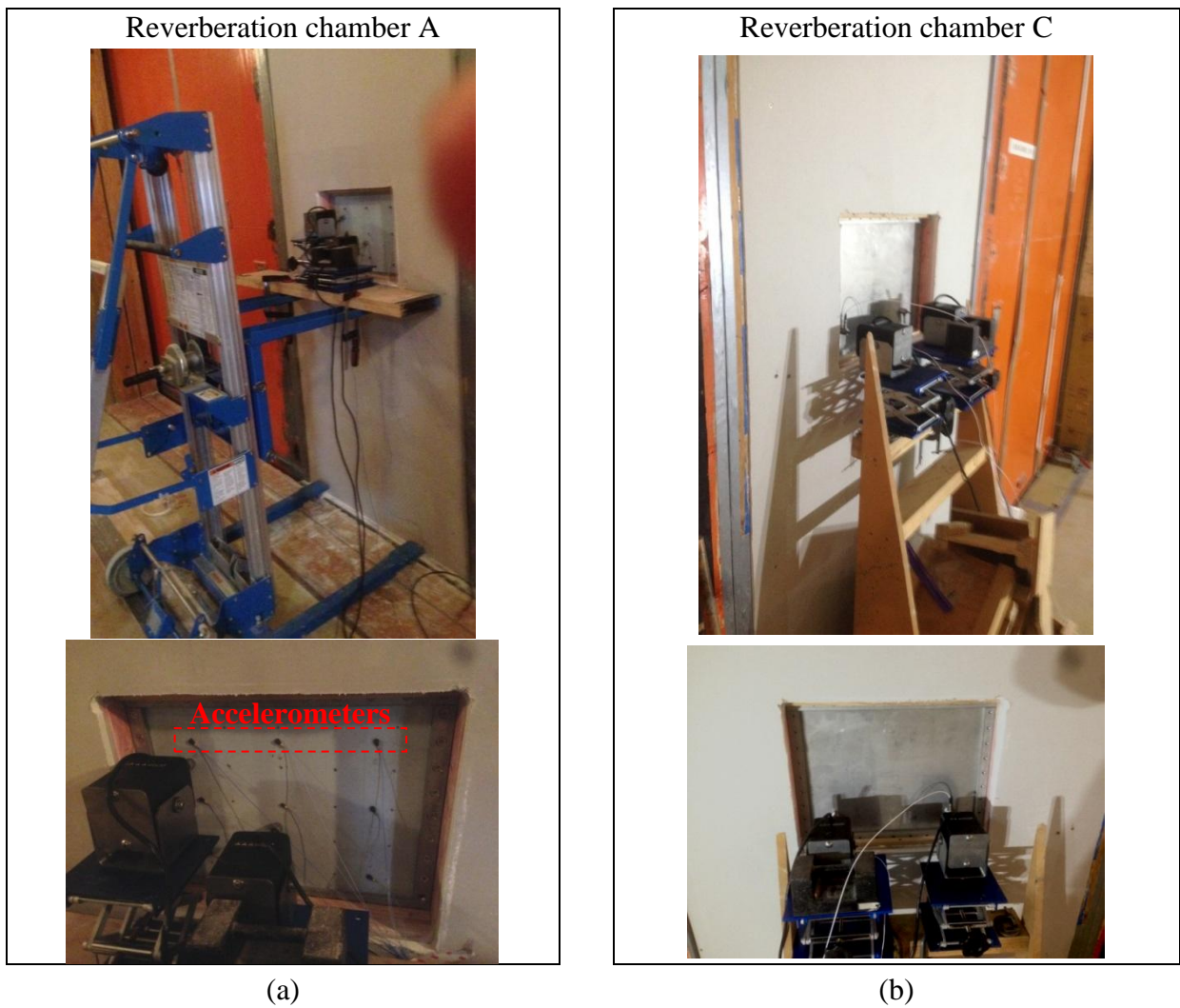


Figure 5.6: Arrangements of accelerometers and shakers attached to the plate, viewed from (a) Reverberation chamber A and (b) Reverberation chamber C.

5.4 Instrumentation

Real-time data acquisition and signal processing were performed using a National Instruments (NI) compact RIO real-time controller model c-RIO 9035. This real-time controller is embedded with a 1.33 gigahertz dual-core central processing unit (CPU), 1 gigabyte dynamic random access memory (DRAM), 4 gigabyte storage, and a Kintex-7 70T field-programmable gate array (FPGA) microchip and an 8-slot chassis. It features a real-time processor for communication and signal processing and an FPGA for implementing high-speed control, custom timing and triggering, and signal processing directly in hardware. The controller was programmed using Labview 2014 software.

Velocity signals from the signal conditioners were acquired by NI analogue input modules model NI 9234, which are equipped with four input channels. This module has a voltage range of $\pm 5\text{V}$ with 24-bit resolution. To acquire signals from the 9 accelerometers and 2 force sensors, 3 input modules were used. The system also outputs four analogue signals (i.e. 1 excitation signal and 3 control signals) through a 4-channel NI analogue output module model NI 9263, which has $\pm 10\text{ V}$ and 0 to 20 mA analogue output ranges with 16-bit resolution. These output signals were first amplified using four fixed amplifiers (from DIGITECH) before transmitted to the shakers. Figure 5.7 shows the experimental setup used in this research.

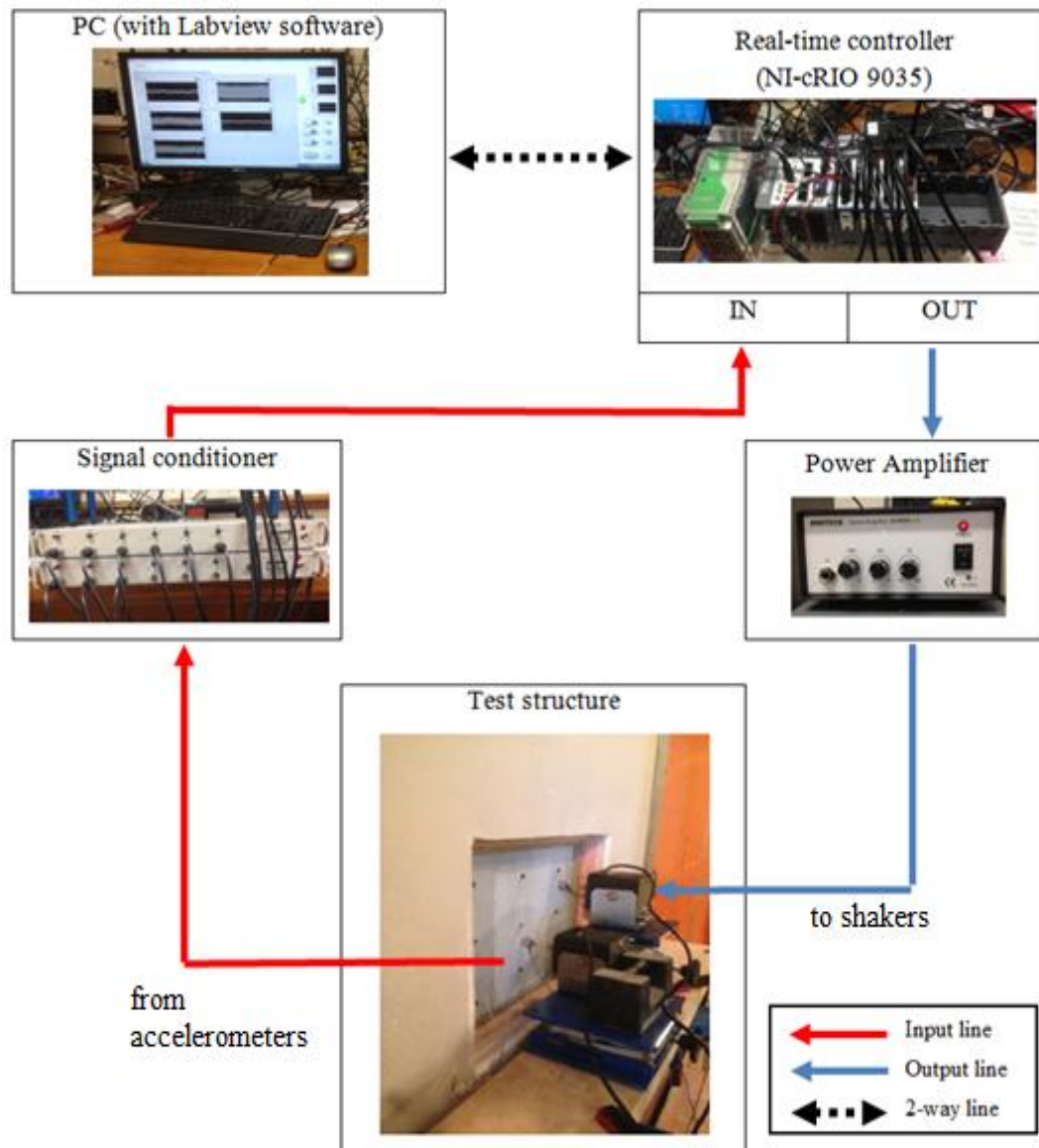


Figure 5.7: Experimental setup.

5.5 Compact RIO Controller programming

In this experiment, the Compact RIO controller was used to estimate the ARM amplitudes and control the sound power radiated from the vibrating plate in real-time. It was programmed using Labview software. Inside the controller, the code can be written in two modes, i.e. FPGA and real-time scan mode (also known as RT scan mode). The maximum clock speed for the controller to process the signal inside the FPGA and RT modes are about 40 MHz and 2 kHz, respectively. However, due to the limited amount of programming code that can be written inside the FPGA, the code was written in both modes. Code for signal

acquisition and output was written in FPGA mode as shown in Appendix A.1. The signal processing parts, i.e. signal convolution with ARM filters, FxLMS algorithm and data logging are implemented in the RT scan mode. This configuration enables the controller to run at a maximum speed of 1 kHz, without any signal loss.

In estimating the radiated sound power, the real-time ARM amplitudes were first computed by filtering the input signals obtained from the sensors with a series of ARM filters. Here, the coefficients of the ARM filters were pre-calculated using Matlab and the method presented in Chapter 3. In this experiment, only the first five ARM filters were implemented. Based on the radiation efficiencies of the plate in Figure 2.5, only the first five ARMs are important radiators for frequencies below 500 Hz. The Labview code written to implement these ARM filters is shown in Appendix A.2.

In controlling the sound power, the secondary paths of the control system, i.e. from input signals to the ARM amplitude signals were first identified using the LMS algorithm. The weights of the secondary path FIR filters were updated until the error between the desired signals (output signals from physical system) and the output signals from the secondary path filters converged. This system identification method was discussed in Section 4.4.2. Here, there are three secondary paths corresponding to the three control actuators. Each was estimated using 39th order FIR filters, which is also the maximum filter order that can be implemented in this Compact RIO controller. The Labview code written inside the Compact-RIO controller for identifying the secondary paths is shown in Appendix A.3.

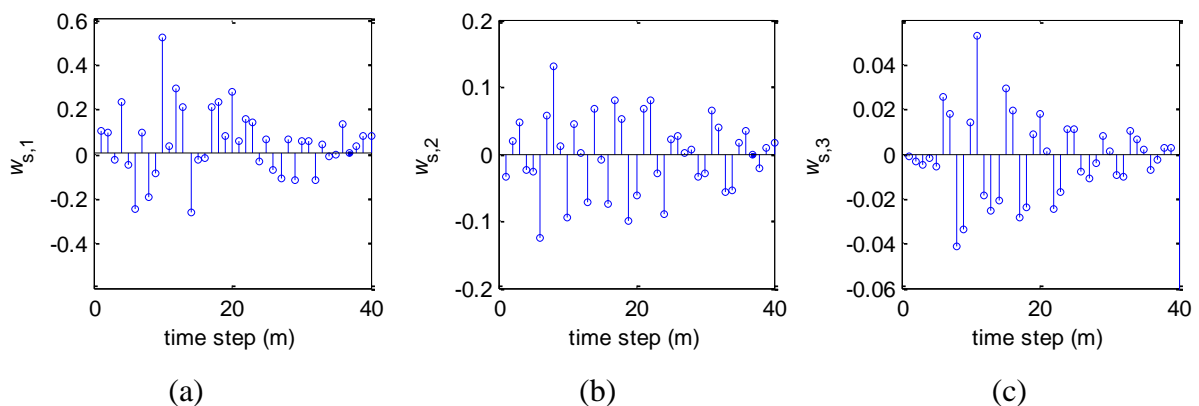


Figure 5.8: FIR filter coefficients for the (a) first, (b) second and (c) third secondary paths.

This system identification code was run for 60 seconds to allow for convergence of errors and the final coefficients of the secondary path filters obtained are shown in Figure 5.8. The filter coefficients obtained from the system identification are then used for the secondary path FIR filters inside the Labview code shown in Appendix A.4, which was used for two purposes. The first is to measure the real-time ARM amplitudes from the input signals obtained by the 3x3 array of accelerometers. These ARM amplitudes are then processed in Matlab to estimate the radiated sound power from the vibrating plate, using the method discussed in Section 3.5. The second purpose of the code is to enable the Compact-RIO controller to act as an adaptive controller using the FxLMS algorithm. Here, the controller filter is designed using 39th order FIR filter. When the control part is enabled, this code computes the appropriate control signals that minimise the error signals (i.e. real-time ARM amplitudes) in real-time. These signals are then output to the shakers attached to the plate.

5.6 Calculation of the sound power radiated from the vibrating plate

5.6.1 ISO 3741 method

The sound power radiated from the plate was measured inside the reverberation chambers by following ISO 3741. Briefly, this was done by measuring the average sound pressure of the chamber for 1 minute using a microphone (model 4190 from Bruel & Kjaer) attached to a rotating boom (model 3923 from Bruel & Kjaer), which was installed in the reverberation chamber A. The signal from the microphone was analysed using a 01dB analyser model 01381. The average sound pressure was then used to calculate the sound power in each octave or one-third octave band within the frequency range of interest using [78-79]

$$W = \bar{P} - 10 \log_{10} \frac{T}{T_0} + 10 \log_{10} \frac{V}{V_0} + 10 \log_{10} \left(1 + \frac{S \lambda_c}{8V} \right) - 10 \log_{10} \frac{B}{1000} - 14 \text{dB}, \quad (5.1)$$

where W is the band power level of the source under test (in dB, ref. 1 pW), \bar{P} is the mean band pressure level after background noise correction (in dB, ref. 20 μ Pa), T is the reverberation time of the chamber (in seconds), $T_0 = 1$ s, V is the volume of the chamber (in m^3), $V_0 = 1$ m^3 , λ is the wavelength at the centre frequency of the octave or one-third octave

band (in m), S is the total surface area of the room (in m^2), and B is the barometric pressure (in mbar).

5.6.2 Statistical method

Based on Equation (2.9), by the definition of the radiation impedance the sound power is given by

$$\bar{W} = \sigma \rho_0 c_0 \langle |v|^2 \rangle. \quad (5.2)$$

The radiation efficiency for a rectangular simply supported plate can be estimated from [79]

$$\sigma \approx \frac{\lambda_c^2}{A} \left(2g_1 + 2 \frac{L_x + L_y}{\lambda_c} g_2 \right). \quad (5.3)$$

Here g_1 and g_2 are given by

$$g_1 = \frac{4}{\pi^4} (1 - 2\alpha_1^2) \frac{1}{\alpha_1 \sqrt{1 - \alpha_1^2}} \quad (5.4)$$

$$g_2 = \frac{1}{4\pi^4} \frac{(1 - \alpha_1^2) \ln \left[\frac{(1 + \alpha_1)}{(1 - \alpha_1)} \right] + 2\alpha_1}{(1 - \alpha_1^2)^{3/2}}$$

where $\alpha_1 = \sqrt{f/f_{\text{cr}}}$ and f_{cr} is the critical frequency calculated from

$$f_{\text{cr}} = \frac{c_0^2}{1.8c_L h} \quad (5.5)$$

where c_L is the speed of sound in the structure. For a steel plate, $c_L = 5790$ m/s.

5.7 Experimental results

This section discusses the experimental results for estimation and control of the radiated sound power.

5.7.1 Estimation of radiated sound power

Here, the plate is excited by the primary force shaker using random noise for 60 seconds. The frequency range considered is between 50 Hz to 450 Hz. The velocity responses obtained are shown in Figure 5.9. Based on this figure, there are eight frequencies with significant peaks, i.e. 90 Hz, 106 Hz, 133 Hz, 166 Hz, 201 Hz, 282 Hz, 333 Hz and 404 Hz. These frequencies are considered to be resonance frequencies of the clamped plate. Note that these frequencies are different from the resonance frequencies found in the simulations. This is due to the boundary conditions, which are only an approximation of clamped edges, together with the accelerometers, force sensors and shaker, which create a non-uniform structure and affected the mass and stiffness of the system slightly.

Despite this difference, the sound power estimation approach based on the ARM estimates (presented in Chapter 3) can be used here since the approach is independent of boundary conditions. Comparison of the radiated sound powers in one-third octave band calculated using ISO 3741, the ARM estimates approach and the statistical approach is shown in Figure 5.10. The one-third octave bands considered in this frequency range are listed in Table 5.4. In general, the radiated sound power estimated using ARM estimates is close to the power calculated using ISO 3741 and statistical approach. It can be seen that at most of the bands, the sound power differences between ARM estimates approach and ISO 3741 are less than 3 dB, except for the 200 and 400 Hz bands with about 4.5 dB difference. Comparing the radiated sound power between ARM estimates and statistical approaches, less than 5 dB differences are observed at most of the bands except for 200 and 400 Hz bands.

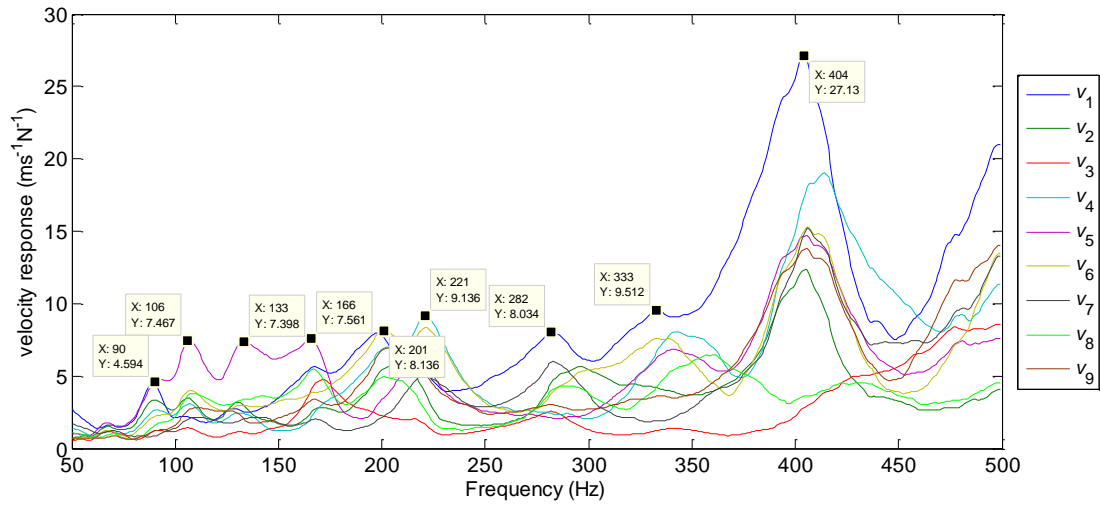


Figure 5.9: Velocity responses from the 3x3 array of sensors.

Table 5.4: Third octave band considered in the experiment

Band number	Nominal centre frequency (Hz)	Passband (Hz)
1	100	89.1 - 112
2	125	112 - 141
3	160	141 - 178
4	200	178 - 224
5	250	224 - 282
6	315	282 - 355
7	400	355 - 447

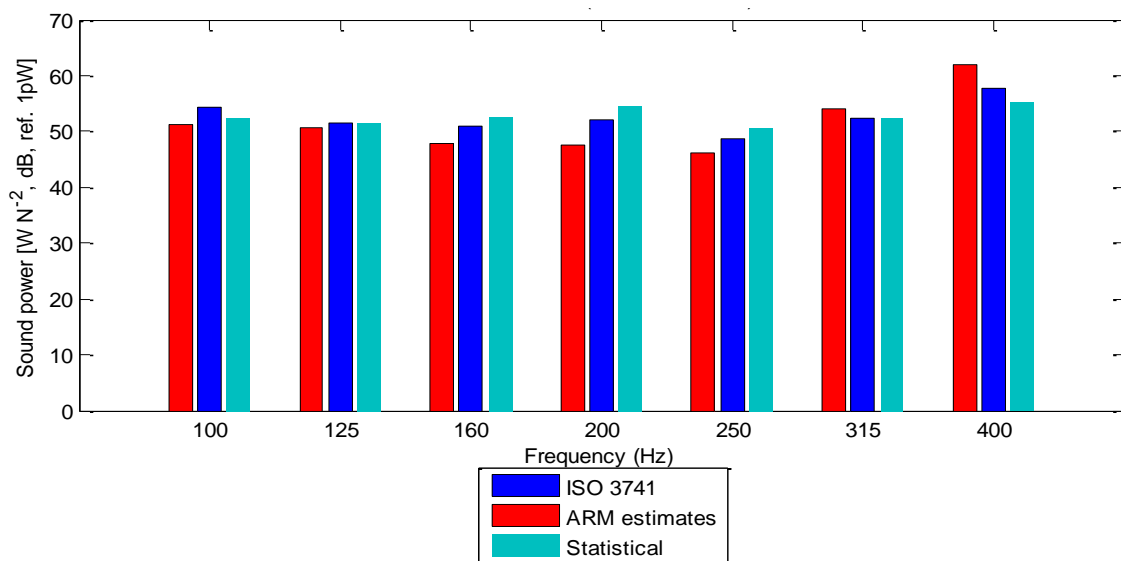


Figure 5.10: Radiated sound power measured according to ISO 3741, ARM estimates and statistical methods.

5.7.2 Control of radiated sound power using FxLMS control

The second part of the experiments was to control the sound power radiated from the plate. Two different reference signals, i.e. tonal disturbance and broadband random noise, were used to excite the plate. The adaptive feedforward controller was applied for about 120 seconds while the control performance was measured after 60 seconds from the start. Here, the FxLMS controllers were used to cancel the first, the first two and the first three ARM amplitudes. The frequency range considered in this experiment was between 50 Hz and 450 Hz.

5.7.2.1 Tonal excitation

The frequencies of the tonal signals were 100 Hz, 125 Hz, 160 Hz, 200 Hz, 250 Hz, 315 Hz and 400 Hz, which are the same as the nominal centre frequencies of the one-third octave bands in Table 5.4. The results, calculated in one-third octave bands, are shown in Figure 5.11 and Table 5.5. Since the reference signal is monotonic, the sound powers are dominant at the excitation frequency. It can be seen in this figure, when the plate is excited at 100 Hz and 125 Hz, more than 10 dB attenuation occurs for all three control cases at relevant frequency bands. The sound power is also reduced by more than 5 dB for excitation at 160 Hz. However, almost no attenuation and some amplifications occur when the plate is excited at higher frequencies, implying that the controllers are only effective at lower frequencies. As mentioned earlier in Chapter 2, the lower order ARMs are more efficient radiators at low frequencies; hence the controllers can only reduce the radiated sound power up to certain frequencies.

It is also seen in Figure 5.11 that, increasing the number of control actuators did not increase the control performance. This might be caused by the fact that, using more control actuators increases the total processing time because of the group delay associated with serial connection of hardware. Besides, the nonlinearity issues due to the attachments of sensors and actuators on the plate might also be one of the causes.

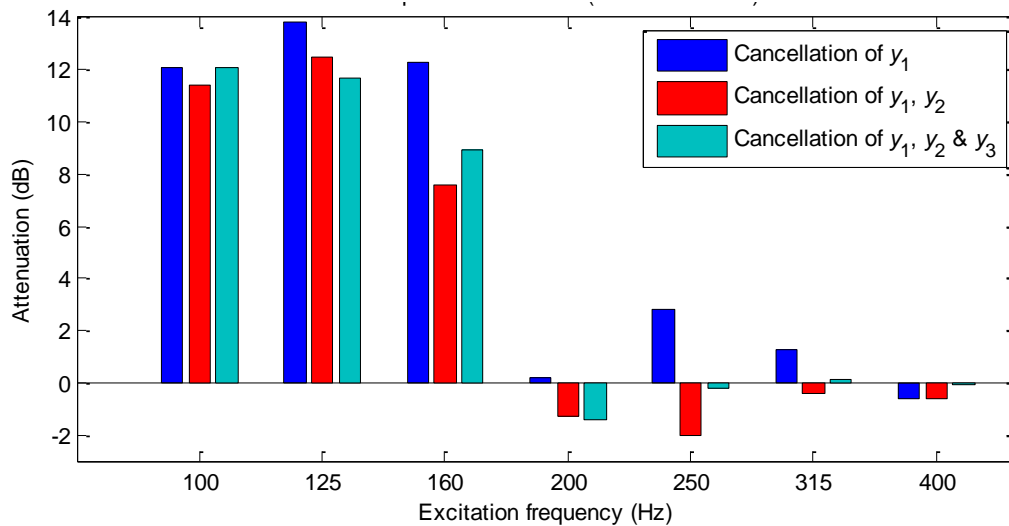


Figure 5.11: Attenuation of radiated sound power, tonal reference at various frequencies.

Table 5.5: Attenuation of the radiated sound power for tonal excitation, calculated using ARM estimates method

Frequency (Hz)	Attenuation (dB)		
	Cancellation of y_1	Cancellation of y_1, y_2	Cancellation of y_1, y_2, y_3
100	12.1	11.4	12.1
125	13.8	12.5	11.7
160	12.3	7.6	8.9
200	0.2	-1.3	-1.4
250	2.8	-2	-0.2
315	1.3	-0.4	0.1
400	-0.6	-0.6	-0.1

5.7.2.2 Broadband, random noise excitation

The control experiment was then repeated using several broadband, random noise reference signals. Figure 5.12 shows the one-third octave band attenuation of the radiated sound power when the plate was excited by broadband noise. The highest reduction is 2.2 dB obtained at Band 1 (nominal centre frequency = 100 Hz). The attenuation in the other bands is not significant, i.e. less than 1 dB, and some of the bands experienced increases in sound power.

Table 5.6 lists the attenuation of sound power at each frequency band calculated using ARM estimates approach presented in Chapter 3. There is a slight increase in the frequency-average attenuation when more than one ARM amplitude is cancelled for the frequency range between 100 Hz to 150 Hz. However, the overall control performance is trivial.

Again, the poor control performance here might be due to the same reasons as that when tonal reference signals were used, i.e. nonlinearities, group delay and secondary path FIR filter length. Besides, the length of the secondary path FIR filters (Figure 5.8) might not be long enough to estimate the secondary paths accurately, hence affecting the control performance of the FxLMS controller. In addition to that, this might be due to the signal aliasing and reconstruction issues, i.e. the signal reconstructed from samples was different from the original continuous signal. The effects of these issues are expected to be much greater for broadband noise excitation since the controller process signals with many frequencies.

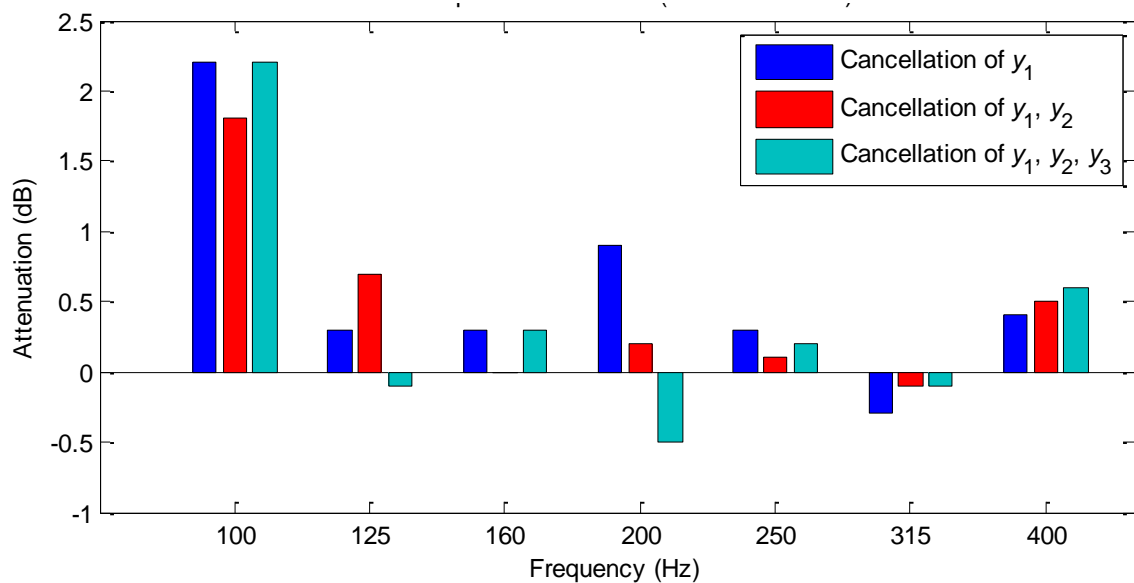


Figure 5.12: Third octave band attenuation of radiated sound power calculated according to ISO 3741, when the plate is excited by noise signal.

Table 5.6: Attenuation of the radiated sound power for noise excitation, calculated using ARM estimates method

Resonance frequency (Hz)	Attenuation (dB)		
	Cancellation of y_1	Cancellation of y_1, y_2	Cancellation of y_1, y_2, y_3
100	2.2	1.8	2.2
125	0.3	0.7	-0.1
160	0.3	0	0.3
200	0.9	0.2	-0.5
250	0.3	0.1	0.2
315	-0.3	-0.1	-0.1
400	0.4	0.5	0.6
Frequency-average (50 Hz to 150 Hz)	0.10	0.24	0.22
Frequency-average (50 Hz to 250 Hz)	0.23	0.20	0.24
Frequency-average (50 Hz to 450 Hz)	0.27	0.18	0.24

5.8 Summary

This chapter presented experimental results of the approaches discussed earlier in Chapters 3 and 4. The chapter began with the description of the experimental setup and instrumentation used in the experiment. The experiment was divided into two parts. The first part involved estimation of the radiated sound power from the vibrating plate using ARM estimates approach. The result shows that the radiated sound power estimated using ARM estimates is comparable to the sound power calculated according to ISO 3741, implying that the proposed estimation method is practical and is able to estimate the sound power under broadband conditions.

The second part of the experiment concerned controlling the radiated sound power using FxLMS controllers. Control results obtained for tonal excitation was good at low frequencies, i.e. at Band 1, 2 and 3. However, increasing the number of control actuators did

not increase the control performance. The control experiment was repeated using broadband, random noise excitation. The results were poor. The highest third octave attenuation achieved was only 2.2 dB at band 1 while the attenuation at the other bands is trivial.

The poor performance of the FxLMS controllers for broadband signals and for tonal signals of 200 Hz and above here generally might be caused by several reasons. Larger FIR filters were needed to estimate the secondary paths accurately. This was clearly a computationally intensive system that gives significant group delay. There were also signal aliasing and reconstruction issues, which caused the controller to process signals at different frequencies from the original signals, especially for the case of broadband noise excitation.

Moreover, the poor performance might also be related to the hardware issues. Attachments of many sensors and actuators might lead to modification of the system response. There might also be sound leakage through the walls. The conversion from acceleration to velocity signals using integrator in the signal conditioner might introduce phase errors to the output signals. There was also an issue on the sensor miscalibration. It is expected that better control performance can be achieved if all these issues are taken care of. This is a matter for future work.

CHAPTER 6 : CONCLUSIONS AND RECOMMENDATIONS

6.1 Conclusions

In this thesis, methods for estimating and controlling the radiated sound power using time-domain estimates of acoustic radiation modes (ARMs) were developed. Chapter 2 reviewed ARMs and radiated sound power. In Chapter 3, a method of approximating the response of ARMs using FIR filters, also called ARM filters, was proposed to answer the first research objective, which is to develop digital filters that estimate the ARMs and radiated sound power in time domain. In particular, causal-delayed ARM filters were seen to give accurate estimates with relatively few filter coefficients. These filters are designed by introducing a time delay of d steps in the frequency response of the ARM estimator, so that the output of the filter gives the estimate of the ARM amplitude d steps later (refer Equation 3.6). This approach is found to be able to approximate the ideal frequency response of ARMs better than a truncated causal FIR filter, and thus leads to more accurate estimates. The approximation improves with the increase in the number of delays. However, there is a trade-off between the accuracy of the ARM filters (i.e. large d) and the delays caused by the algorithm, which may affect the performance of the application in which the estimated ARM will be used. The time delay itself is unimportant for applications where estimates of radiated sound power are required. However, for real-time control applications, the delay is more significant.

For real-time simulation purposes, the structural responses were simulated in the time-domain by using an array of resonant filters, one filter for predicting the response at one location, each being a 3rd order IIR filter. Simulink was used to simulate the system in real-time under broadband, random noise excitation, and the results showed that the estimated radiated sound power using real-time ARM estimates agreed well with the theoretical values (calculated using Equation 2.12) for both 1-D (i.e. beam) and 2-D (i.e. plate) radiators.

To answer the second research objective, which is to develop feedforward controllers to attenuate the sound radiated from a structure using real-time ARM amplitude as an error function, two control strategies, i.e. non-adaptive and adaptive feedforward control, were

implemented in real-time simulations and presented in Chapter 4. The first example concerned non-adaptive feedforward control applied to a baffled simply supported beam, where the controller transfer function was defined in terms of the primary and secondary paths (refer Equation (4.9)). The controller filter was constructed using the causal-delayed FIR filter approach presented in Section 3.2. Overall, the implemented frequency responses of the controller were able to approximate the theoretical values reasonably well. The second strategy involved adaptive feedforward control applied to a clamped, rectangular plate. The adaptive controllers were designed using the FxLMS algorithm, where the real-time amplitudes of one or more radiation modes were treated as the error signals. The secondary path response was identified by using the auto-correlation method between input and output signals of the secondary path. Both the estimator and controller filters were designed using high order FIR filters. In both strategies, the results showed that controlling more radiation modes in real-time increases the attenuation level and the control bandwidth.

In the last part of Chapter 4, offline optimisation of the location of the control actuators using an ant colony optimisation (ACO) algorithm was presented to answer the third research objective, which is to determine the optimal location of the actuators used to control the sound radiation. The method was applied to the adaptive ASAC system developed earlier. Frequency-averaged attenuation (calculated using Equation (4.29)) was chosen as the objective function of this optimisation. The best location to place a control actuator on a plate to reduce the first ARM amplitude is close to the centre of the plate (i.e. $(x_{c,1}/L_x, y_{c,1}/L_y) = (0.47, 0.47)$), while optimal locations for the second and third control actuators were closer to the corners of the plate (i.e. $(x_{c,2}/L_x, y_{c,2}/L_y) = (0.15, 0.72)$ and $(x_{c,3}/L_x, y_{c,3}/L_y) = (0.85, 0.17)$). The simulation results showed improvements in both attenuation and control bandwidth when the locations of the control actuators were optimised. Different optimisation results may be obtained if a different objective function is used.

Chapter 5 described practical experiments on the estimation and control of radiated sound power for a plate using the ARM estimates approach developed in Chapters 3 and 4, respectively. This chapter was presented to address the last research objective, which was to validate the simulation results experimentally. The experiments were conducted in the reverberation chambers of the acoustics laboratories at the University of Auckland. Real-time data acquisition and signal processing were performed using an NI compact-RIO real-time controller. Results showed that the estimated radiated sound power under broadband, random

excitation was comparable to the sound power estimated according to ISO 3741. Control results obtained for tonal excitation were good at low frequencies, i.e. at third octave bands 1, 2 and 3. However, increasing the number of control actuators did not increase the control performance. The results were poor when the control experiment was repeated using broadband, random noise excitation. The poor performance of the FxLMS controllers for broadband signals and for tonal signals of 200 Hz and above might be caused by issues related to signal processing (i.e. insufficient FIR filter length for estimator filters, group delay, and signal aliasing and reconstruction issues) and hardware (i.e. sensor miscalibration, integrator phase errors, sound leakage through the wall and modification of system responses due to the attachment of sensors).

6.2 Recommendations for future work

The first three objectives of this thesis have been achieved. As for the last objective, the real-time estimation of the radiated sound power using ARM amplitude estimates was successful, as this power is comparable to the powers using ISO 3741 and statistical methods (refer Figure 5.10). However, while reasonable control of tonal signals was achieved for lower frequency excitation, the results of the control were poor for broadband, random signals and for tonal signals of 200 Hz and above. Further experimental studies were not feasible due to time constraints and access to facilities, but should be pursued in future work.

Considering all these factors, the following are suggested for future work.

1. ARM estimation

The ARM filters can be constructed in the time-domain to approximate the response of $Q_{r,n}(\omega)\sqrt{\lambda_r(\omega)}$, which might give a better estimation of the radiated sound power.

The output of this filter can also be used as the cost function of the FxLMS controller, which is expected to improve the control results since it is weighted directly with respect to the eigenvalue (or radiation efficiency). However, there are rapid changes in the eigenvalues with respect to frequency, especially for higher order ARMs (refer Figures 2.3 and 2.5), hence a very long FIR filter might be needed to estimate the

response accurately. IIR filters might be more suitable in this case but there will be instability issue that needs to be considered.

2. Optimisation of sensor and actuator locations

In Chapter 3, the structural sensors were placed equally-spaced on the structures. Optimal sensor locations can be determined using an optimisation algorithm such as a genetic algorithm, ant colony optimisation, etc. Here the objective function is to optimise sensing of the selected ARMs while minimise the sensitivity to other ARMs. These could reduce the number of sensors used or provide more accurate estimates, and hence reduce the signal processing requirements of the controller, and hence reduce the processing time.

The optimisation of actuator locations presented in Section 4.5 used an objective function that minimises the frequency-averaged attenuation of the total radiated sound power W . The optimisation results might be improved by choosing an objective function which comprises the radiated sound power contributed by the individual ARMs (i.e. W_1 , W_2 , etc.) and the frequency range used to calculate the average attenuation might also be the frequency range where only these individual ARM powers are important.

3. Identification of the secondary path in the noise control experiment

The poor performance of the control results in the experiments might be due in part to insufficient length of FIR filters used to estimate the secondary path responses. Based on Figure 5.11, the filter coefficients were not converging to zero even when using the 39th order FIR filters, which is the maximum filter can be written in Compact RIO controller. In other word, longer FIR filters are needed to accurately estimate the secondary path responses. However, care must be taken in choosing the filter length, because longer filters increase the computational cost, which is constrained by the hardware. Alternatively, IIR filters can be used to estimate the secondary path response and they have a much smaller group delay, but a constraint need to be added to make sure the optimised IIR filters are stable.

4. Excitation signal for noise control experiment

Based on the control results, better attenuation was achieved at frequencies below 200 Hz for tonal excitation and poor performance was seen for broadband, random excitation. One of the main reasons is the sheer computational intensity due to many, long FIR filters being used to estimate the ARMs (i.e. 9 ARM filters to output an individual ARM amplitude). Better results might be expected if the plate is excited by either low frequency multi-tone excitation (i.e. 100 Hz + 125 Hz + 160 Hz) or band-limited noise (i.e. up to 160 Hz).

5. Estimation of radiated sound power

Accelerometers were used to measure the plate responses at discrete points. However, this creates a mass-loading effect due to the uneven distribution of mass of the accelerometers, which in turn results in a less accurate estimation of the radiated sound power. The measurement might be improved if the plate response was measured using for example a laser Doppler vibrometer (LDV), which is contactless, hence reducing measurement errors. Note that this sensing approach is not applicable for controlling the radiated sound power since there is a significant processing delay associated with LDV.

6.3 Summary

In summary, the main contributions of this thesis are as follows.

- Propose a method to estimate the ARM in real-time using causal-delayed FIR filters.
- Use the ARM filters to estimate the radiated sound power of one and two dimensional radiating structures.
- Use ARM estimates as the errors functions in active structural acoustic control on both non-adaptive and adaptive feedforward control system.
- Determine the optimal control actuator locations for adaptive control case (applied on the plate radiator) using offline optimisation technique.

The ARM estimation approach proposed in this thesis allows for real-time implementation and give broadband control of strongly radiating vibration. It approximates volume velocity control at low frequencies, while conventional ARM control could be designed based on the ARM shapes at one specific frequency. The advantage of the approach presented here is that the ARM filters allow for the frequency dependence of the ARM shapes, and hence give a better approximation across the frequency range of interest than either of those two methods. While the result is encouraging for simple beam and plate structure, further work is needed to investigate the effectiveness of this approach for more complex structure, such as ribbed plates, shells etc. The output of this thesis could be applied to reduce structure borne noise radiated into vehicle cabins (e.g. car, aeroplane). Although the thesis focuses specifically on beam and plate radiators, the proposed methods could also be applied to any structure or shape, provided that their ARMs are known.

BIBLIOGRAPHY

- [1] P. Gardonio, "Review of Active Techniques for Aerospace Vibro-Acoustic Control," *Journal of Aircraft*, vol. 39, pp. 206-214, 2002.
- [2] F. Fahy and J. Walker, *Advanced applications in acoustics, noise and vibration*: CRC Press, 2004.
- [3] Y.-M. Huang and C.-C. Chen, "Optimal design of dynamic absorbers on vibration and noise control of the fuselage," *Computers & Structures*, vol. 76, pp. 691-702, 2000.
- [4] F. J. Fahy and P. Gardonio, *Sound and structural vibration: radiation, transmission and response*: Academic press, 2007.
- [5] Y. Yun and C. M. Mak, "The theoretical fundamentals of an adaptive active control using periodic Helmholtz resonators for duct-borne transmission noise in ventilation systems," *Building Services Engineering Research and Technology*, vol. 34, pp. 195-201, 2011.
- [6] D. Wu, *et al.*, "Noise Attenuation Performance of a Helmholtz Resonator Array Consist of Several Periodic Parts," *Sensors*, vol. 17, p. 1029, 2017.
- [7] S. J. Estéve and M. E. Johnson, "Reduction of sound transmission into a circular cylindrical shell using distributed vibration absorbers and Helmholtz resonators," *The Journal of the Acoustical Society of America*, vol. 112, pp. 2840-2848, 2002.
- [8] Q. Mao and S. Pietrzko, "Experimental study for control of sound transmission through double glazed window using optimally tuned Helmholtz resonators," *Applied Acoustics*, vol. 71, pp. 32-38, 2010.
- [9] R. C. K. Leung, *et al.*, "Passive noise control by enhancing aeroacoustic interference due to structural discontinuities in close proximity," *Journal of Sound and Vibration*, vol. 330, pp. 3316-3333, 2011.
- [10] S. J. Elliott and M. E. Johnson, "Radiation modes and the active control of sound power," *The Journal of the Acoustical Society of America*, vol. 94, pp. 2194-2204, 1993.
- [11] K. A. Cunefare, "The minimum multimodal radiation efficiency of baffled finite beams," *The Journal of the Acoustical Society of America*, vol. 90, pp. 2521-2529, 1991.

- [12] E. G. Williams and J. D. Maynard, "Numerical evaluation of the Rayleigh integral for planar radiators using the FFT," *The Journal of the Acoustical Society of America*, vol. 72, pp. 2020-2030, 1982.
- [13] C. Wallace, "Radiation resistance of a rectangular panel," *The Journal of the Acoustical Society of America*, vol. 51, pp. 946-952, 1972.
- [14] J. W. S. B. Rayleigh, *The theory of sound* vol. 2: Macmillan, 1896.
- [15] E. G. Williams, "A series expansion of the acoustic power radiated from planar sources," *The Journal of the Acoustical Society of America*, vol. 73, pp. 1520-1524, 1983.
- [16] ISO, "ISO 3741:1975 Acoustics -Determination of sound power levels of noise sources - Precision methods for broad-band sources in reverberation rooms," ed. Geneva, Switzerland: International Organization for Standardization, 1975.
- [17] G. V. Borgiotti, "The power radiated by a vibrating body in an acoustic fluid and its determination from boundary measurements," *The Journal of the Acoustical Society of America*, vol. 88, pp. 1884-1893, 1990.
- [18] K. Naghshineh and G. H. Koopmann, "Active control of sound power using acoustic basis functions as surface velocity filters," *The Journal of the Acoustical Society of America*, vol. 93, pp. 2740-2752, 1993.
- [19] J. Tao and X. Qiu, "Sensor number requirements for sound power prediction using two different mode decomposition methods," *Applied Acoustics*, vol. 70, pp. 646-651, 2009.
- [20] H. Wu, *et al.*, "A method to compute the radiated sound power based on mapped acoustic radiation modes," *The Journal of the Acoustical Society of America*, vol. 135, pp. 679-692, 2014.
- [21] L. Ji and J. S. Bolton, "Sound power radiation from a vibrating structure in terms of structure-dependent radiation modes," *Journal of Sound and Vibration*, vol. 335, pp. 245-260, 2015.
- [22] L. Ji and J. Stuart Bolton, "Coupling mechanism analysis of structural modes and sound radiations of a tire tread band based on the S-mode technique," *Applied Acoustics*, vol. 99, pp. 161-170, 2015.
- [23] Z. Yamaguchi, *et al.*, "Reduction of sound radiation by using force radiation modes," *Applied Acoustics*, vol. 72, pp. 420-427, 2011.

- [24] C. Hesse, *et al.*, "Frequency-independent radiation modes of interior sound radiation: Experimental study and global active control," *Journal of Sound and Vibration*, vol. 401, pp. 204-213, 2017.
- [25] L. Paul, "Process of silencing sound oscillations," ed: Google Patents, 1936.
- [26] J. Qiu and H. Ji, "The application of piezoelectric materials in smart structures in China," *International Journal of Aeronautical and Space Science*, vol. 11, pp. 266-284, 2010.
- [27] S. Elliott and P. Nelson, "The active control of sound," *Electronics & communication engineering journal*, vol. 2, pp. 127-136, 1990.
- [28] S. M. Kuo and D. R. Morgan, "Active noise control: a tutorial review," *Proceedings of the IEEE*, vol. 87, pp. 943-973, 1999.
- [29] J. P. Carneal and C. R. Fuller, "An analytical and experimental investigation of active structural acoustic control of noise transmission through double panel systems," *Journal of Sound and Vibration*, vol. 272, pp. 749-771, 2004.
- [30] R. L. Clark and C. Fuller, "Control of sound radiation with adaptive structures," *Journal of Intelligent Material Systems and Structures*, vol. 2, pp. 431-452, 1991.
- [31] C. C. Fuller, *et al.*, *Active control of vibration*: Academic Press, 1996.
- [32] J. Pan and C. Bao, "Analytical study of different approaches for active control of sound transmission through double walls," *The Journal of the Acoustical Society of America*, vol. 103, pp. 1916-1922, 1998.
- [33] G. Pinte, *et al.*, "Active structural acoustic control of repetitive impact noise," *Journal of Sound and Vibration*, vol. 319, pp. 768-794, 2009.
- [34] A. Grewal, *et al.*, "Active cabin noise and vibration control for turboprop aircraft using multiple piezoelectric actuators," *Journal of Intelligent Material Systems and Structures*, vol. 11, pp. 438-447, 2000.
- [35] D. Palumbo, *et al.*, "Flight test of active structural acoustic noise control system," *Journal of aircraft*, vol. 38, pp. 277-284, 2001.
- [36] T. Kaizuka and N. Tanaka, "Vibroacoustic modes and active control of both vibration and sound," *AIAA journal*, vol. 46, pp. 1490-1504, 2008.
- [37] E. Bianchi, *et al.*, "Smart panel with multiple decentralized units for the control of sound transmission. Part III: control system implementation," *Journal of Sound and Vibration*, vol. 274, pp. 215-232, 2004.

- [38] P. Gardonio, *et al.*, "Smart panel with multiple decentralized units for the control of sound transmission. Part I: theoretical predictions," *Journal of Sound and Vibration*, vol. 274, pp. 163-192, 2004.
- [39] P. Gardonio, *et al.*, "Smart panel with multiple decentralized units for the control of sound transmission. Part II: Design of the decentralized control units," *Journal of Sound and Vibration*, vol. 274, pp. 193-213, 2004.
- [40] G. P. Gibbs, *et al.*, "Radiation modal expansion: Application to active structural acoustic control," *The Journal of the Acoustical Society of America*, vol. 107, pp. 332-339, 2000.
- [41] M. N. Currey and K. A. Cunefare, "The radiation modes of baffled finite plates," *The Journal of the Acoustical Society of America*, vol. 98, pp. 1570-1580, 1995.
- [42] S.-B. Choi, "Active structural acoustic control of a smart plate featuring piezoelectric actuators," *Journal of Sound and Vibration*, vol. 294, pp. 421-429, 2006.
- [43] M. Johnson and S. Elliott, "Active control of sound radiation using volume velocity cancellation," *The Journal of the Acoustical Society of America*, vol. 98, pp. 2174-2186, 1995.
- [44] T. Sors and S. Elliott, "Volume velocity estimation with accelerometer arrays for active structural acoustic control," *Journal of Sound and Vibration*, vol. 258, pp. 867-883, 2002.
- [45] P. Gardonio, *et al.*, "Analysis and measurement of a matched volume velocity sensor and uniform force actuator for active structural acoustic control," *The Journal of the Acoustical Society of America*, vol. 110, pp. 3025-3031, 2001.
- [46] J. M. Fisher, *et al.*, "Development of a pseudo-uniform structural quantity for use in active structural acoustic control of simply supported plates: An analytical comparison," *The Journal of the Acoustical Society of America*, vol. 131, pp. 3833-3840, 2012.
- [47] J. M. Fisher, *et al.*, *Development of a pseudo-uniform structural quantity for use in active structural acoustic control of simply supported plates: An analytical comparison* vol. 131, 2012.
- [48] K. C. Sahu, *et al.*, "Active piezoelectric-structure acoustic control of a soft-core sandwich panel using volume velocity and a weighted sum of spatial gradient control metric," *Journal of Vibration and Control*, vol. 23, pp. 2391-2400, 2017.

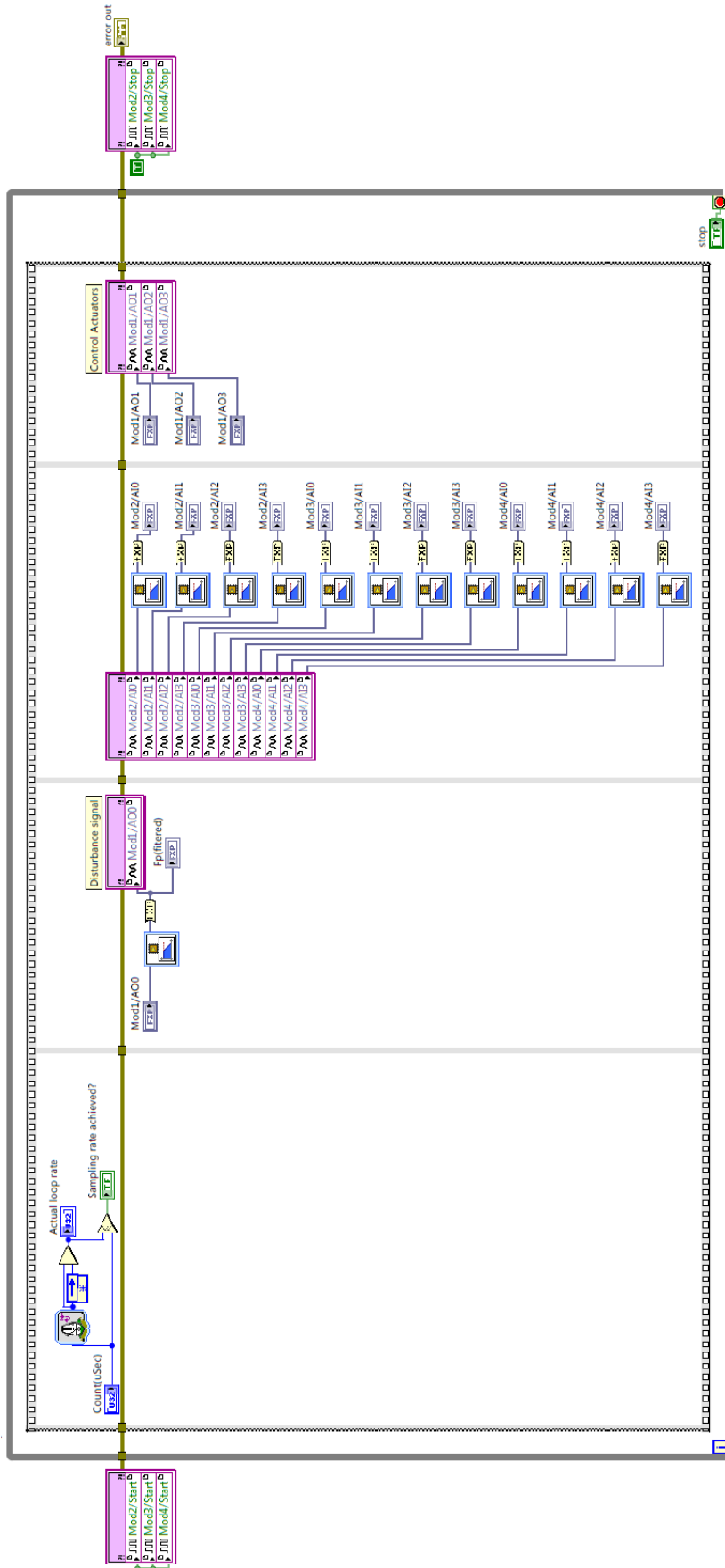
- [49] P. Aslani, *et al.*, "Active control of cylindrical shells using the weighted sum of spatial gradients control metric," *The Journal of the Acoustical Society of America*, vol. 137, pp. 2258-2258, 2015.
- [50] D. R. Hendricks, *et al.*, "Experimental active structural acoustic control of simply supported plates using a weighted sum of spatial gradients," *The Journal of the Acoustical Society of America*, vol. 136, pp. 2598-2608, 2014.
- [51] A. P. Berkhoff, "Broadband radiation modes: Estimation and active control," *The Journal of the Acoustical Society of America*, vol. 111, pp. 1295-1305, 2002.
- [52] G. V. Borgiotti and K. E. Jones, "Frequency independence property of radiation spatial filters," *The Journal of the Acoustical Society of America*, vol. 96, pp. 3516-3524, 1994.
- [53] J. Maillard, "Advanced time domain sensing for active structural acoustic control," Virginia Polytechnic Institute and State University, 1997.
- [54] W. Wu, "Analysis of acoustic radiation mode in time domain," *Science in China Series E: Technological Sciences*, vol. 52, pp. 2384-2390, 2009.
- [55] J. P. Maillard and C. R. Fuller, "Advanced time domain sensing techniques for active structural acoustic control," *The Journal of the Acoustical Society of America*, vol. 92, pp. 2411-2411, 1992.
- [56] F. Fahy and P. Gardonio, "3 - Sound Radiation by Vibrating Structures," in *Sound and Structural Vibration (Second Edition)*, ed Oxford: Academic Press, 2007, pp. 135-241.
- [57] Q. Mao and S. Pietrzko, *Control of Noise and Structural Vibration: A MATLAB®-Based Approach*: Springer Science & Business Media, 2013.
- [58] C. R. Fuller, *et al.*, "2 - Introduction to Waves in Structures," in *Active Control of Vibration*, ed London: Academic Press, 1996, pp. 25-57.
- [59] S. S. Rao and F. F. Yap, *Mechanical Vibrations*: Prentice Hall, 2011.
- [60] F. Fahy and P. Gardonio, "2 - Structural Mobility, Impedance, Vibrational Energy and Power," in *Sound and Structural Vibration (Second Edition)*, ed Oxford: Academic Press, 2007, pp. 75-134.
- [61] F. Fahy and P. Gardonio, "1 - Waves in Fluids and Solid Structures," in *Sound and Structural Vibration (Second Edition)*, ed Oxford: Academic Press, 2007, pp. 1-73.
- [62] C.-C. Sung and C. T. Jan, "Active control of structurally radiated sound from plates," *The Journal of the Acoustical Society of America*, vol. 102, pp. 370-381, 1997.

- [63] J. P. Arenas, "On the vibration analysis of rectangular clamped plates using the virtual work principle," *Journal of Sound and Vibration*, vol. 266, pp. 912-918, 2003.
- [64] J. W. Weaver, *et al.*, *Vibration Problems in Engineering*: John Wiley & Sons, 1990.
- [65] S. S. Rao, *Vibration of continuous systems*: John Wiley & Sons, 2007.
- [66] C. A. Brebbia and J. Dominguez, *Boundary elements: an introductory course*: Computational Mechanics, 1992.
- [67] K. A. M. Nor, *et al.*, "Time-domain estimation of acoustic radiation modes and active structural acoustic control," in *Acoustics 2016: The Second Australasian Acoustical Societies' Conference*, 2016.
- [68] B. R. Mace and C. R. Halkyard, "Time domain estimation of response and intensity in beams using wave decomposition and reconstruction," *Journal of Sound and Vibration*, vol. 230, pp. 561-589, 2000.
- [69] S. J. Elliott, "Optimal and Adaptive Digital Filters," in *Signal Processing for Active Control*, ed London: Academic Press, 2001, pp. 49-102.
- [70] C. R. Fuller, *et al.*, "4 - Feedforward Control," in *Active Control of Vibration*, ed London: Academic Press, 1996, pp. 91-113.
- [71] S. J. Elliott, "2 - Optimal and Adaptive Digital Filters," in *Signal Processing for Active Control*, ed London: Academic Press, 2001, pp. 49-102.
- [72] B. Widrow and M. E. Hoff, "Adaptive Switching Circuits," in *1960 IRE WESCON Convention Record, Part 4*, 1960, pp. 96-104.
- [73] M. Dorigo and T. Stützle, *Ant Colony Optimization*: Mit Press, 2004.
- [74] M. Garcia, *et al.*, "Path planning for autonomous mobile robot navigation with ant colony optimization and fuzzy cost function evaluation," *Applied Soft Computing*, vol. 9, pp. 1102-1110, 2009.
- [75] K. A. M. Nor, *et al.*, "Optimization in Active Vibration Control: Virtual Experimentation Using COMSOL Multiphysics - MATLAB Integration," in *2014 5th International Conference on Intelligent Systems, Modelling and Simulation*, 2014, pp. 385-389.
- [76] M. Dorigo and T. Stützle, "An experimental study of the simple ant colony optimization algorithm," in *2001 WSES International Conference on Evolutionary Computation (EC'01)*, 2001, pp. 253-258.
- [77] A. G. A. Muthalif and R. S. Langley, "Active control of high-frequency vibration: Optimisation using the hybrid modelling method," *Journal of Sound and Vibration*, vol. 331, pp. 2969-2983, 2012.

- [78] ISO, " ISO 3741:1975 Acoustics - Determination of sound power levels of noise sources - Precision methods for broadband sources in reverberation rooms," ed. Geneva, Switzerland: International Organization for Standardization, 1975.
- [79] L. Cremer, *et al.*, "Radiation from Bending Waves," in *Structure-Borne Sound: Structural Vibrations and Sound Radiation at Audio Frequencies* Third ed Berlin: Springer 2005, pp. 483-507.

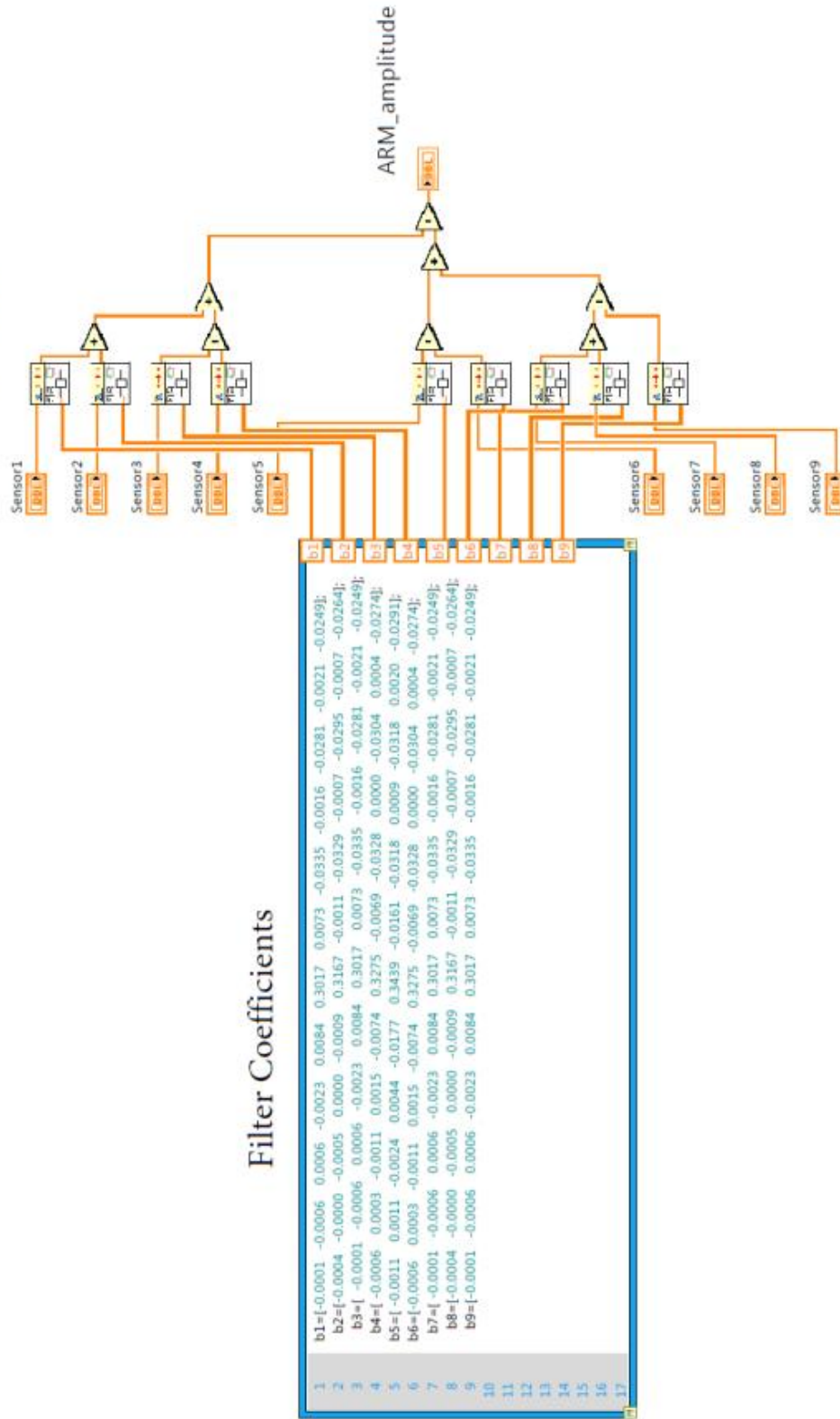
APPENDIX A

LABVIEW CODES

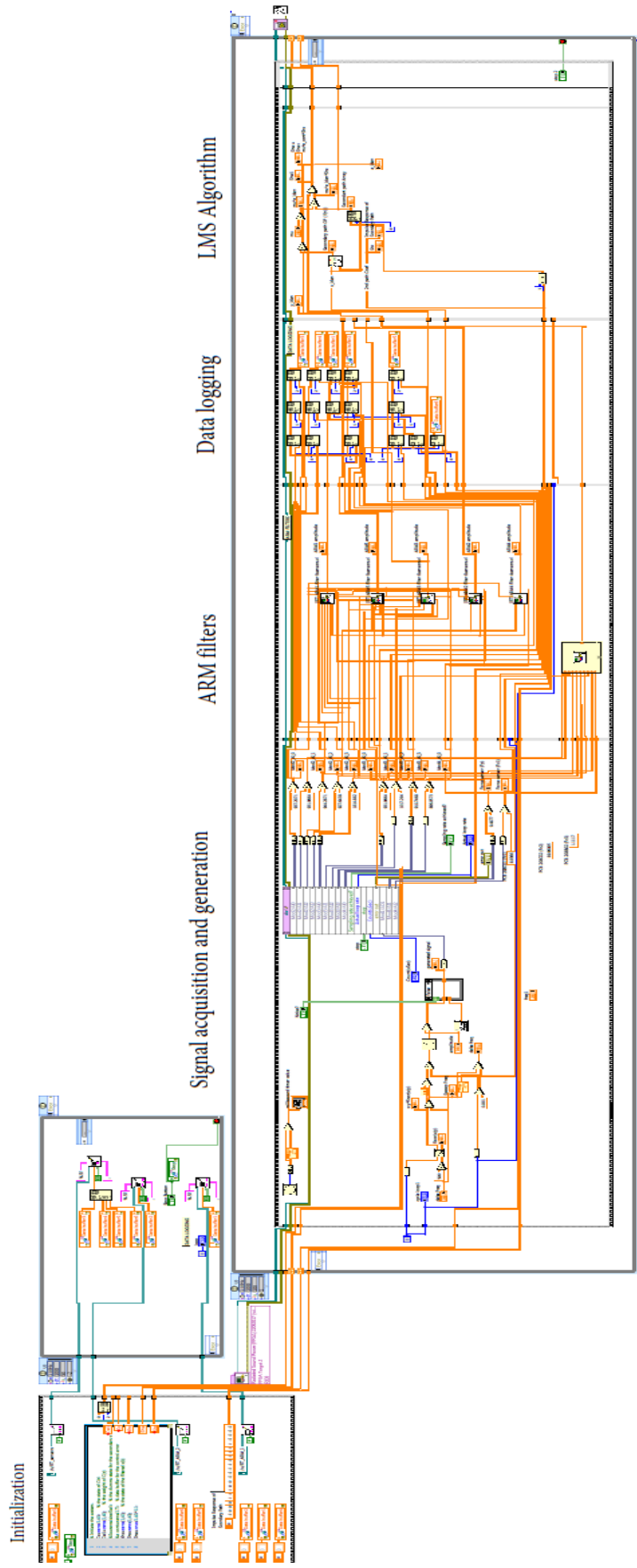


Appendix A.1: Labview FPGA code for signal acquisition and transmission.

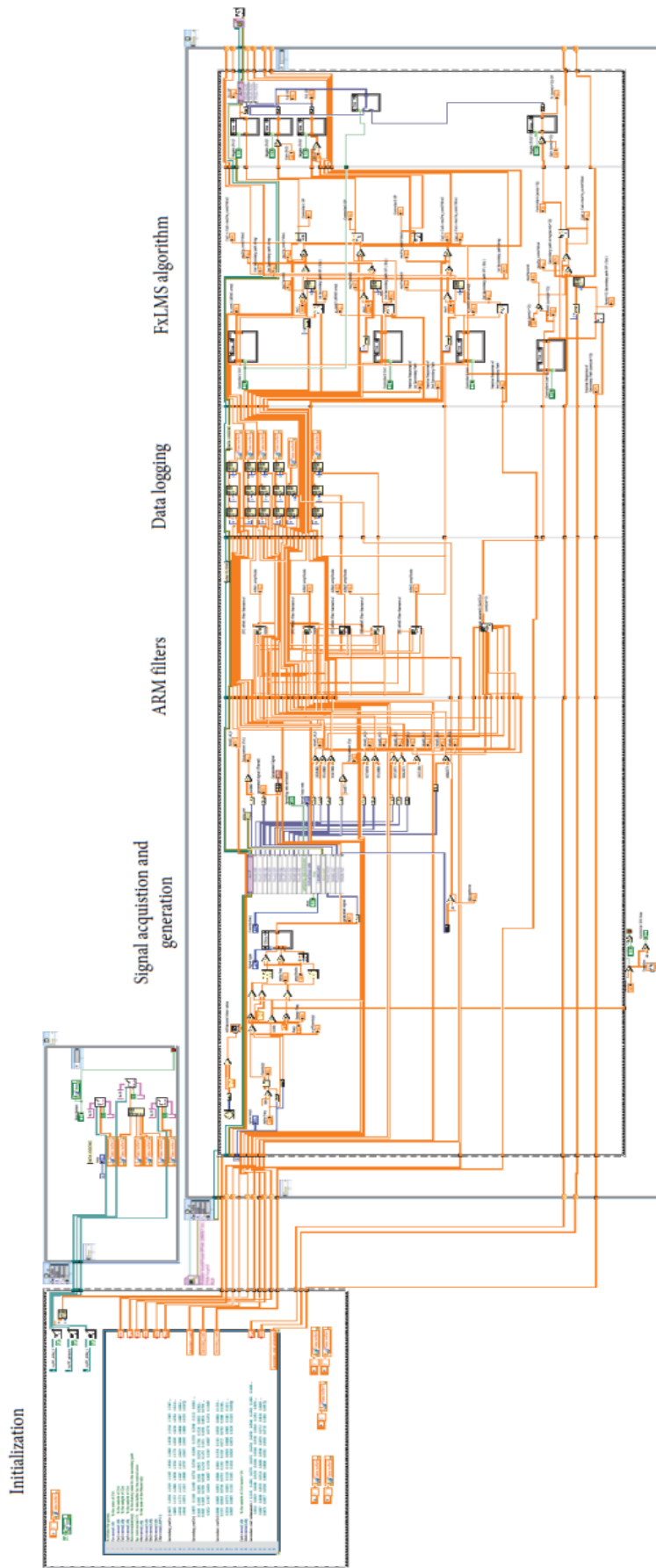
ARM filters



Appendix A.2: Labview RT code for ARM filters.



Appendix A.3: Labview RT scan code for system identification, used to estimate the secondary path filter coefficients.



Appendix A.4: Labview RT code for estimation and control of radiated sound power.